10-14-1966

OPTICAL AND ELECTRON-PARAMAGNETIC RESONANCE STUDIES OF SODIUM-FLUORIDE

Ronald Allen Andrews
Wayne State University

OPTICAL AND ELECTRON PARAMAGNETIC RESONANCE STUDIES OF SODIUM FLUORIDE

by

RONALD A. ANDREWS

A DISSERTATION

Submitted to the Office for Graduate Studies,
Graduate Division of Wayne State University, Detroit, Michigan,
in partial fulfillment of the requirements
for the degree of

DOCTOR OF PHILOSOPHY

1966

MAJOR: PHYSICS (SOLID STATE)

APPROVED BY:

Oct 14, 1966
Advisor Date

David W. Moore

John P. Olive

ACKNOWLEDGEMENTS

The author of this thesis wishes to sincerely thank Professor Y.W. Kim for his guidance during the past four years.

Thanks are also due to Messrs. J. VanGemen and M. Shopnick for much patience and help in preparing experimental equipment; Miss B. Collins, Miss J. Filinger, and Mrs. B. Gregory for typing the many drafts of this manuscript; and Mr. H. Brown for preparing photographs and slides.

The author is also indebted to the Harshaw Chemical Company for doing a spectroscopic analysis of several crystals of NaF, and the Wayne State University Computing and Data Processing Center for machine time on an IBM 7074 computer.

Sincere appreciation is also expressed to the National Science Foundation for fellowship support during the past four years, and the United States Atomic Energy Commission, whose contract (AT(11-1)-1054) supported the research described herein.

TABLE OF CONTENTS

Page

Acknowledgements ii

List of Tables v

List of Figures vi

Chapter

I. Introduction 1

II. Basic Concepts 4

Color Centers 4

Electron Paramagnetic Resonance (EPR) 11

III. Experimental Set-Up and Techniques 17

Optical Spectrophotometer 17

EPR Spectrometer 22

Helium Cryostat 29

IV. Electron Paramagnetic Resonance of Fe^{3+} in NaF 38

Introduction 38

Experimentals 39

Experimental Results and Spin Hamiltonian 40

Temperature Effects 47

Discussion 53

Conclusion 57

V. Iron Impurity Controlled F to M Conversion in X-Irradiated NaF 59

Introduction 59

Experimental Procedure and Results 61

Empirical Analysis of the Aging Effects 69

Proposed Mechanism of Optical Bleaching 71

TABLE OF CONTENTS (Cont'd.)

Chapter		Page
	Discussions of the Experimental Results.	76
	Conclusion	78
VI.	Observation of an Unstable N Band in NaF.	79
Appendix I.	Hyperfine Interaction Term in a Spin Hamiltonian. . .	85
Appendix II.	Spin Hamiltonian for $S_{5/2}$ - State Ions in a Cubic Crystalline Field	92
List of References		102
Autobiographical Statement		105

LIST OF TABLES

Table		Page
1.	Spin Hamiltonian parameters for the observed resonance due to Fe^{3+} in NaF at 77°K.	48
2.	Values of Empirical Parameters of Eq. (28)	70

LIST OF FIGURES

Figure		Page
1.	Schematic diagram of an F center: Stereoscopic view plus a section in the (100) plane.	5
2.	(a) Configuration coordinate diagram of an F center (b) Breathing mode of vibration of the six nearest neighbor cations of the F center	7
3.	Schematic diagrams of the current models for F-aggregate centers: (a) A stereoscopic view of the M center and a section in the (100) plane, (b) A stereoscopic view of the R center and a section in the (111) plane, (c) Stereoscopic view of the N_1 and N_2 centers	10
4.	Energy level diagram for an electron in a magnetic field. .	13
5.	Diagram illustrating the geometry of a sample in a spectrophotometer light beam	18
6.	Schematic diagram of an optical absorption spectrophotometer	20
7.	Modification of the spectrophotometer sample compartment for optical bleaching experiments.	23
8.	Schematic diagram of an EPR spectrometer.	24
9.	Output of an EPR spectrometer illustrating why the recorded signal is the first derivative of the absorption line. .	28
10.	Scaled schematic drawing of the complete helium cryostat. .	30
11.	Section of cryostat tail taken at right angles to the section given in Fig. 10	33
12.	Details of the microwave cavity and the coupling mechanism.	36
13.	The observed EPR spectra (solid lines) and the theoretical fit (dots) of Fe^{3+} in NaF at 77°K for $\theta = 0°$, $55°$, and $90°$.	41-42
14.	The observed EPR spectra (solid lines) and the theoretical fit (dots) of Fe^{3+} in NaF near 180°K for $\theta = 90°$ and $\theta = 55°$.	49

Figure Page

15. The observed temperature dependence of the EPR spectral amplitude for $\theta = 90^{o}$ and $\theta = 55^{o}$ (solid curves). The dashed curves represent the experimental curves corrected for the Boltzmann temperature dependence. 50

16. The temperature dependence of a, γ, and W found by fitting the experimental data at several temperatures. g and δ are found to be constant within experimental error. . . 52

17. Schematic diagram showing, (a) associated charge compensating cation vacancies in next-nearest neighbor positions forming a "complex", and (b) a charge compensating vacancies away from the Fe^{3+} ion. In this case the Fe^{3+} ions are left in a site with cubic symmetry and the vacancies are free to migrate at sufficiently high temperatures depending on the activation energy . . 55

18. Typical x-ray colorability curves for F centers in Type I and Type II samples at room temperature 63

19. Typical optical bleaching curves for the F and M centers in Type I (F_I and M_I) and Type II (F_{II} and M_{II}) samples 65

20. A typical M center optical bleaching curve of a Type I sample illustrating aging effects after pauses in the F-light optical bleaching at points A and B. The optical density of the M-band is plotted as a function of the net bleaching time. As for the dashed curves, see text. 67

21. Schematic diagram illustrating the models of an anion vacancy (α), a cation vacancy ($\tilde{\alpha}$), a vacancy pair ($\alpha,\tilde{\alpha}$), and the Seitz model of an M center (M_s). e^- indicates a trapped electron. 73

22. A probable mode of decay of the M_s center into an M center and an $\tilde{\alpha}$ center. e^- represents a trapped electron. The arrows in the left hand diagram indicate the probable motion of lattice ions 74

23. λ_{max} (dots) of N-bands, and also F- and M-bands, observed in several alkali halides, and Ivey's relations (straight lines) for the bands. The straight lines for the F- and M-bands are taken from ref. 2: $\lambda_{max} = 703\ d^{1.84}$ (F-band) and $\lambda_{max} = 1400\ d^{1.56}$ (M-band). They are included here for comparison. 80

24. Behavior of the band N, and the F- and M-bands during optical bleaching with F-light. Note the different ordinate scales for the F- and M-bands and the band N . 82

Figure Page

25. Exponential decay with time constant 7.8 hours of the band N_1 when left in the dark. 83

26. Coordinate system used to find the hyperfine interaction between a paramagnetic ion and a single nuclear magnetic moment. $\vec{H}$ is directed along the z' axis and the nuclear magnetic moment is located on the z axis. 88

27. Coordinate system of the cubic lattice (x,y,z) and a primed coordinate system in which $\vec{H}$ is along the z' axis. . . . 94

28. Angular variation of the fine structure components of a resonance line for rotation about the [110] axis ($\phi = 45^{o}$). 100

CHAPTER I

INTRODUCTION

Pure alkali halide crystals are transparent and consist of singly ionized alkali ions (positive) and singly charged halide ions (negative) in a face-centered cubic (space) lattice, except for the cesium halides, which are simple cubic. When subjected to ionizing radiation or made to take on a stochiometric excess of alkali ions, these crystals acquire characteristic coloration[1] (NaF becomes light orange, NaCl becomes yellow, KCl becomes violet, etc.). This coloration is due to point defects in the crystalline lattice, which are called color centers. These color centers absorb light from the visible part of the optical spectrum and, in some cases, from the near ultra-violet, depending on the host lattice and the electronic structure of the color centers.

When crystals colored by ionizing radiation are exposed to light of the proper frequency, the acquired coloration tends to change, and at the same time the degree of coloration slowly decreases. This is due to the "optical bleaching" of some of the color centers. The bleaching is dual in its operation: selective destruction of one type of color center and formation of other types of color centers. These new color centers exhibit new optical absorption bands which appear in the visible and near infrared parts of the optical spectrum. The bleaching process is found to be affected by the presence of impurities in the lattice.

A few mechanisms have recently been proposed for the optical bleaching process by several independent workers.[2] However, it is not clear which one of the proposed mechanisms gives the correct

description of the bleaching process. Furthermore, no specific mechanism or mechanisms appear to have been proposed for the role of impurities in the optical bleaching process.

An experimental study of these optical processes and the role of impurities in these processes is the purpose of the present thesis. The experiments described in this thesis make use of iron as an impurity in NaF which is colored by x-rays near room temperature. These experiments determine (1) the interaction of x-ray photons with the iron impurity and (2) the role of the impurity in the optical bleaching process. The results to be obtained from such studies provide significant information concerning the interactions among various color centers, impurities, and the lattice.

These topics are investigated by the methods of electron paramagnetic resonance (EPR) and optical absorption spectroscopy at controlled temperatures between 4.2°K and 300°K.

Chapter II of this thesis gives a brief survey of the known color centers in the alkali halides, including currently accepted models for the color centers, optical characteristics of alkali halide crystals containing color centers, and the role of EPR in the color center research. Also included is a brief discussion of the principles of EPR. The experimental methods are described in Chapter III. Included in this section is a description of an EPR spectrometer, an optical absorption spectrometer, and a liquid helium cryostat for combined EPR and optical studies.

Chapter IV presents the results of EPR studies of the x-ray conversion of Fe^{2+} in NaF to Fe^{3+} and Fe^{+}, and the interaction of Fe^{3+} (an S-state ion) with the host lattice. These EPR results

prepare the way for studies of the optical processes in x-irradiated NaF samples with and without the iron impurity. The results of these optical studies are presented in Chapter V. Finally, the observation of a previously unobserved unstable optical absorption band in NaF is discussed in Chapter VI.

Two appendices are given for reference purposes in the present thesis; one of them is concerned with the spin Hamiltonian for an S-state ion such as Fe^{3+} in a cubic crystalline field, and the other is concerned with the nuclear hyperfine interaction.

CHAPTER II

BASIC CONCEPTS

Color Centers

Color centers in the alkali halides have been a research topic for over fifty years. Recently many excellent review articles with extensive bibliographies have appeared.[1-5] Therefore, in the brief summary of relevant color center topics which follows, only very recent work will be cited in the list of references. Details of the other topics can be found in the review articles.

The color center which has received the most attention is the F center. The F center is simply an electron trapped at an anion vacancy in the lattice (see Fig. 1). It has the simplest structure of all the color centers in the alkali halides and is responsible for the most prominent (optical absorption) band in "colored"* crystals. This band, which is very broad,+ is called the F-band since it is due to optical transitions of the F center electron. A simple theory of the F center treats the electron as being in a coulomb potential well, and the problem is similar to the hydrogen atom problem. The ground state is a 1s orbital state and the first excited state is a triply degenerate 2p state which lies just below the conduction band of the solid. The interaction of the electron with the lattice is best visualized by use of a configuration coordinate diagram as shown in Fig. 2(a). This figure illustrates a plot of energy vs.

---

* The term "colored" crystal is used throughout this thesis to indicate any crystal which contains any type of color center.

+ In NaF the F-band is centered at λ = 340 mμ and it has a width of about .51 ev. See Ref. 2 for a complete listing of color centers in all the alkali halides.

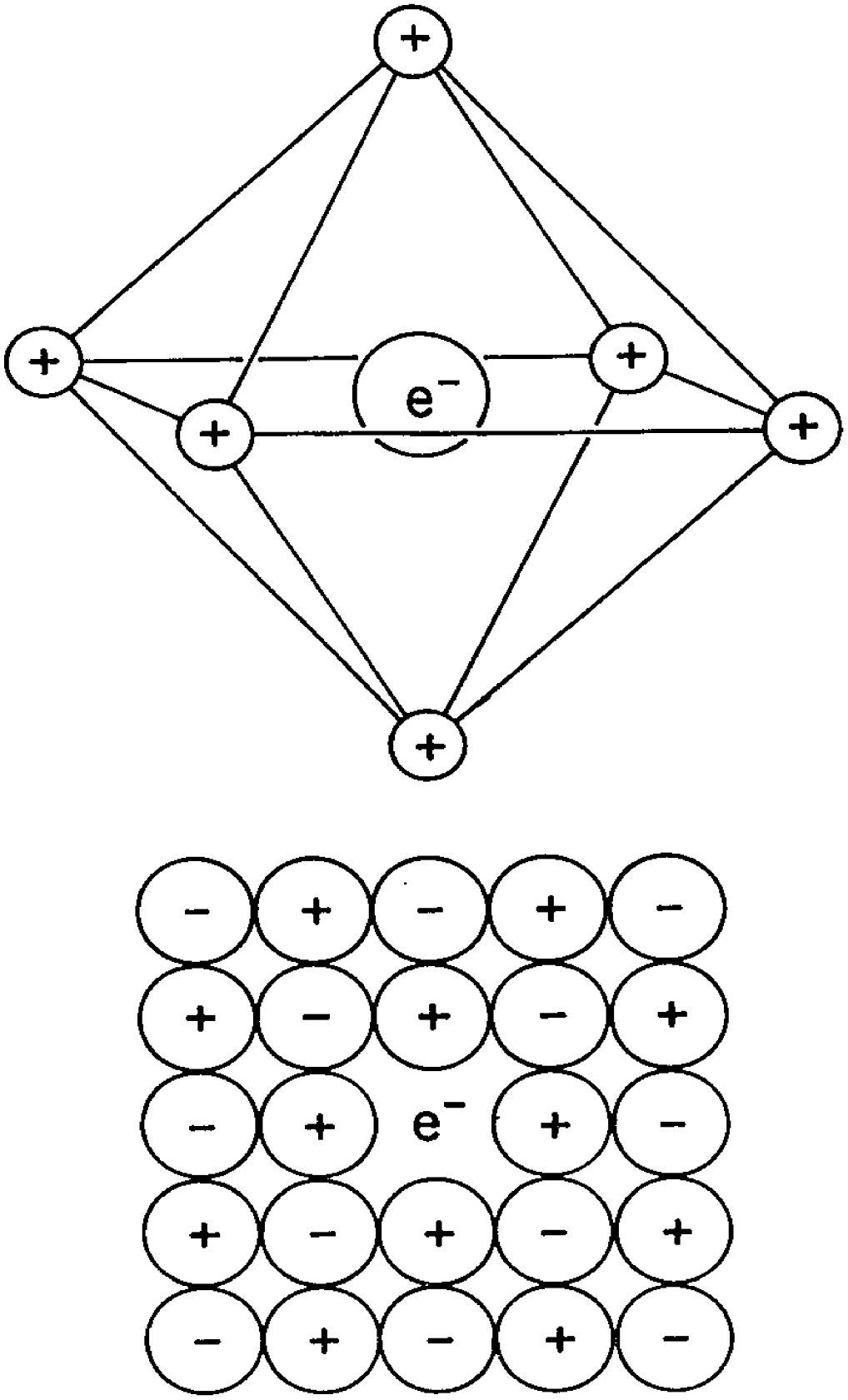

Fig. 1. Schematic diagram of an F center: Stereoscopic view plus a section in the (100) plane.

a configuration coordinate for the ground and first excited states of the F center. The coordinate q describes the "breathing" mode, which is the principal vibrational mode of the ions in the neighborhood of the point defect. This vibrational mode is illustrated in Fig. 2(b), where the six nearest neighbors of the F center move in unison as shown.

A configuration diagram such as the one shown in Fig. 2(a) can be used to explain the following experimentally observed properties of F centers: (1) why the F-band is not a sharp line as is observed for the absorption spectrum of free atoms; (2) why the observed luminescence of the F center has a large Stokes shift*; (3) why it is possible to have radiationless transitions; and (4) why optical bleaching is accompanied by photoconductivity. To see why the above effects are reasonable, consider the absorption process in terms of the diagram in Fig. 2. During an optical transition, the nuclear coordinates, and hence q, remain fixed according to the Frank-Condon principle.[6] The ground state and the first excited state, however, have many vibrational levels which are illustrated by a set of parallel horizontal lines above the points A and G, respectively, in Fig. 2. Hence, the values of the nuclear coordinates at any given time depend on the vibrational state of the neighboring ions. Typically, the center of the absorption band might correspond to a transition from point A to point B on the configuration coordinate diagram. In this case the absorbed photon has an energy $h\nu_{AB} = E_B - E_A$. At room temperature,

---

* A Stokes shift is a shift in frequency of the luminescent light (ν_ℓ) from the exciting light (ν_e). In returning to the ground state the electron emits a photon and it also can give energy to the lattice; hence, $\nu_e < \nu_\ell$.

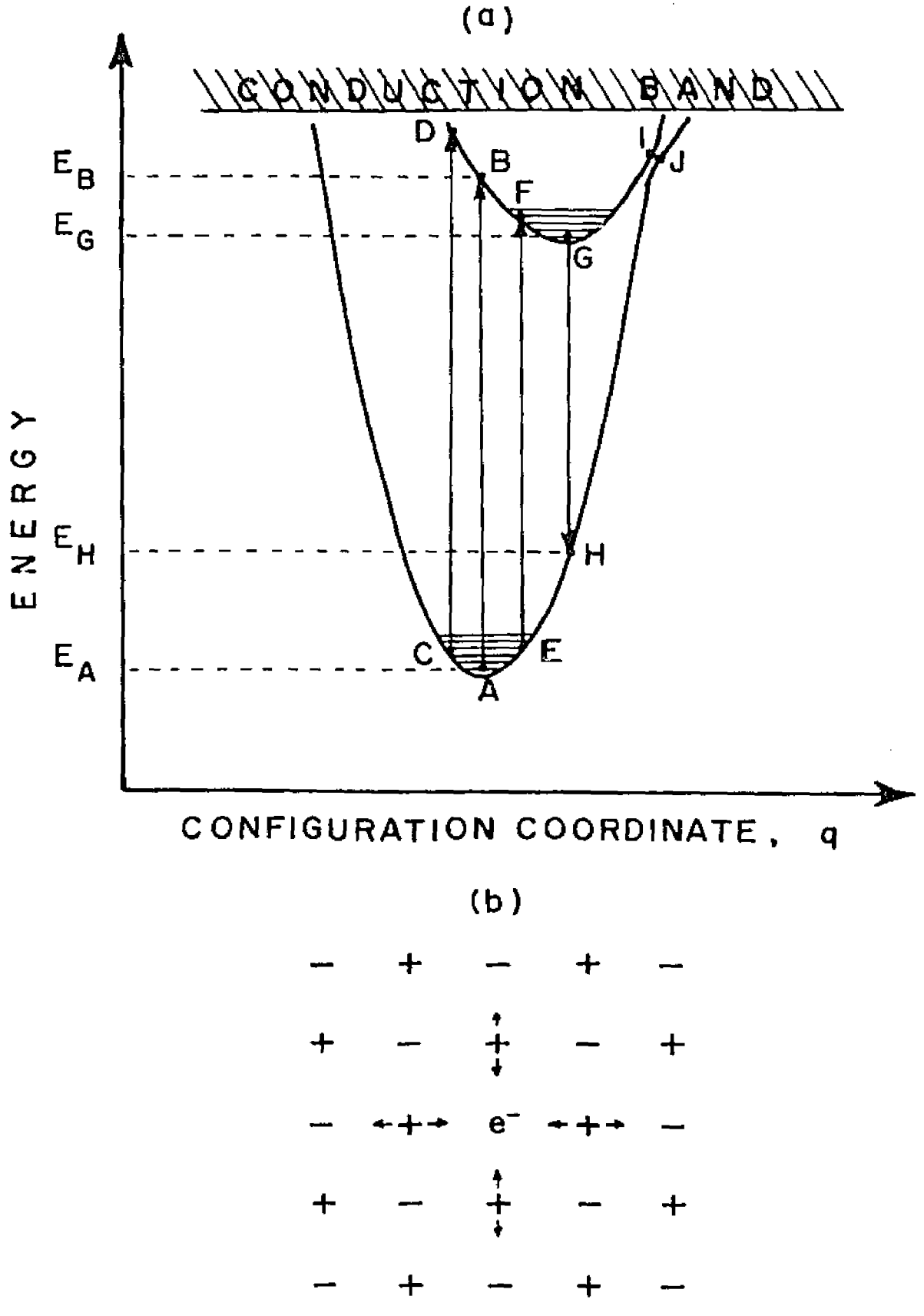

Fig. 2. (a) Configuration coordinate diagram of an F center. (b) Breathing mode of vibration of the six nearest neighbor cations of the F center.

many of the higher energy vibrational states will be excited and transitions from C to D and from E to F will also occur, giving rise to the width of the absorption band.

When the electron is in the excited state, it has a wave function different from the ground state wave function. The energy of the excited electron will be a different function of q and, in general, q will have a new equilibrium value. In returning to the ground state, the electron may give up a part of its energy to the lattice and "drop" to point G in the configuration coordinate diagram. From point G it can spontaneously drop back to the ground state at point H emitting a photon $h\nu_{GH} < h\nu_{AB}$. The energy of the emitted photon is observed as luminescence with a large Stokes shift corresponding to the reduction of frequency. If the thermal energy is sufficiently large, the electron at point G can go to point I and to point J and then relax to point A giving up all its energy to the lattice in a radiationless transition. There is also the possibility that the excited F center electron will absorb sufficient thermal energy and be excited into the conduction band, contributing to the photo-conductivity. Once in the conduction band, it is free to migrate until it becomes trapped at another defect or impurity center.

If light in the region of the F-band (simply F-light) is incident on a colored crystal containing primarily F centers, then the (absorption) intensity of the F-band decreases and new bands at longer wavelengths are known to develop. These new bands are associated with new color centers called F-aggregate centers, which are nearest-neighbor combinations of F centers. The simplest of the F-aggregate centers is the M center, which is a pair of F centers at nearest

neighbor sites as shown in Fig. 3(a). The M-band is the first of the optical absorption bands on the long wavelength side of the F-band to appear during optical bleaching. After the M-band starts to grow, two bands called R_1 and R_2 grow with constant intensity ratio. These bands are due to two different transitions of the R center which is illustrated in Fig. 3(b). As shown, the R center is a nearest neighbor combination of three F centers. Finally, the N_1- and N_2-bands appear. These bands are attributed to two different N centers, called N_1 and N_2 centers. Both N centers are a combination of four F centers (see Fig. 3(c)); N_1 has a planar configuration and N_2 is a tetrahedron. Recent work on F-aggregate centers is summarized in Ref. 2. Of the F-aggregate centers, the M center has received the most attention and its model is very well established.[7,8] The N centers have received comparatively little attention and there is still doubt concerning the proposed models.[9]

Other color centers play an important role in the F→F-aggregate conversion. These are electrically charged color centers, such as the F' and F_2^+ centers. A prime (') indicates that the otherwise neutral color center has an excess electron. Hence an F' center is an F center with two electrons instead of one. A superscript plus (+) indicates the lack of an electron. Hence, and M^+ center is an M center with only one electron. The accepted model of the M center is often called the F_2 model of the M center, F_2 meaning a nearest neighbor combination of two F centers. Similarly, the currently accepted model of the R center is the F_3 model.

It has been known for a long time that impurities affect color center processes,[10] in particular, the colorability of crystals.

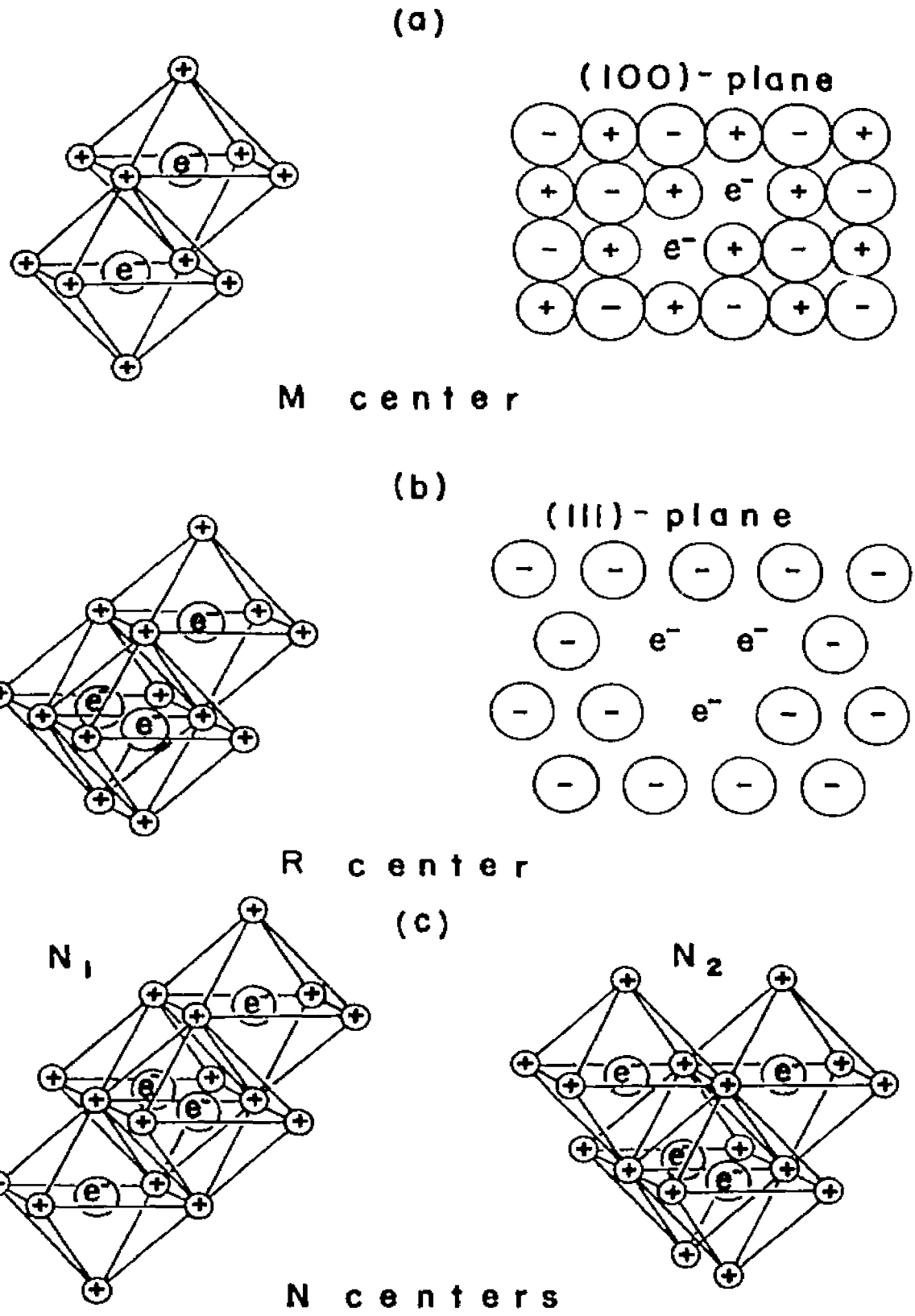

Fig. 3. Schematic diagrams of the current models for F-aggregate centers: (a) A sterescopic view of the M center and a section in the (100) plane, (b) A sterescopic view of the R center and a section in the (111) plane, (c) Stereoscopic view of the N_1 and N_2 centers.

Impurity ions may be effectively electron or hole traps, and thus have an influence on the coloration process. Some impurities are foreign atoms entering the host lattice in interstitial positions and thus causing local strains and defects in the lattice. Others are divalent or trivalent foreign atoms, entering the lattice substitutionally. In either case, divalent or trivalent impurity ions force the formation of charge compensating vacancies in the lattice to maintain local electrical neutrality. These vacancies may be bound to an impurity ion to form a well defined complex, or they may be unbound and free to migrate at sufficiently high temperatures.

Electron Paramagnetic Resonance (EPR)

The fundamental concepts of EPR and its applications are discussed by many authors.[11-15] It is the purpose of this summary to indicate briefly what EPR is and what information can be obtained about paramagnetic ions by using EPR techniques.

To illustrate the concept of EPR consider the case of a single free electron in a static magnetic field $\vec{H}$. The electron has a magnetic moment

$$\vec{\mu} = -g\beta\vec{S} \tag{1}$$

where

g = electronic g factor,

β = Bohr magneton,

$\vec{S}$ = the electron's spin angular momentum .

When placed in a magnetic field, the magnetic moment of the electron interacts with the field such that the interaction energy is given by

$$E = -\vec{\mu} \cdot \vec{H} = g\beta \vec{S} \cdot \vec{H} \quad . \tag{2}$$

This is what is commonly called the Zeeman interaction and it causes the electron to have two energy levels characterized by the spin quantum number $m_s = \pm 1/2$ as shown in Fig. 4. When $H = H_o$, the difference in energy between the two Zeeman levels is given by

$$\Delta E = g\beta H_o \quad . \tag{3}$$

Classically the electronic magnetic moment $\vec{\mu}$ can be considered to precess about the magnetic field $\vec{H}$.[11] The application of an oscillating magnetic field of frequency ν, perpendicular to $\vec{H}$, can cause magnetic dipole transitions between these two spin levels if the resonance condition, $h\nu = \Delta E$, where h is Planck's constant, is satisfied. For g values around two, magnetic fields of 10^3 to 10^4 gauss correspond to frequencies of about 10^{10} cps.

Consider now that this electron is placed in a solid substance. For convenience consider the case of an F center in an otherwise perfect lattice. The F center electron is no longer free and it interacts with its environment. The charged ions surrounding the F center produce a crystalline field which will play a major role in determining the F center wave function. All the neighboring nuclei in the lattice have magnetic moments. These nuclear magnetic moments will interact with the magnetic moment of the F center electron (hyperfine interaction). Details of the hyperfine interaction are discussed in Appendix I. The resonance condition is altered by the hyperfine interaction. When a single nucleus of spin I is involved, the resonance condition is given by (See Eq. A-21):

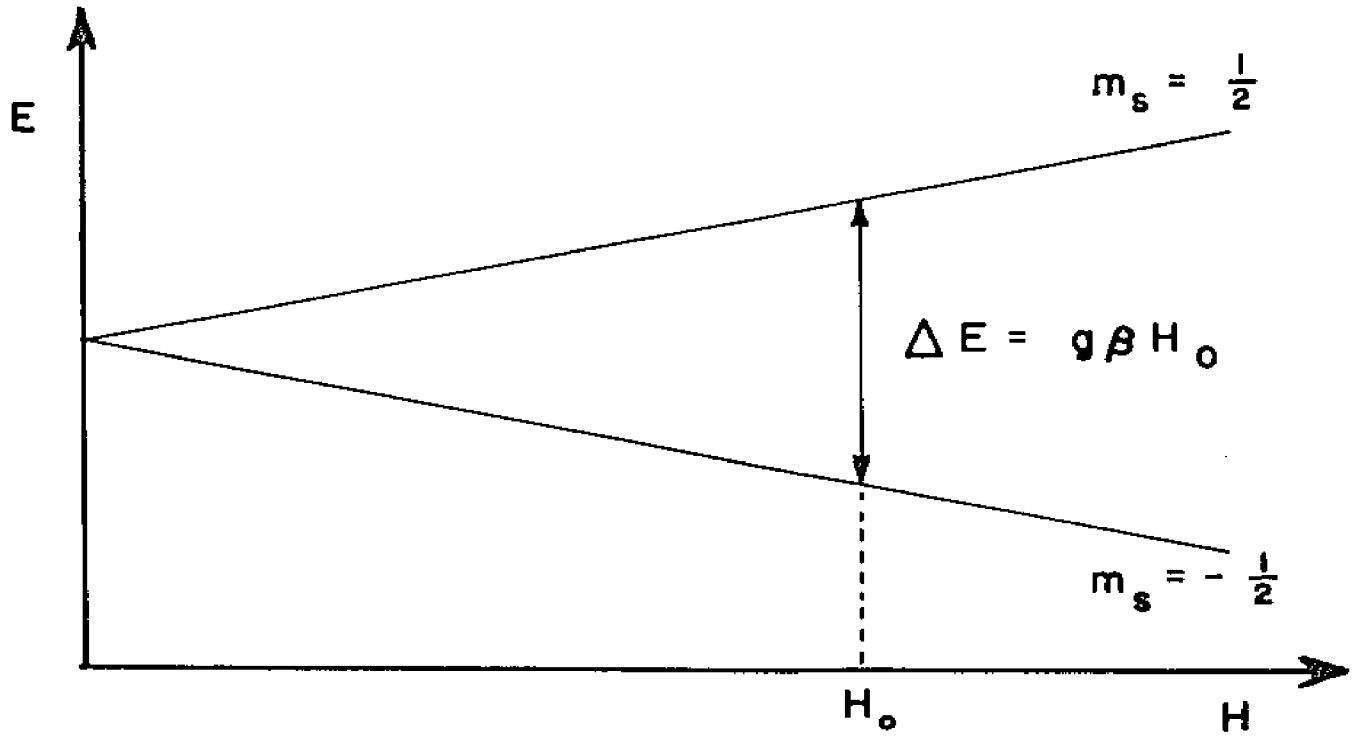

Fig. 4. Energy level diagram for an electron in a magnetic field.

$$h\nu = g\beta H + M_I W_{HFS} \tag{4}$$

where

$$W_{HFS} = \delta + \gamma (3\cos^2\theta - 1) \quad , \tag{5}$$

M_I = magnetic quantum number of the interacting nucleus with spin I = I, I - 1, ... - (I - 1), - I;

and θ = the angle between $\vec{H}$ and the direction of the radius vector from the center of the F center to the nuclear site.

The value of g in Eq. 4 is in general different from the free electron g value of 2.0023. Also in more general cases the value of g can depend on the direction of $\vec{H}$ relative to a crystal and in this case the g value is described by a tensor. This topic is treated in detail in Ref. 15. In most EPR experiments ν is kept constant and H is varied. Thus, transitions now occur when

$$H = \frac{1}{g\beta}(h\nu - M_I W_{HFS}) = H_o - M_I \left(\frac{W_{HFS}}{g\beta}\right) \quad , \tag{6}$$

instead of H_o. Hence, where without the hyperfine interaction there would be one resonance line at $H = H_o$, with the hyperfine interaction there are 2I + 1 hyperfine lines symmetrically distributed on both sides of H_o. Details of the EPR spectra due to F centers in alkali halides have been discussed by many authors.[3,14,15]

Any ion or system of electrons with $\vec{L}$ or $\vec{S} \neq 0$ is paramagnetic.[15] Hence, some color centers other than F centers are paramagnetic. EPR signals have been observed for R centers[16,17] (3 electrons with S = 1/2, 3/2) and the metastable triplet state of M centers

(2 electrons with S = 1). Also, transition element ions have an unfilled inner electron shell and have $\vec{S}$ and/or $\vec{L} \neq 0$, making them paramagnetic. Like the F center electron, when a paramagnetic ion is placed in a solid substance, it interacts with its environment. If there are neighboring nuclear magnetic moments, there is a hyperfine interaction just as in the F center case. In general, besides the hyperfine interaction, there are the following: (1) the spin-orbit interaction, (2) the crystalline field interaction, and (3) a spin-spin interaction between electrons.

The Hamiltonian which describes the paramagnetic ion in a solid substance takes into account all of the interactions of the ion with its environment and is quite complicated. To explain an EPR spectrum, it is not necessary to work with this "complete" Hamiltonian, $\mathcal{H}$. This is because EPR involves only magnetic dipole transitions which are described by a change of the magnetic quantum numbers only. Hence, it is convenient to work with a Hamiltonian which has only spin operators. This Hamiltonian is called a "spin Hamiltonian"[18] and is labeled $\mathcal{H}_S$. $\mathcal{H}_S$ is obtained from $\mathcal{H}$ by calculating

$$\mathcal{H}_S = \int \psi^* \mathcal{H} \psi \, d\tau \tag{7}$$

where ψ is the orbital wave function of the paramagnetic ion and the integral is over the orbital variables only. These integrals then appear as constants (or parameters from the spectroscopists' point of view) in $\mathcal{H}_S$.

An example of a paramagnetic ion is Fe^{3+}. This ion has a $^6S_{5/2}$ ground state. When placed into an alkali halide, Fe^{3+} must

have a spin Hamiltonian which takes into account three effects: (1) the Zeeman interaction of a magnetic moment due to S = 5/2 with the external static magnetic field H, (2) the hyperfine interaction of the magnetic moment with all the neighboring nuclear magnetic moments, and (3) the effects of the crystalline field and spin-orbit coupling, which are effects that are greater than first order for the case of an S state ion. The latter interactions (3) give rise to what is called fine structure and details of this term in the spin Hamiltonian are presented in Appendix II.

By examining an EPR signal due to a paramagnetic ion in detail, one can determine what types of interactions are taking place. Knowing this, it is possible to "fit" the observed spectra with an appropriate spin Hamiltonian with the right values of the spin Hamiltonian parameters. At this point one is able to infer: (1) what the spin of the paramagnetic ion is, (2) whether or not it is an S-state ion, (3) the spin quantum numbers of the nuclei with which it interacts, (4) the hyperfine coupling constants of the interacting nuclei (See Appendix I), and (5) where in the lattice the paramagnetic ion is located. Many other things can be inferred[3,15] but most important is the fact that EPR gives the experimentalist a microscopic view of the environment of a paramagnetic ion.

CHAPTER III

EXPERIMENTAL SET-UP AND TECHNIQUES

As mentioned previously, color center research involves the use of both an optical spectrophotometer for measuring the optical absorption bands due to color centers and an EPR spectrometer for investigating paramagnetic impurities and color centers. These two instruments along with a versatile cryostat for combined EPR and optical work will be described separately in the following sections.

Optical Spectrophotometer

Color centers manifest themselves macroscopicly by absorbing light in characteristic bands lying in the visible, near infrared, or near ultraviolet portions of the optical spectrum. The measured optical absorption is characterized in terms of an absorption coefficient of the material, $\alpha(\lambda)$, where λ is the wavelength of the incident light. Consider the situation illustrated in Fig. 5 where a monochromatic beam of light of wavelength λ and intensity I_o is incident normally on a crystal of thickness d. The transmitted beam has an intensity I where $I < I_o$ (assume that there is no diffuse scattering of light). At a point x in the crystal the intensity is $I(x)$. In traversing a distance dx in the crystal, the intensity of the beam is diminished by an amount $dI = -\alpha(\lambda)\, I(x)dx$. By integrating this differential equation with the proper boundary conditions, the following solution is obtained:

$$I(x) = I_o \exp\,[-\alpha(\lambda)x] \quad . \tag{8}$$

Hence, the intensity of the transmitted light is obtained as

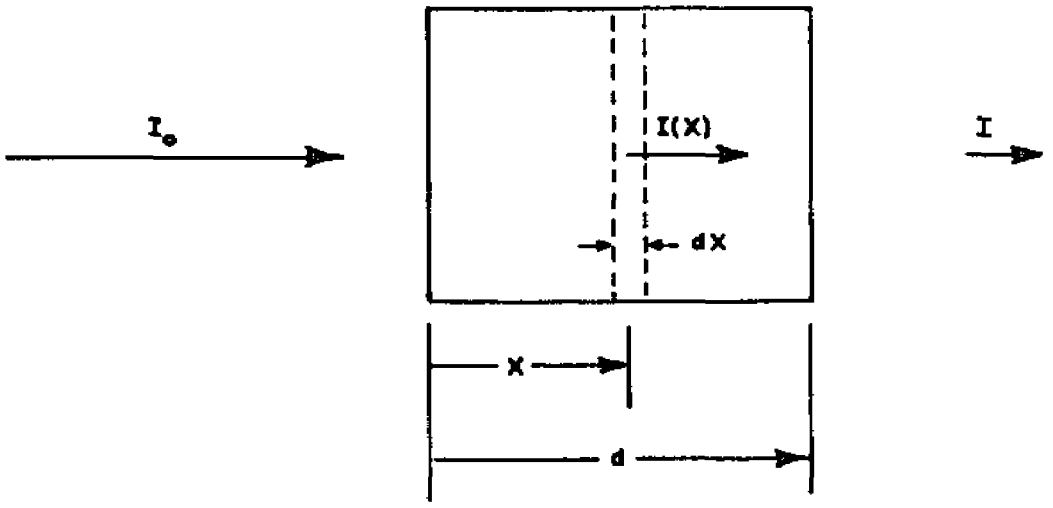

Fig. 5. Diagram illustrating the geometry of a sample in a spectrophotometer light beam.

$$I = I(d) = I_o \exp [- \alpha(\lambda)d] \quad . \tag{9}$$

An optical spectrophotometer measures αd as a function of λ for a given crystal. αd is called the optical density. The spectrophotometer that was used in the present experiments is a Bausch and Lomb 505 recording spectrophotometer. Details of this instrument are given in a Bausch and Lomb manual.[19] Therefore, only a brief explination of how the instrument measures optical density, α(λ)d, will be presented here. A schematic diagram of the spectrophotometer is given in Fig. 6. A condensing lens system (B) collects light from a source of light (A) and focuses it on the entrance slit (C) of a monochrometer. The light source (A) is a tungsten lamp for the visible spectrum (λ = 400 mμ → 700 mμ) and a deuterium discharge lamp for the near ultraviolet spectrum (λ = 200 mμ → 400 mμ). A monochromatic beam of wavelength λ emerges from the exit slit and two mechanically connected chopping wheels chop these beams at (E) in such a way that they are alternately transmitted as shown in Fig. 6. Each beam is chopped at 60 cps such that it is on once each cycle for a period of 1/4 of a cycle. One beam passes through the sample (F) under investigation and is called the sample beam, while the other is used as a reference and is called the reference beam. The reference and sample beams are focused at (G) onto the photomultiplier cathode. The reference beam and the sample beam are alternately incident on the photomultiplier (H). The photomultiplier output is proportional to the incident light intensity and it is amplified by a preamplifier (I) as shown. The sensitivity of the photomultiplier is determined by the high voltage applied to its dynodes. This voltage is changed automatically to maintain the proper sensitivity, as will

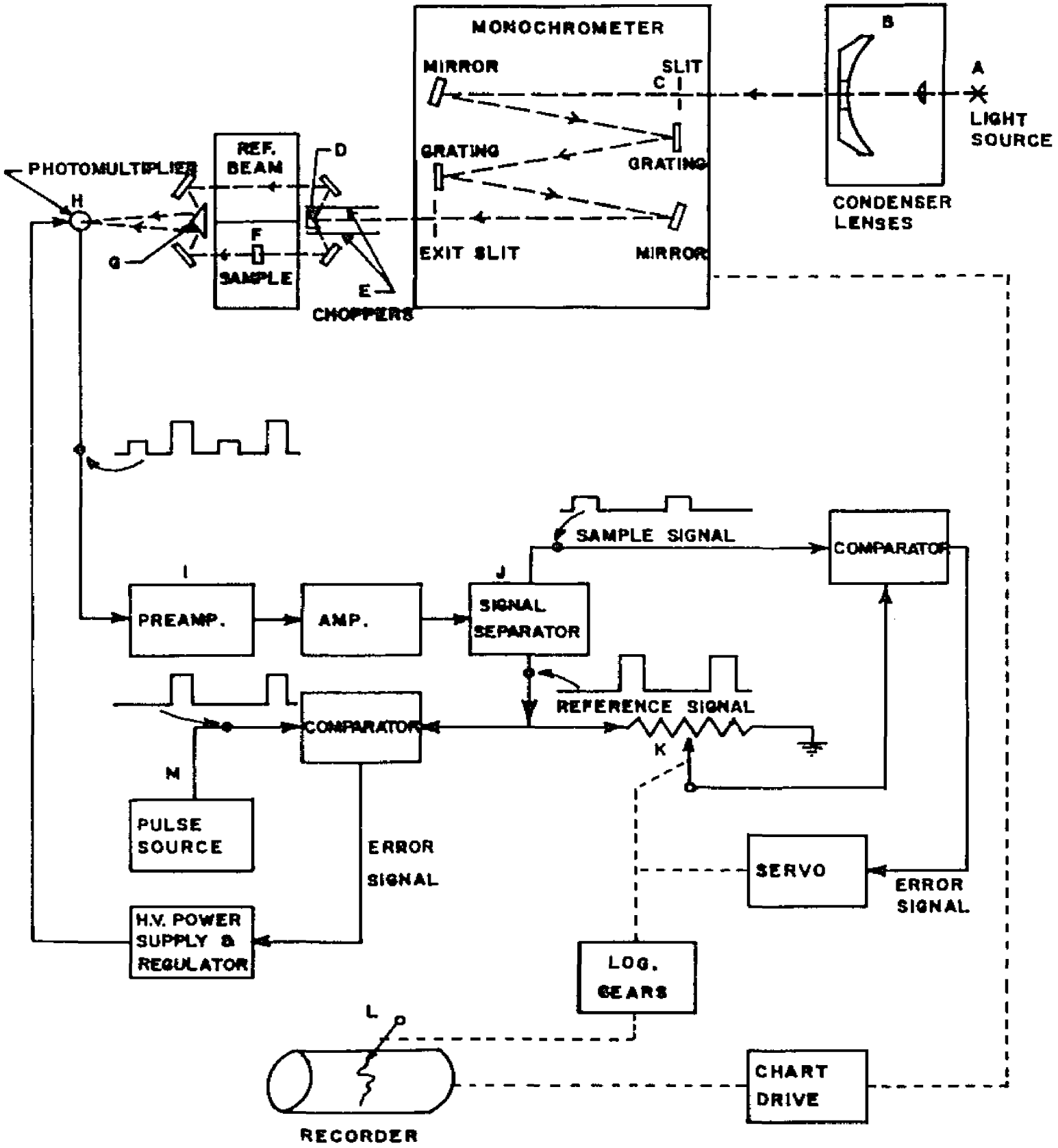

Fig. 6. Schematic diagram of an optical absorption spectrophotometer (a Bausch and Lomb Spectronic 505).

be described below. After being amplified, the reference and sample signals are separated at (J). The reference signal is applied to a potentiometer (K) whose slider is mechanically connected to a recorder pen (L). By means of a servo mechanism, the potentiometer slider is constantly maintained at a position such that the voltage at the slider is equal to the voltage of the sample signal. Hence, the ratio of the distance of the potentiometer slider from the grounded end of the potentiometer to the length of the potentiometer is equal to (I/I_o). However, the mechanical connection between the potentiometer and the recorder pen is via logarithmic gears. Thus, the pen records a signal proportional to $|\ln (I/I_o)| = \alpha(\lambda)d$. Now the absorption coefficient is proportional to the concentration of color centers absorbing light of wavelength λ. Therefore, at a given wavelength, the recorded output is proportional to the concentration of absorbing color centers. A continuous curve ($\alpha(\lambda)d$ vs. λ) is obtained by scanning the monochrometer over a range of values of λ.

The dual-beam feature (sample beam and reference beam) prevents changes in $I_o(\lambda)$ with wavelength from being interpreted as sample absorption. It also reduces noise due to fluctuations in the intensity of the light source. As part of this feature, the reference signal is maintained at a constant level by comparing the reference signal to the output of a constant voltage pulse source (M) and by changing the high voltage applied to the photomultiplier. This is done electronically by using the difference in voltage between the reference signal and the pulse source as an error signal for the high voltage regulator. If the reference signal decreases, the high voltage is increased. This

increase of high voltage on the photomultiplier provides a larger accelerating potential for the electrons freed from the photocathode. Hence, the sensitivity of the photomultiplier is effectively increased and the output current is maintained at a constant level when the reference beam is incident on the photomultiplier.

For an optical bleaching experiment, it is necessary to shine a bleaching light of a selected wavelength on the sample, and at regular intervals measure the changes in the optical absorption bands. For this purpose, the sample compartment shown in Fig. 6 is modified as illustrated in Fig. 7. The sample is mounted in a sample holder which can be rotated by 90°. In the 0° position the sample is in the sample beam of the spectrophotometer and in the 90° position, it is in the bleaching beam. The bleaching beam is produced by means of a 150 watt high pressure mercury arc lamp (N) and a monochrometer (O). This beam is perpendicular to the direction of the sample beam and it is focused on the sample by means of a lens (P). The intensity of the sample beam is much less than the intensity of the bleaching beam. Hence, bleaching caused by the sample beam during an optical density measurement is negligible.

EPR Spectrometer

The spectrometer assembly used in the present work consists mainly of (1) a Varian Model V4500 EPR spectrometer, operated in the X band of microwave frequencies (8.2 to 12.4 kMcps) with magnetic field modulation at 100 kcps and audio frequencies, and (2) an associated Varian model V3603 12 inch rotating laboratory magnet. A block diagram of the assembly is given in Fig. 8. Since the

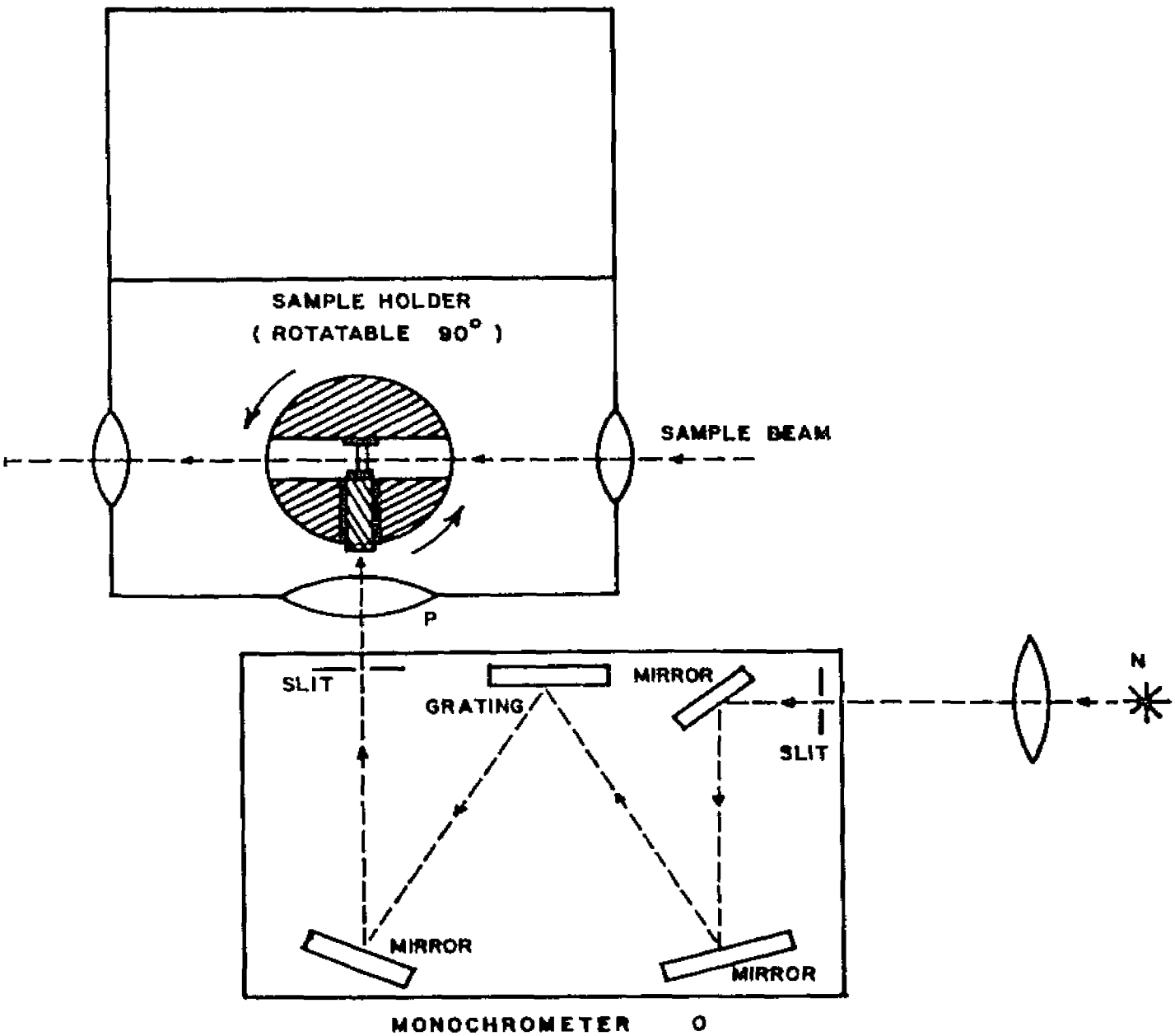

Fig. 7. Modification of the spectrophotometer sample compartment for optical bleaching experiments.

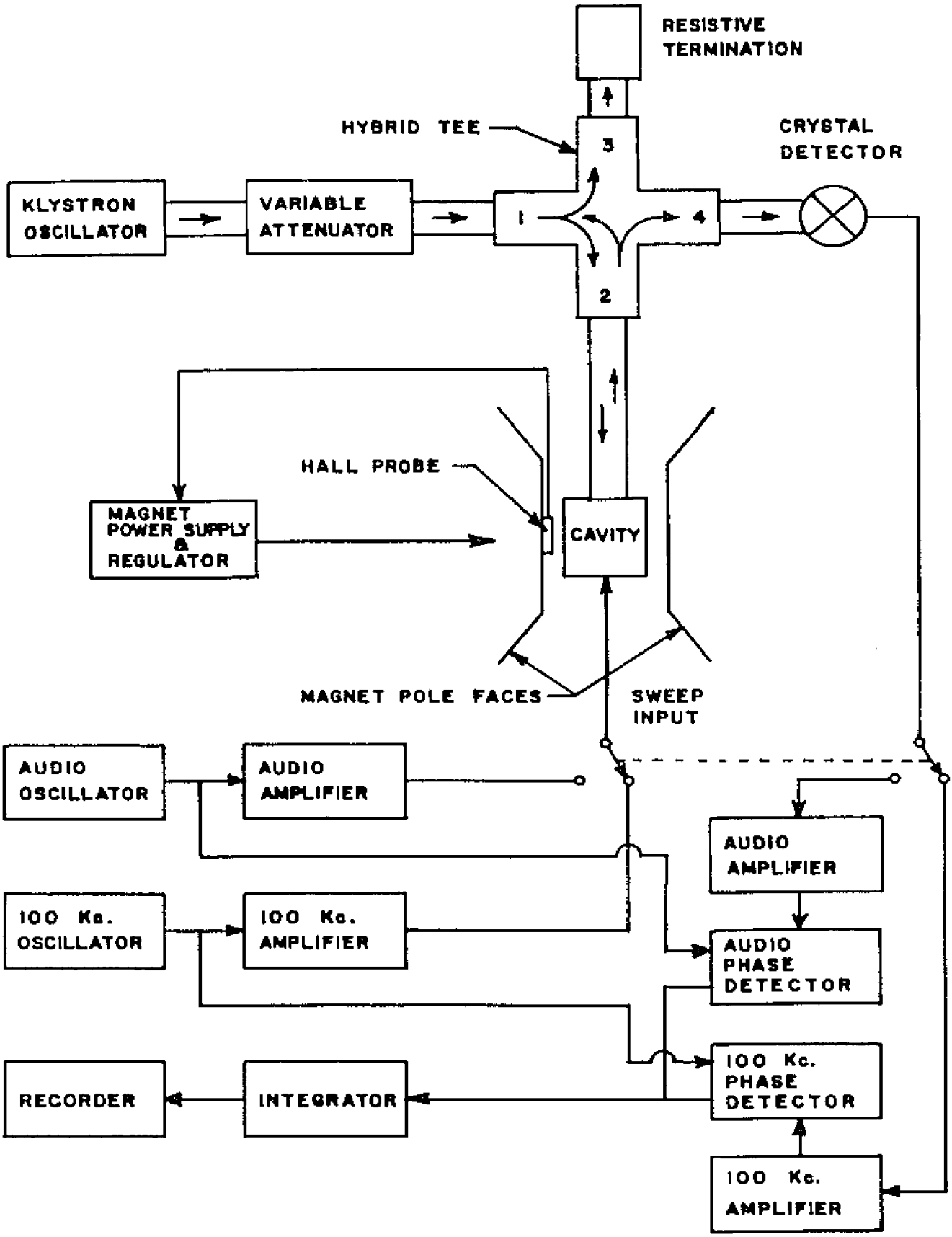

Fig. 8. Schematic diagram of an EPR spectrometer.

operational details of this system are given in a Varian manual,[20] only a brief summary of its operation will be given here.

The sample which contains paramagnetic ions must be placed in an environment where the resonance condition, $h\nu = g\beta H_o$, can be satisfied. As mentioned in Chapter II, two things are necessary to satisfy the resonance condition: (1) a static magnetic field H_o, and (2) an oscillating magnetic field of frequency ν perpendicular to H_o. The static field is supplied by the large 12 inch electromagnet. The sample is located in a microwave cavity which is centered in the air gap of this electromagnet. The purpose of this microwave cavity is to supply the oscillating magnetic field. The sample is positioned in the cavity in the region of maximum oscillating microwave magnetic field. This oscillating field may be thought of in terms of two rotating magnetic fields: one rotating in the same sense as the precessing magnetic moments of the paramagnetic ions in the sample and the other rotating in the opposite sense. The microwave field which rotates in the same sense as the precessing magnetic moments provides the required pertubation to cause magnetic dipole transitions in the sample. The microwave frequency ν of the oscillating field is kept fixed at about 9.3 kMc and the static magnetic field is varied until the resonance condition is satisfied.

The spectrometer must detect the absorption of microwave power by the sample when the resonance condition is satisfied. To see how this is accomplished, we must first digress and explain how the microwave radiation reaches the cavity. Referring to Fig. 8, it can be seen that the microwave power from the klystron is supplied to arm one of the hybrid tee. This power is then divided between a

resistive load in arm three, and arm two. Since the impedance of the microwave cavity with the sample in place is matched to the impedance of arm two when the resonance condition is not satisfied, all the power in arm two is absorbed by the microwave cavity. When the resonance occurs, the sample absorbs power and, by so doing, changes the impedance match between the cavity and arm two of the hybrid tee. This mismatch is proportional to the power absorbed by the sample, and causes a reflected wave to propagate back from the cavity to arm two, where it is divided between arm four and arm one. Arm four is terminated by a crystal detector. This detector provides a voltage proportional to the microwave power incident on it, which in turn is proportional to the mismatch of the cavity. Hence, by monitoring the voltage output of the crystal detector while the static magnetic field is swept, one can detect the signal representing the power absorption, which will be referred to as the EPR signal of the sample in the following. The situation is slightly complicated by the fact that when the sample absorbs power in the microwave cavity, it also shifts the resonant frequency of the microwave cavity. This shift in the resonant frequency from its off resonance value is known as dispersion. The spectrometer system as shown in Fig. 8 discriminates against dispersion and detects a signal proportional only to the absorbed microwave power by locking the klystron frequency to the microwave cavity. Details of this automatic frequency control (AFC) can be found elsewhere.[21]

The signal observed at the crystal detector is a D.C. signal and it is accompanied by noise which might obscure a weak EPR signal. In order to overcome this problem, the spectrometer system uses a

combination of magnetic field modulations and narrow band detection. The magnetic field modulation is produced by a pair of Helmholtz sweep coils on opposite sides of the cavity. These coils are driven by a combination of a 100 kc oscillator (or an audio frequency) and a power sweep amplifier. The AC magnetic field produced by these coils is parallel to the static magnetic field. This field modulation causes the sample to see a varying magnetic field, which in turn modulates the signal seen by the crystal detector when the resonance condition is satisfied (see Fig. 9). Without field modulation a DC signal appears at the crystal detector. This DC signal is proportional to the "bell shaped" resonance line obtained when H is scanned through the resonance point as shown in Fig. 9. The AC signal due to the field modulation is amplified by a narrow band amplifier tuned to the field modulation frequency. This "narrow band detection" eliminates all the noise except the small fraction present at the field modulation frequency.

The size of the amplified AC signal is proportional to the slope of the absorption line at that particular value of magnetic field. Further, the phase of the amplified signal shifts by 180° when the slope of the absorption curve changes sign. Therefore, the amplified signal is sent through a phase sensitive detector, which uses the field modulation oscillator as a reference, and the result is a demodulated signal proportional to the first derivative of the absorption line as shown in Fig. 9. To further reduce the noise content of this derivative signal it is passed through an integration network and finally it is displayed by a graphic recorder as shown in Fig. 8. The shape of the recorded absorption line in

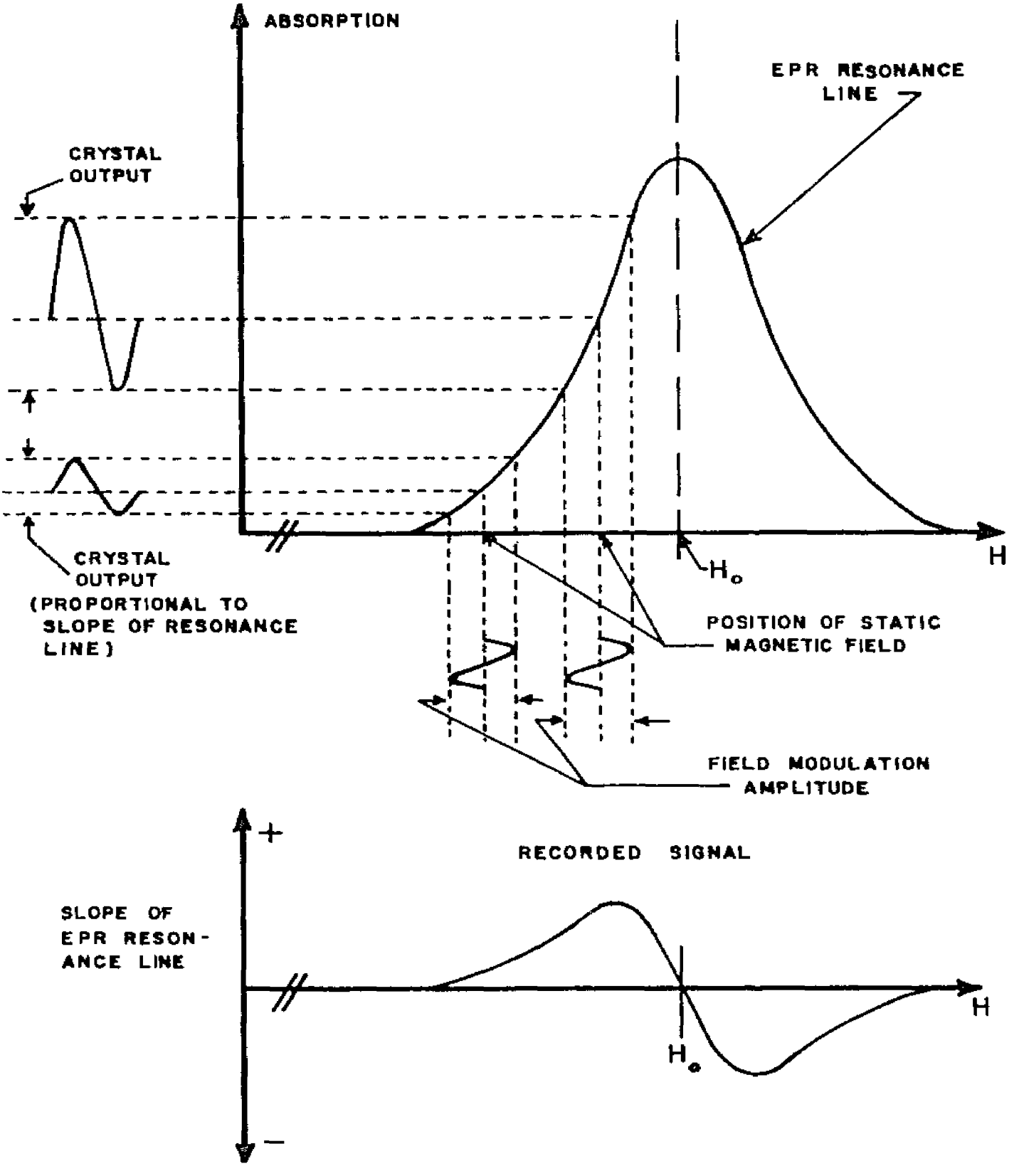

Fig. 9. Output of an EPR spectrometer illustrating why the recorded signal is the first derivative of the absorption line.

general varies between the derivative of a Gaussian line shape and the derivative of a Lorentzian line shape.[11]

Helium Cryostat

In order to study low temperature effects on the EPR signal, some sort of cryostat is necessary. This section describes in detail a cryostat that was designed, built, and successfully employed in the course of the present thesis work. The details of this cryostat were previously published by this author and Y.W. Kim in The Review of Scientific Instruments.[22]

A schematic diagram of the cryostat used for all the 4.2°K measurements is given in Fig. 10. The outer shell of the main body N and the liquid nitrogen reservoir are part of a standard modular cryostat built by Andonian Associates, Inc., Waltham, Massachusetts.

Basic Mechanical Construction

The outer shell of the cryostat tail A is made of brass, and is fastened to the main body by an O-ring seal. The copper radiation shield B is bolted to the bottom of the liquid nitrogen reservoir. The construction allows easy removal of the tail and access to the microwave cavity C and the quartz sample tube D. The cavity and supporting waveguide are bolted to the bottom of the helium well. A 0.635 cm (1/4 inch) o.d. stainless steel coaxial cable tube, a 0.953 cm (3/8 inch) o.d. stainless steel sample tube E, and an X band stainless steel waveguide, all of which pass through the helium well, are soldered in the copper bottom of the helium well and sealed by O-rings at the top. This allows the top works to be easily removed. Figure 11 illustrates a section of the tail taken

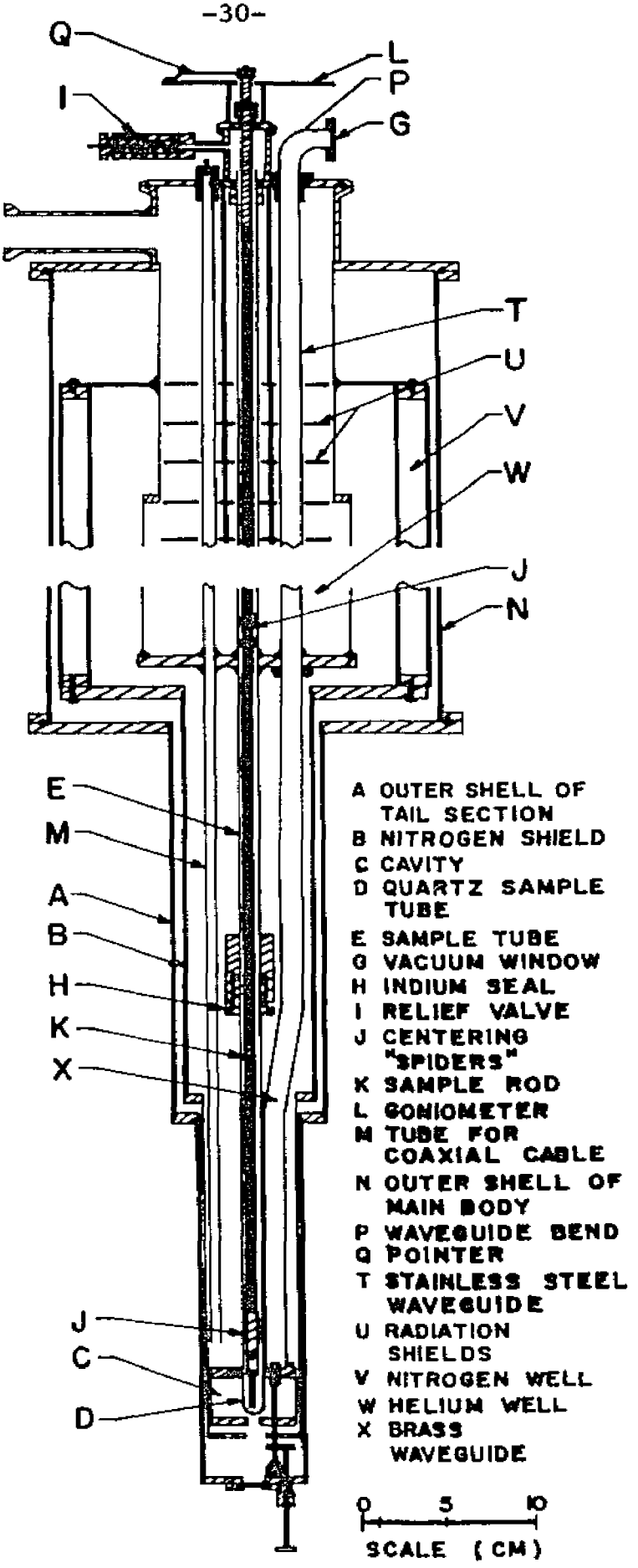

Fig. 10. Scaled schematic drawing of the complete helium cryostat.

at right angles to Fig. 10. It shows an additional 0.953 cm o.d. stainless steel tube F so situated that during transfer of liquid helium the transfer tube extends down to within a centimeter of the cavity. This tube is attached to the relatively massive waveguide and cavity by copper braid at several locations. This technique permits rapid and efficient cooling of the large heat reservoir presented by the waveguide and cavity.

Microwave Assembly

An X band microwave bridge is attached at the top of the cryostat to a 90° E bend P as shown in Fig. 10. This waveguide bend has a vacuum tight window at one end G, and is sealed by an O-ring to the top works of the cryostat at the other end. The same O-ring seals the stainless steel waveguide in the helium well to the top works. This construction allows the entire section of waveguide and the cavity to be part of the vacuum jacket of the cryostat. For rigid construction the waveguide connected to the bottom of the helium well is copper alloy and the cavity is brass. The cavity is cylindrical and operates in the TE_{011} mode. To prevent unwanted modes of oscillation in the cavity the top and bottom of the cavity are electrically insulated from the side wall by Teflon gaskets. The cavity is coupled to the waveguide by a mechanism similar to that of Ager, Cole, and Lambe.[23] The difference is that the electric field in the waveguide is coupled to the magnetic field in the cavity. Figure 12 shows the details of the coupling. A copper wire in a Teflon rod which can be rotated and moved up and down serves to vary the coupling. The Teflon rod extends out through the bottom

of the cavity and is connected to a gear assembly, which subsequently comes out the bottom of the cryostat through an O-ring coupling. The gears unscrew from the tuning rod to allow removal of the liquid nitrogen shield. This arrangement permits the waveguide to be coupled to the top of the cavity and allows the diameter of the cryostat tail to be kept to a minimum. (For rotating magnets the cryostat requires a minimum gap of 7.38 cm and for a fixed configuration of the cryostat and magnet a gap of 6.22 cm is required.)

Optical Characteristics

As seen in Fig. 11, the tail section has three sets of windows Z, two radially opposed sets of windows and a third set on the bottom of the tail. The outer windows are flat quartz disks sealed to the outer shell with rubber O-rings. Since the vacuum jacket is common for the entire cryostat, 0.64 x 1.9 cm rectangular holes in the liquid nitrogen shield B suffice for windows. The radial windows Y in the microwave cavity C are a series of closely spaced horizontal slots in the side wall of the cavity. Since the cavity resonates in the TE_{011} mode, this type of window offers a minimum perturbation to the microwave currents, which travel only in a horizontal direction in the outer wall.[24] The third window is simply a hole in the bottom of the cavity.

Sample Positioning Mechanism

As shown in Fig. 10, the quartz sample tube D, which extends into the cavity, is attached by means of an indium O-ring seal H to the stainless steel sample tube which extends through the helium well

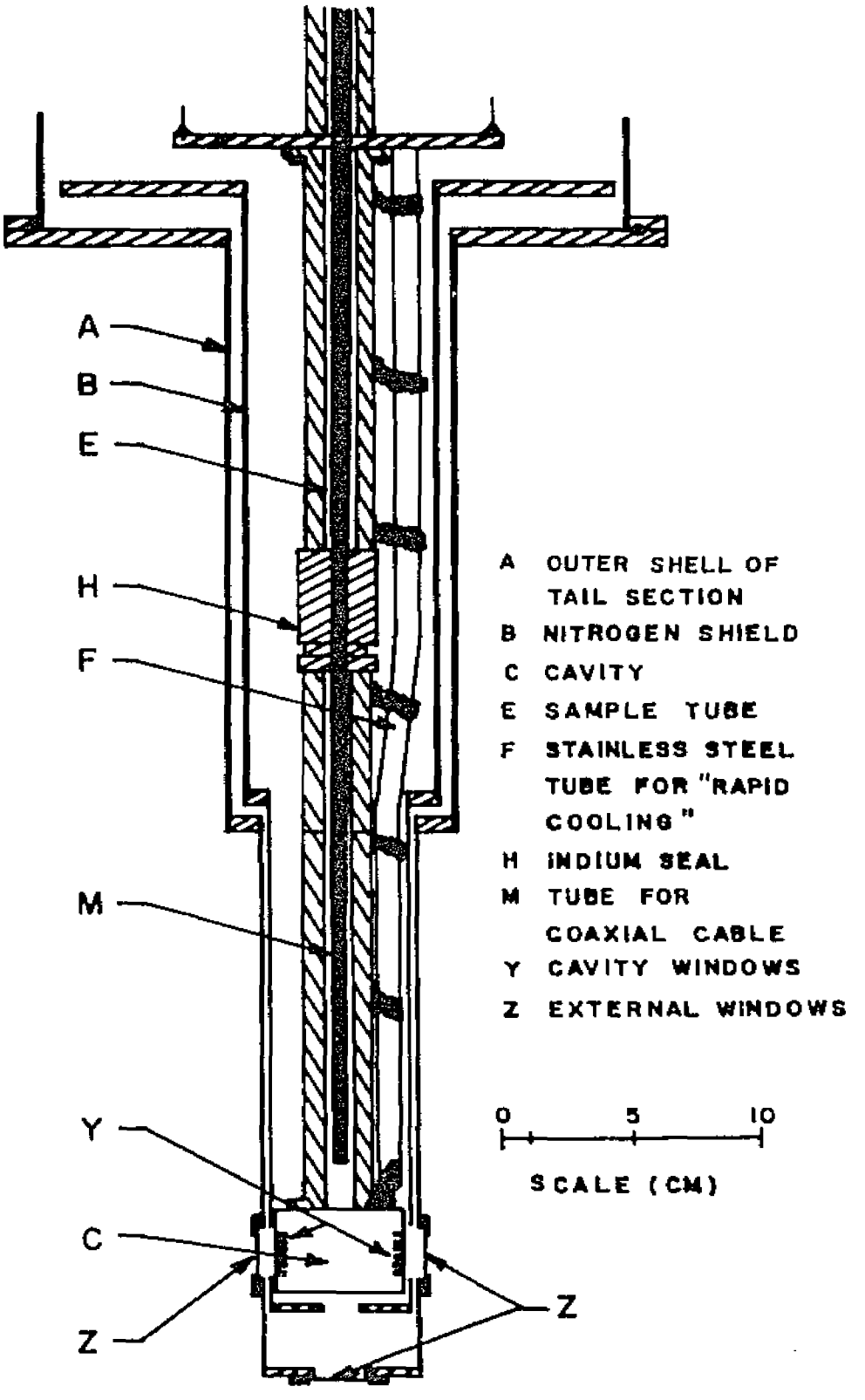

Fig. 11. Section of cryostat tail taken at right angles to the section given in Fig. 10.

to the top works of the cryostat. For operation with a cold finger the quartz tube would be replaced by a copper tube sealed at the bottom and extending down to the top of the microwave cavity. Only the sample, which is attached to the copper, extends into the cavity. At the top of the cryostat is an adjustable relief valve I and a vacuum valve (not shown) for evacuating the sample tube. When using the quartz sample tube, the sample is attached to the end of a 0.635 cm o.d. stainless steel tube K, which extends from the cavity to the top of the cryostat. A pointer Q on top of the sample rod indicates the sample orientation on a goniometer L, on top of the cryostat. The sample rod is kept centered in the sample tube with brass "spiders" J as shown in Fig. 10. The goniometer and the cap on the sample tube are removable to facilitate changing samples. This cap also has three electrical feedthroughs for thermocouple leads or carbon resistor thermometers.

The present experiments require a temperature of 4.2°K. Hence, several small holes have been made in the sample tube in the helium well area to maintain liquid helium in the sample tube. For operation at temperatures above 4.2°K the sample tube would be a closed system. The temperature of the sample would depend on the pressure of helium exchange gas in the sample tube.

ENDOR* Coil

A piece of 0.635 cm o.d. stainless steel tubing M, as shown in

---

* Electron-nuclear double resonance (ENDOR) is discussed in Ref. 11. This section is included in order to present a complete description of the cryostat. ENDOR experiments are not a part of the present thesis.

Fig. 10, carries coaxial cable for the ENDOR coil in the cavity. The coil itself is two or three turns of No. 24 copper wire attached to the quartz sample tube with thin strips of Teflon tape. One end of the coil is grounded in a threaded hole S as shown in Fig. 12. The other end passes through a hole R in the top of the cavity.

Discussion

The modular design of the cryostat makes it extremely versatile and provides several interesting features. First, the tail section is readily removed. If the sample tube must be replaced or exchanged for the cold finger, a vacuum tight indium seal can be made with little or no trouble. Careful cleaning of the surfaces involved is the only precaution necessary. Secondly, the waveguide and cavity are evacuated, thus preventing noise due to boiling liquid helium or foreign material that may be in the helium well. Also, since the cavity is maintained at near helium temperatures, it acts as an effective heat shield for the sample inside the cavity. Thirdly, since a cylindrical cavity is used, the sample, which is on the axis of the cavity, can be rotated in the cavity. The magnet can also be rotated around the cryostat. Furthermore, the sample can easily be removed and another inserted. After changing samples the cavity coupling can be readjusted from outside the cryostat. Fourth, the windows allow for visual alignment of the sample in the cavity. Fifth, when operating with a cold finger, one of the quartz windows could easily be replaced by a beryllium window to allow the sample to be x-irradiated while in the cavity and at low temperatures.

For most efficient use of liquid helium, it has been found that

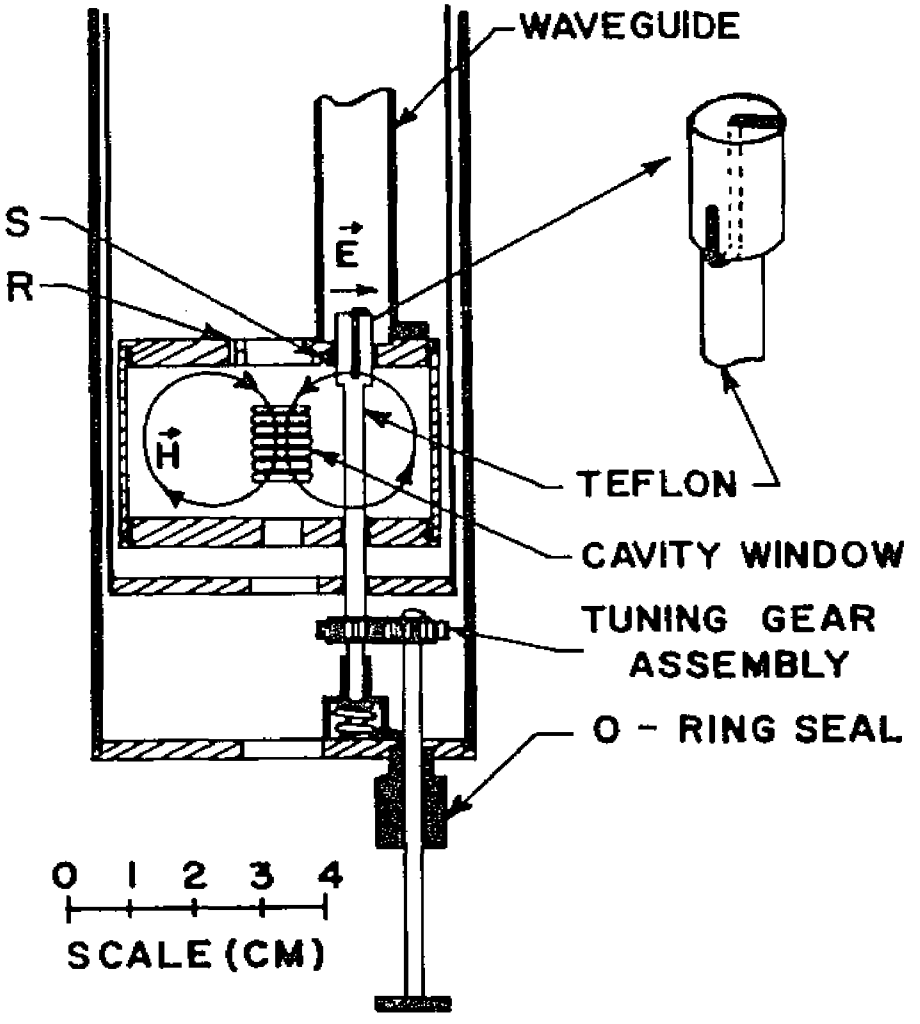

Fig. 12. Details of the microwave cavity and the coupling mechanism.

transferring at a rate of about 6 liters/h into the bottom of the tube F until liquid starts to collect and then transferring at about 1 liter/min gives maximum efficiency. About 3 liters of liquid helium are required to cool the helium well (precooled with liquid nitrogen) to 4.2°K. Styrofoam in the neck of the cryostat prevents the venting helium from freezing out the O-ring seals in the top works during a transfer. The helium well holds about 4 liters. With the three windows open and helium in the sample tube the evaporation rate is about 0.25 liter/h.

CHAPTER IV

ELECTRON PARAMAGNETIC RESONANCE OF Fe^{3+} IN NaF*

Introduction

The work described in this chapter is concerned with EPR absorption studies of iron doped NaF at controlled temperatures below 180°K. It is the purpose of this work to determine the characteristics of iron as an impurity in NaF. The results of this type of study are necessary before an investigation of the effects of iron on the optical bleaching process can be made.

The paramagnetic resonance of iron impurity in NaF has been investigated by Bleaney and Hayes,[25] and Hayes and Jones.[26] These authors have observed an EPR absorption due to Fe^{+} only. The EPR absorption of Fe^{3+} ($^6S_{5/2}$) has been observed in several iron-doped single crystals[27-28] other than alkali halides. However, no successful observation of the EPR absorption of Fe^{3+} seems to have been made in alkali halides.

In the present Chapter, experimental evidences will be presented, which indicate strongly that the ionic state of the iron impurity of NaF may be changed from Fe^{2+} into a singly-ionized state (Fe^{+}) and a triple-ionized state (Fe^{3+}) by means of x-irradiation of the iron-doped NaF. Both Fe^{+} and Fe^{3+} appear to be located substitutionally at cation sites and to interact with the crystalline field as well as the six nearest neighbor fluorine ions. In particular, the interaction of the Fe^{3+} ion with its environment is remarkably

---

* The content of this Chapter is based on a manuscript submitted to the Physical Review by this author and Y.W. Kim.

temperature-dependent. The spin Hamiltonian for the Fe^{3+} has been determined in such a way that it can account for the observed temperature dependence. The results are compared with the current theory of the fine structure splitting of S-state ions.

Experimentals

Single crystals of NaF were obtained from the Harshaw Chemical Co., Cleveland, Ohio. Mass spectroscopic analysis* of these crystals indicated that the crystal samples contained 8 parts per million (ppm) of iron, 3 ppm of manganese, but no detectable amount of chromium (<1/10 ppm). Samples of dimensions approximately 3mm x 3mm x 15mm were cut from these crystals in such a way that the longest dimension of the samples is parallel to the [110]-direction.

The samples were then irradiated by x-rays from a molybdenum target tube operated at 50 Kv and 20 ma for about 90 hours at room temperature.

The (EPR) spectra of these samples before and after the irradiation were investigated near 77°K and 4.2°K. The EPR spectrometer used for these studies is a Varian model V4500 X band spectrometer with 100 kcps and audio frequency magnetic field modulation (See Chapter III). The liquid helium cryostat described in Chapter III has been employed for parts of the present work.

The angular dependence of the spectra is investigated by rotating the samples about the [110]-axis which is held perpendicular to the D.C. and microwave magnetic fields. The angle (θ) of rotation is measured from the [110]-direction of the samples to the direction

---

* Spectroscopic analysis was performed by the Harshaw Chemical Co.

of the D.C. magnetic field, which remains on the (110)-plane.

Experimental Results and Spin Hamiltonian

The samples have yielded weak EPR spectra of the 3 ppm of manganese impurity before the x-irradiation, but no trace of the EPR absorption of the 8 ppm of iron impurity. The lack of the resonance of the iron impurity is not unexpected, since the iron enters the lattice of NaF as a divalent ion[29] (Fe^{2+}) and the EPR resonance of Fe^{2+} is very sensitive to the lattice defects,[30] making the width of the resonance so broad as to be practically unnoticeable.

The x-irradiation has been found to reduce the intensity of the manganese resonance to practically nil, and to induce three EPR spectra which are easily distinguishable at different temperatures.

Near 77°K, only two of them are observable. One represents the well-known F center resonance.[31] The intensity of this F center resonance, however, can be reduced substantially by optically bleaching the x-irradiated samples with F-light (340 mμ). After the optical bleaching, then, the other of the two spectra is better identified. This second spectrum is centered approximately at $g = 2.002$, and exhibits a partially resolved anisotropic structure. The solid curves of Fig. 13 illustrate four spectra recorded at $\theta = 0°$, 34°, 55°, and 90°. $\theta = 0°$, 55°, and 90° correspond to [100], [111], and [110] respectively. The best resolution is obtained for $\theta = 34°$ and 90°, while poorer resolutions are noticed for $\theta = 0°$ and 55°. For the orientations of best resolution, the spectrum consists of seven lines, which are approximately equally spaced (13.7 gauss apart). The intensity ratio of the seven lines is approximately 1:6:15:20:15:6:1.

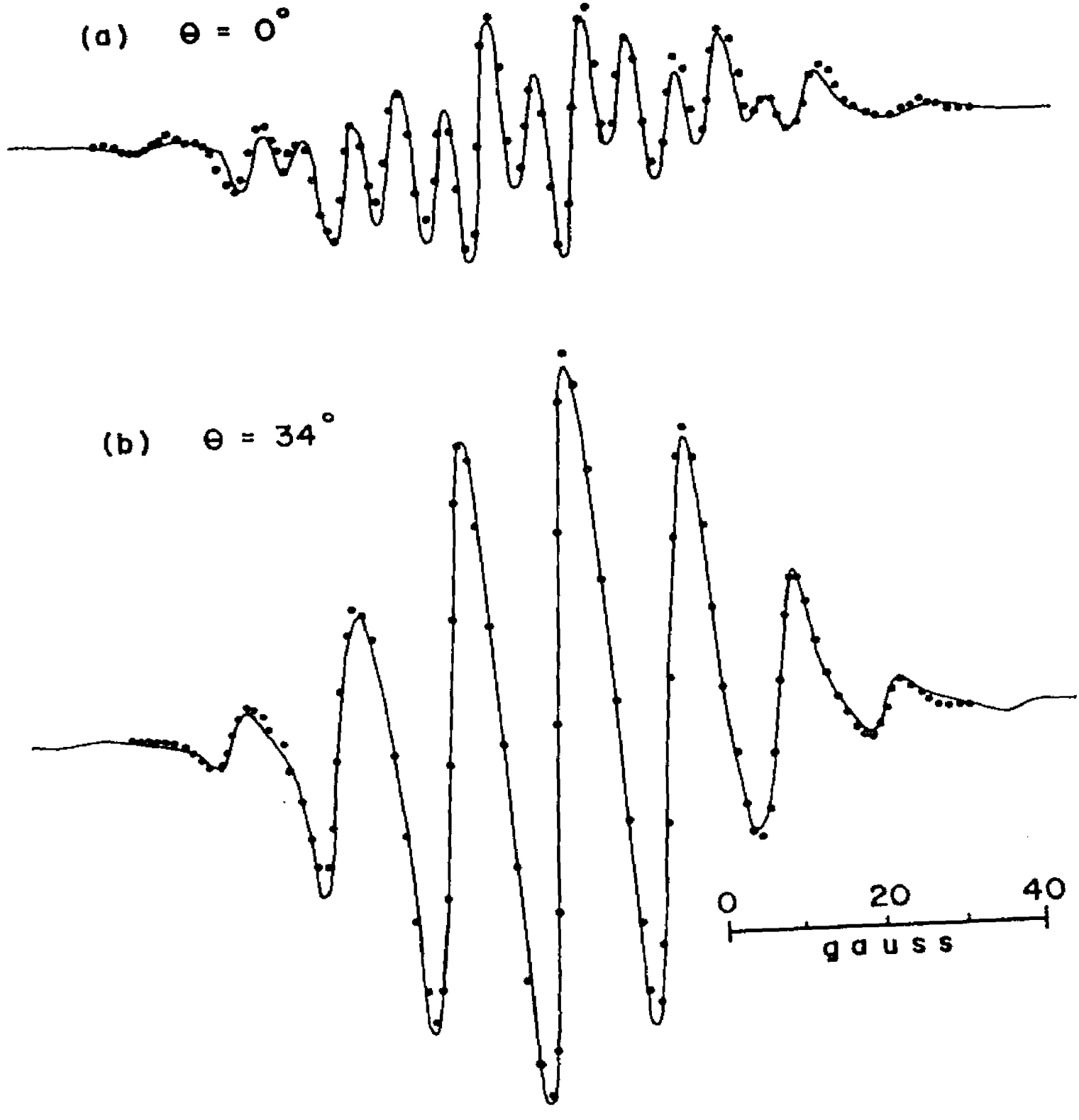

Fig. 13. The observed EPR spectra (solid lines) and the theoretical fit (dots) of Fe^{3+} in NaF at 77° for θ = 0°, 34°, 55°, and 90°. (Continued on next page.)

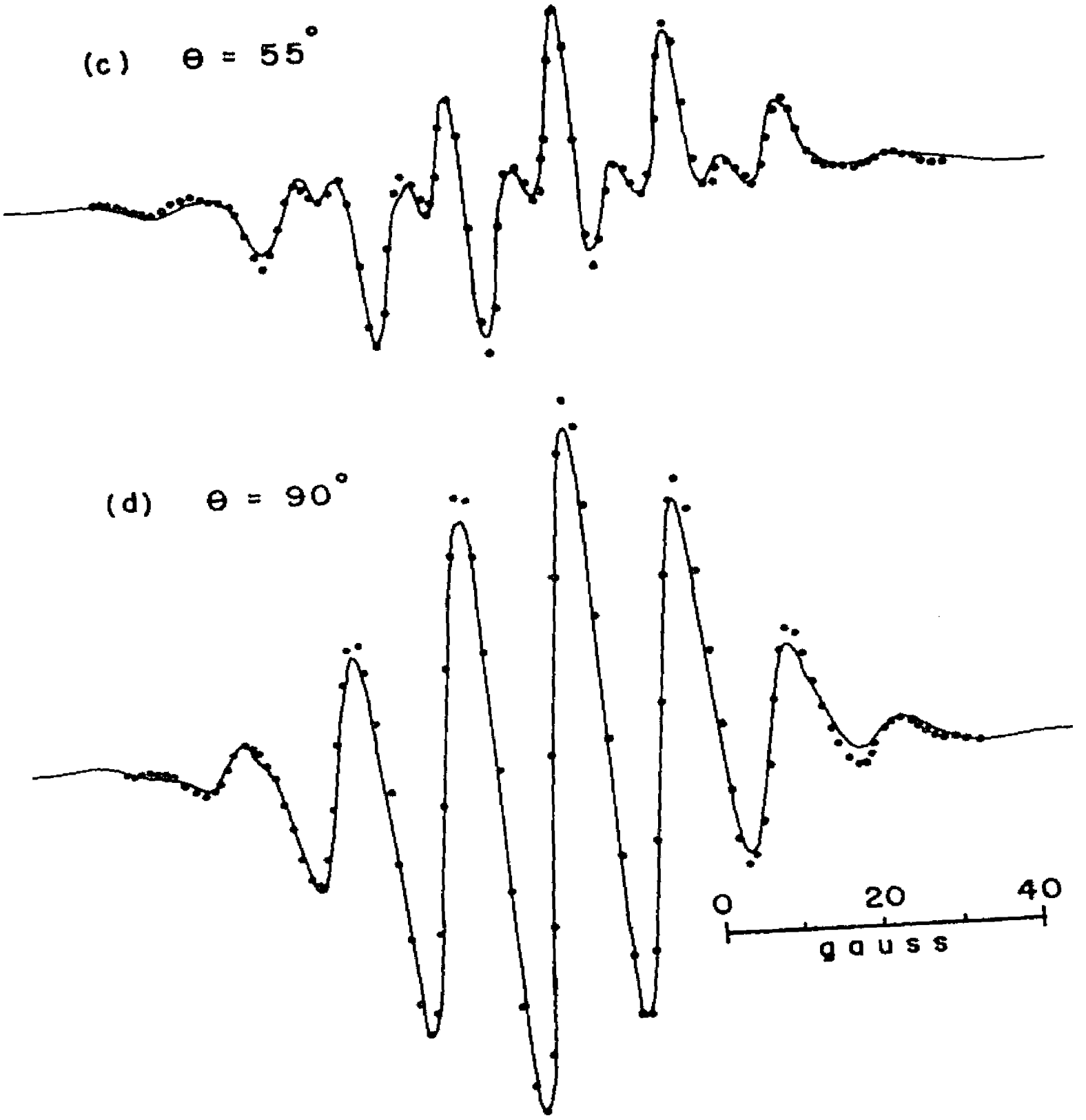

Fig. 13. (Continued).

Near 4.2°K, the second spectrum is not observable, and the F center resonance has been already reduced by the optical bleach. Instead, a third spectrum with a partially resolved anisotropic structure is noticed. This one is centered near g = 4.344. The anisotropy of this spectrum is different from that of the second spectrum, and has been found to be satisfactorily described in terms of the spin Hamiltonian that Bleaney and Hayes[25] previously assigned to Fe^+ located at a cation site in NaF. In the remaining part of this paper, therefore, only the second anisotropic spectrum will be dealt with.

As preliminary clues to the determination of the proper spin Hamiltonian for describing the spectrum, two points of observation have been used: First, the intensity ratio of the seven lines mentioned in the preceding is very close to that which would be expected from six equivalent nuclei of spin I = 1/2, each interacting with the paramagnetic ion responsible for the spectrum. In the present case, Na^{23} and F^{19} are both 100% naturally occurring isotopes with nuclear spins of 3/2 and 1/2 respectively. This suggests that the paramagnetic ion is situated on a cation site with cubic symmetry and interacts with six equivalent nearest-neighbor fluorine ions. Secondly, if the resolved spectrum is due solely to the hyperfine interaction (see Appendix I), the resolution should be best for $\theta = 55^\circ$, when the anisotropic part of the hyperfine interaction vanishes and leaves only seven lines.* However, this is not the case (see Fig. 13). Instead,

---

* This is the case for cubic symmetry when $\vec{H}$//[111]; then $(3\cos^2\theta_n - 1) = 0$ for n = 1, ..., 6.

the observed angular dependence of the resolution appears to be more similar to what would be expected from unresolved fine structure splitting (see Appendix II) of an ion in the $^6S_{5/2}$ state.[32] Thus, the spin Hamiltonian for the spectrum is taken to be:

$$\mathcal{H}_s = g\beta \vec{H} \cdot \vec{S} + \sum_{n=1}^{6} \vec{S} \cdot \underline{A}_n \cdot \vec{I}_n + F(a) \quad . \tag{10}$$

The first term of Eq. (10) describes the Zeeman interaction of the electron spin (S = 5/2) with the magnetic field H, where the spectroscopic splitting factor g = 2.002, and β is the electronic Bohr magneton. The second term of Eq. (10) denotes the summation of the hyperfine interaction tensor $\underline{A}_n$ of the n-th fluorine nucleus of spin I_n(=1/2) over the six nearest neighbor fluorine nuclei.

Since the paramagnetic ion is on a cubic lattice site, each of the hyperfine tensors is axially symmetric and the hyperfine term can be written as follows (see Appendix I):

$$\sum_n I_{nz}, S_z, [\delta + \gamma (3 \cos^2\theta_n - 1)] \tag{11}$$

where the subscript z' refers to the direction of the external field along which $\vec{S}$ and $\vec{I}_n$ are quantized,[3] and θ_n is the angle between the direction of the magnetic field and the axis joining the n-th fluorine nucleus to the paramagnetic ion. The two Greek letters δ and γ represent the isotropic and anisotropic (hyperfine) coupling constants respectively.

The third term of Eq. (10) is the fine structure term for the $^6S_{5/2}$ ion in a cubic crystalline field. It has the following form (see Appendix II):

$$F(a) = (1/6)\ a[S_x^4 + S_y^4 + S_z^4 - (1/5)\ S(S+1)(3S^2+3S-1)] \qquad (12)$$

where the suffices x, y, and z refer to the crystalline axes, and a is the fine structure constant. The fine structure term depends only on the electron spin operators, and splits transitions between the electron spin levels as follows (see Appendix II):

$$M_s = \pm 1/2 \rightarrow \mp 1/2: \quad H = H_0 \qquad (13)$$

$$M_s = \pm 3/2 \rightarrow \pm 1/2: \quad H = H_0 \pm (5/2)\ p\ (a/g\beta) \qquad (14)$$

$$M_s = \pm 5/2 \rightarrow \pm 3/2: \quad H = H_0 \pm 2\ p\ (a/g\beta) \qquad (15)$$

where $H_0 = \frac{h\nu}{g\beta}$, ν being the fixed microwave resonance frequency, and $p = (1/5)\ (\ell^2m^2+m^2n^2+n^2\ell^2)$ with ℓ, m, n the direction cosines of $\vec{H}$ referred to the cubic axis of the crystal. The transitions given by Eqs. (13), (14), and (15) have an intensity ratio of 9:8:5 respectively.

Using the spin Hamiltonian given in Eq. (10), theoretical spectra were calculated with the aid of an IBM 7074 computer (W.S.U. Computing & Data Processing Center, Detroit, Michigan). The first step in this calculation is to determine the magnetic energy-level structure of $\mathcal{H}_s$. The Zeeman term yields six equally spaced electron spin levels and each of them is split into the nuclear hyperfine structure determined by the hyperfine term. In general, there are 64 hyperfine levels, each corresponding to one of the $(2I_n + 1)^6$ possible orientations of the six nuclear spins, each $I_n = 1/2$. Finally, the fine structure term splits each of these into five levels. From this structure, then, the energy separation, ΔE_i, of all the allowed transitions is determined along with the magnetic field value $H_i = \Delta E_i/g\beta$, at which the transition will take place. Knowing all possible values of H_i it is then possible to

construct a theoretical spectrum. Using the magnetic field, H, as the abscissa, the derivative of a Gaussian line,* which has a width, W, between the points of maximum slope, is placed at all values of H_i. Each of these Gaussian lines is weighted by the appropriate intensity factor. The individual Gaussian derivative curves are then superimposed and added togther at .5 gauss intervals to obtain the overall composite spectrum. The interval of summation (.5 gauss) is chosen to obtain the maximum resolution in the computed spectrum. The structure and anisotropy of the computed spectrum naturally depends on the values of the parameters (δ, γ, a, and W). These parameters are varied over wide ranges, so that the resulting computed spectra fit well the observed spectra. Two facts are especially helpful in determining the best fit: (1) for $\theta = 55^\circ$ the anisotropic hyperfine interaction vanishes and has no effect on the spectrum, and (2) for $\theta \simeq 30^\circ$ the fine structure splitting vanishes+ ($p = 0$) and a has no effect on the spectrum.

The results of this computer fit for the observed spectra at 77°K are illustrated in Fig. 13, where the spectra for four values of θ (0°, 34°, 55°, and 90°) are compared. The solid lines are the observed spectra and the dots represent the computed spectra. The values of the spin Hamiltonian parameters which gave this fit are given

---

* Gaussian shaped lines were used in this calculation since there is probably some broadening due to the hyperfine interaction with next nearest neighbor nuclei. Also, the individual lines making up the composite spectra are probably broadened by thermal vibrations as will be shown later on in this chapter.

+ Experimentally the spectra reaches a maximum amplitude for θ near 34° even though the fine structure disappears near 30°. This is probably due to the anisotropic hyperfine interaction which is decreasing at this point and vanishes when $\theta = 55^\circ$.

in Table 1. The agreement between the observed spectra and the calculated spectra is remarkably satisfactory and justifies the reasoning that led to the choice of the electronic state of the paramagnetic ion ($^6S_{5/2}$) in a cubic site and its spin Hamiltonian.

Temperature Effects

As the temperature of the samples is raised from 77°K to 180°K,* the features of the spectra for different angles change quite rapidly and significantly. For example, near 180°K, the spectra for all values of θ tend to show only a seven-line pattern as is observed for $\theta = 90^\circ$ at 77°K, and there is an accompanying decrease of the spectral amplitude. The solid curves of Fig. 14 illustrate the spectra for $\theta = 55^\circ$K and $\theta = 90^\circ$ near 180°K, and the solid curves of Fig. 15 show the observed temperature dependence of the amplitude of the two spectra in Fig. 14.

A comparison of the spectrum for $\theta = 55^\circ$ of Fig. 14, for example, with the corresponding spectrum in Fig. 13 would indicate easily the interesting effect of the temperature change. The structural change of the spectra at 180°K indicates that the spin Hamiltonian parameters are changing and that the temperature effect is not solely due to the Boltzmann temperature dependence of the spin level population. Another evidence in support of this view is given by the observed temperature dependence of the spectral amplitude. The portion of the amplitude change due to the Boltzmann temperature dependence (of the spin level populations) can be readily removed by means of a correction factor.

---

* At higher temperatures, the spectral intensity at $\theta = 0^\circ$ becomes quite small and weak signals due to unidentifiable impurities make a detailed analysis of this spectrum difficult.

TABLE 1

SPIN HAMILTONIAN PARAMETERS FOR THE OBSERVED RESONANCE DUE TO Fe^{3+} IN NaF AT 77°K

g	$2.002 \pm .001$
a	$2.29 \pm .05$ 10^{-4} cm^{-1} (2.45 gauss)
δ	$12.80 \pm .03$ 10^{-4} cm^{-1} (13.7 gauss)
γ	$1.7 \pm .1$ 10^{-4} cm^{-1} (1.8 gauss)
W	4.69 gauss

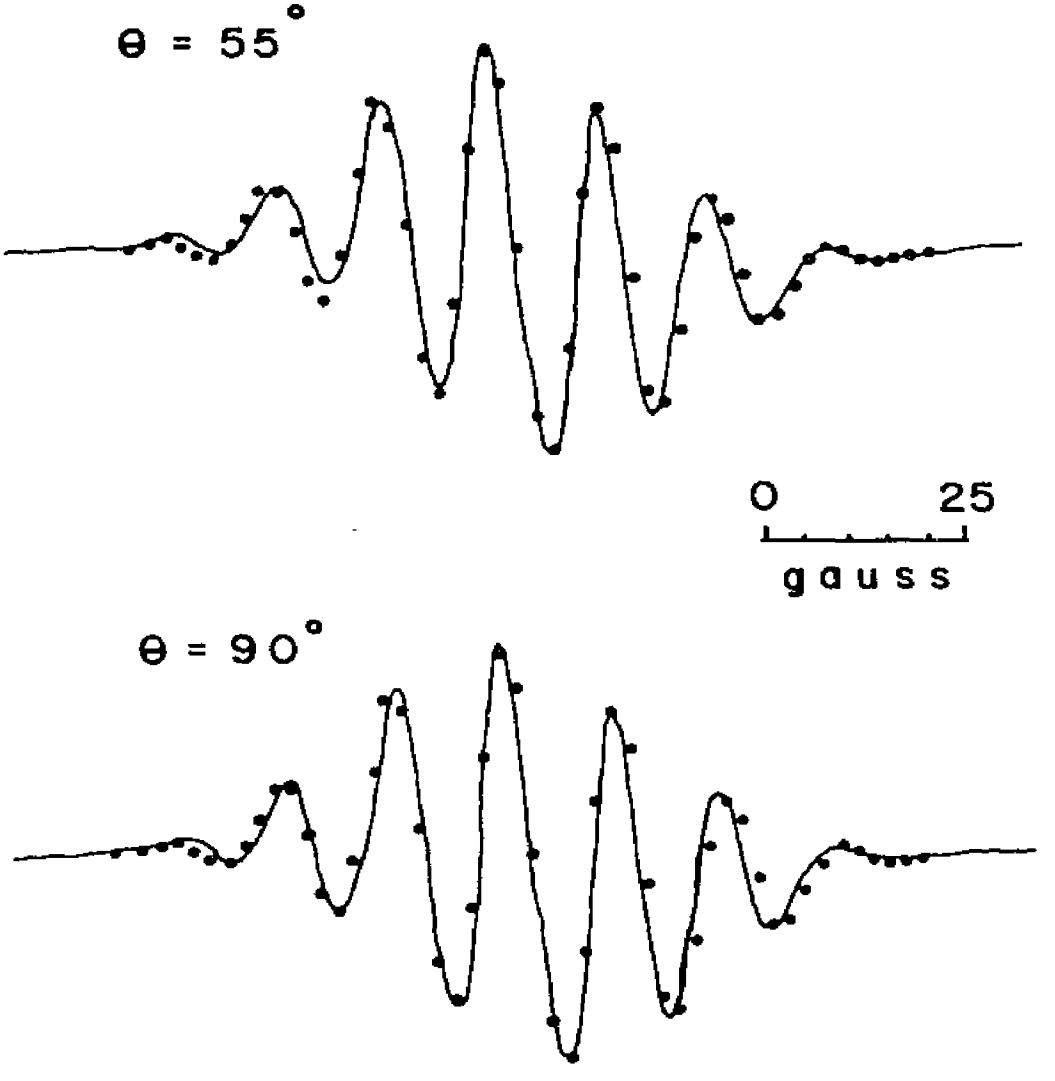

Fig. 14. The observed EPR spectra (solid lines) and the theoretical fit (dots) of Fe^{3+} in NaF near 180° for $\theta = 90°$ and $\theta = 55°$.

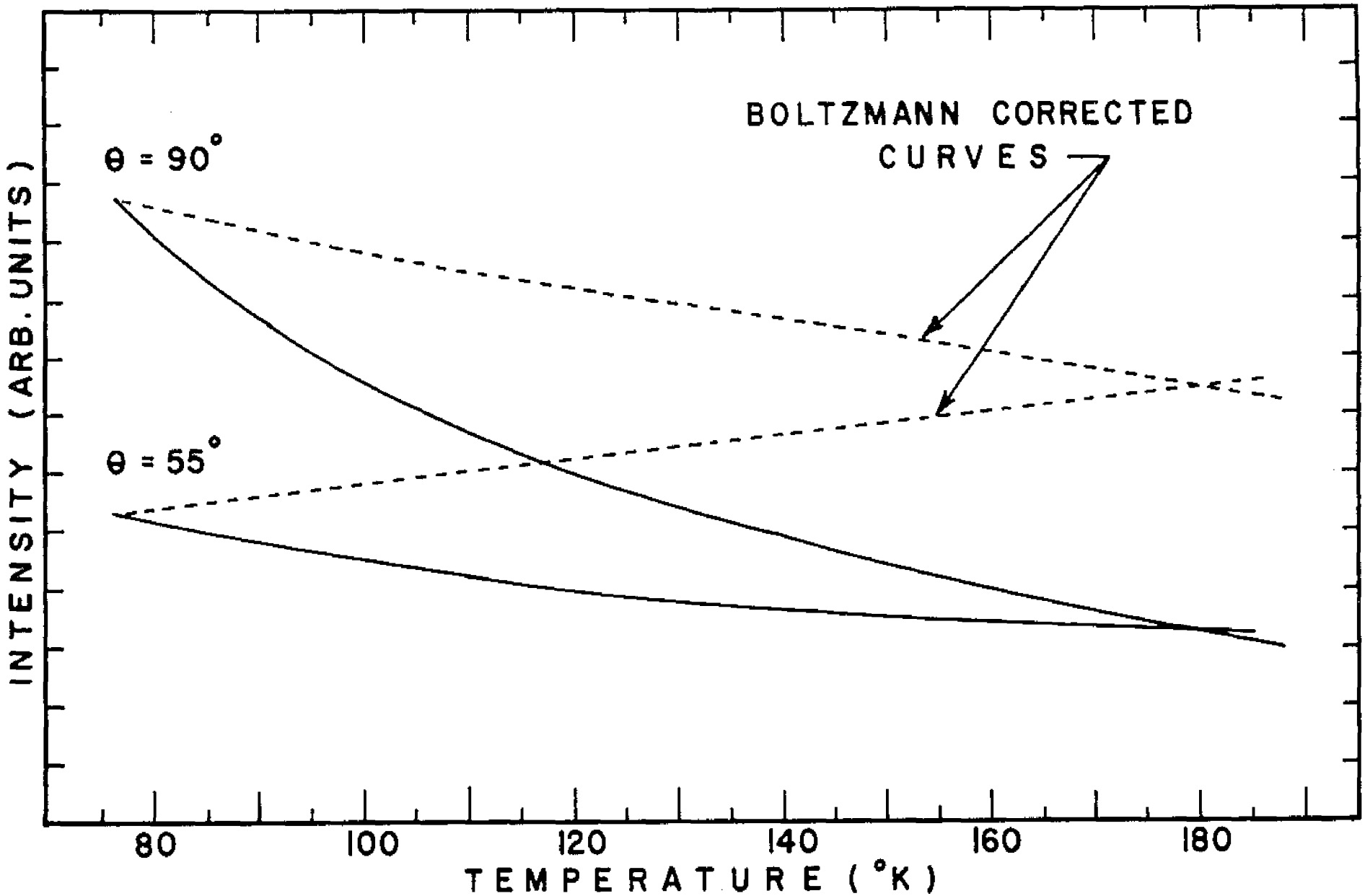

Fig. 15. The observed temperature dependence of the EPR spectral amplitude for $\theta = 90^{o}$ and $\theta = 55^{o}$ (solid curves). The dashed curves represent the experimental curves corrected for the Boltzmann temperature dependence.

When the correction is made, the solid curves in Fig. 15 should behave like the two dashed curves. If the amplitude change were due solely to the Boltzmann temperature dependence, the dashed curves would have to be horizontal. The fact that they are not indicates that the spin Hamiltonian parameters and/or W are changing, as the temperature is varied.

A major consideration in the computer analysis of the temperature dependence of these spectra is, therefore, that the computed spectra show only the basic seven-line pattern near 180°K and that the anisotropy of the computed spectra corresponds to the observed anisotropy. Otherwise, theoretical spectra for the higher temperatures were calculated in the same way as described previously for the 77°K spectra by adjusting the values of a, γ, and W. All the computed spectra were normalized so that the area under the absorption curve remained constant for changes in W.

The computation results have indicated that the observed change in the structure and amplitude of the spectra for different temperatures is primarily due to the temperature dependence of a and W, and slightly due to γ, while g and δ appear to remain constant within experimental errors. The results of the computation are illustrated by the dots in Fig. 14. The agreement is satisfactory. Figure 16 illustrates the computed temperature dependence of a, W, and γ, which has been found to be satisfactory to account for the observed temperature dependence of the spectra. Three points of significance should be noticed: First, a decreases practically linearly as T increases. Second, W is found to be proportional to the square root of T. Third,

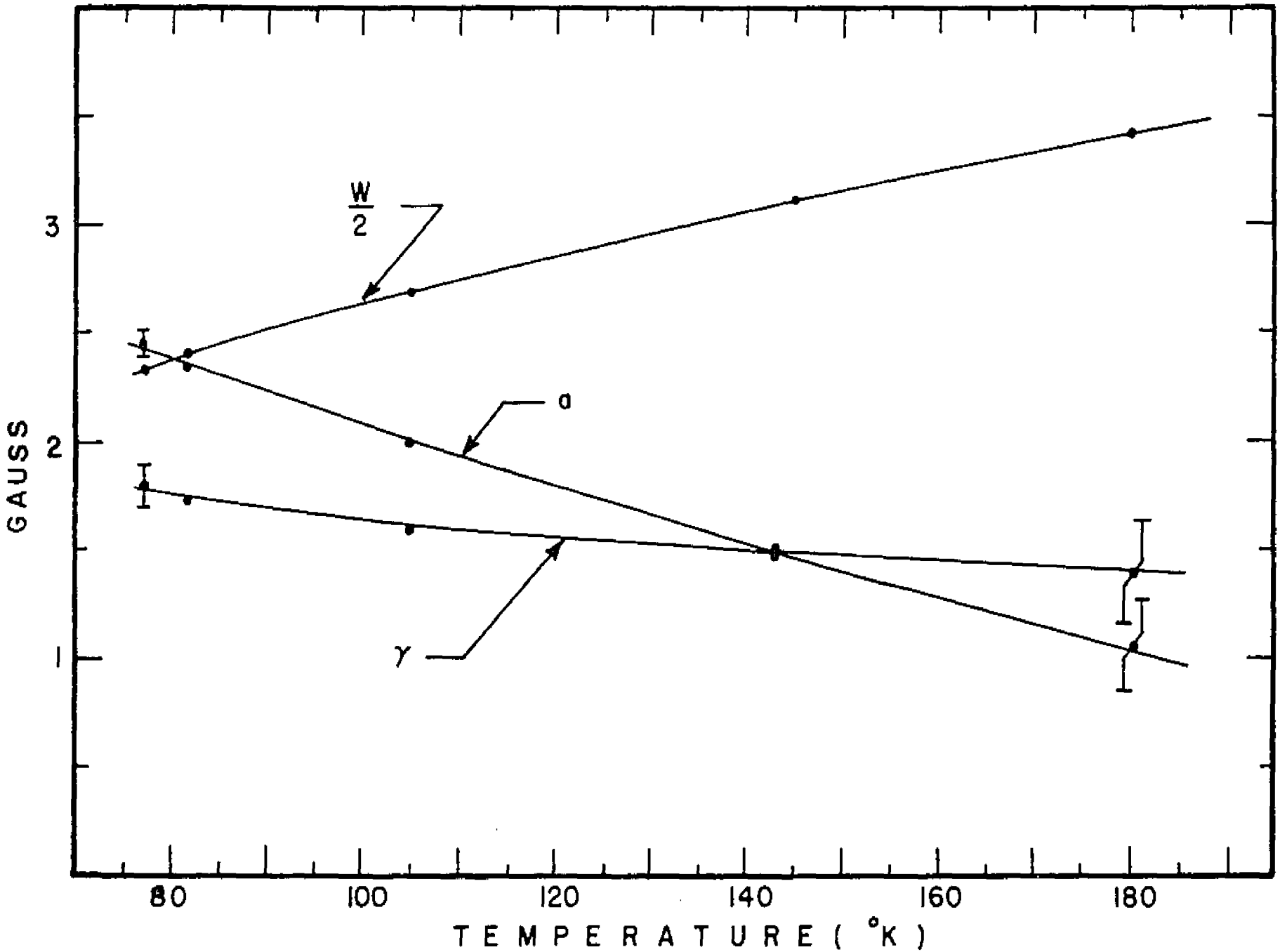

Fig. 16. The temperature dependence of a, γ, and W found by fitting the experimental data at several temperatures. ε and δ are found to be constant within experimental error.

γ tends to decrease as T increases, but the large error in the computational difficulty makes it doubtful whether the change of γ is significant, as compared with the change of a and W.

Discussion

The results of the analyses in the preceding show that the choice of the electronic state ($^6S_{5/2}$) of the paramagnetic ion, its location at a cation site surrounded by a cubic field, and the accompanying spin Hamiltonian Eq. (1) is very satisfactory in accounting for the anisotropy of the spectra as well as for the temperature dependence of the spectra.

Each of the three metallic impurities (iron, manganese, and chromium) of the NaF samples investigated in the present work can exist in the $^6S_{5/2}$ electronic state: Fe^{3+}, Mn^{2+}, and Cr^{+}. Of the three possibilities, Fe^{3+} is most favorable. The following reasons may be cited. First, Mn^{2+} has a nuclear spin of 5/2 and a large nuclear magnetic moment, which would lead to a large hyperfine splitting of the spectra and would contribute to the spin Hamiltonian in Eq. (1) an additional term representing the hyperfine interaction of the electronic spin with the nuclear spin of Mn^{2+}. This additional term would then lead to a hyperfine splitting ($\sim$90 gauss) of the spectra, which is not the case in the present work. Furthermore, the x-irradiation has reduced the resonance of Mn^{2+} practically to nil (see Section on Experimental Results and Spin Hamiltonian). Secondly, the concentration of the chromium impurity is too small (less than one-tenth ppm), to be responsible for the spectra, since the observed spectra corresponds to a concentration of at least 1 ppm of impurity. Thirdly, the parametersfor Cr^{+} in NaF reported by Hayes and Jones[26] are not the

same as the parameters determined in the present work.

The ionic radius of an Fe^{3+} ion is relatively small (0.6Å)[33] and the interatomic spacing of the NaF lattice is 2.31Å. This might lead one to speculate that the Fe^{3+} should be located in an interstitial position as it is in AgCl.[27] The conclusion in the present work that it is not in an interstitial position is probably attributable to the stability[34] of the complex $(FeF_6)^{3-}$. This complex puts the iron in a lattice site with cubic symmetry.

To preserve local electrical neutrality in the lattice, each Fe^{3+} should produce two cation vacancies. These vacancies will cause departures from cubic symmetry at the Fe^{3+} site (see Fig. 17(a)), if they are close to the Fe^{3+} site forming a complex. This would introduce additional non-cubic terms into the spin Hamiltonian, Eq. (10). Since the resonance can be fit by only cubic terms, the charge compensating vacancies are not "bound" to the Fe^{3+} site (see Fig. 17(b)).

The computed temperature dependence of a and W (see Fig. 16) facilitates some discussions with regard to the mechanism of the line broadening, and the existing theoretical expression for a.

First, as mentioned in the preceding, the line width W is fairly well proportional to $(T)^{1/2}$, where T is the temperature. This dependence may be explained in terms of the thermal vibration of the ions neighboring the Fe^{3+} ions. The thermal vibration is expected to cause fluctuations in the zero-field splitting,[35] which is measured by a. Thus, in a simple approximation, the rms fluctuation of a, say Δa, can be taken to be a measure of W, and it can be taken to be proportional to the rms amplitude of the thermal vibration, say Δx. Therefore, W becomes proportional to Δx. Now, the average energy of an ion in

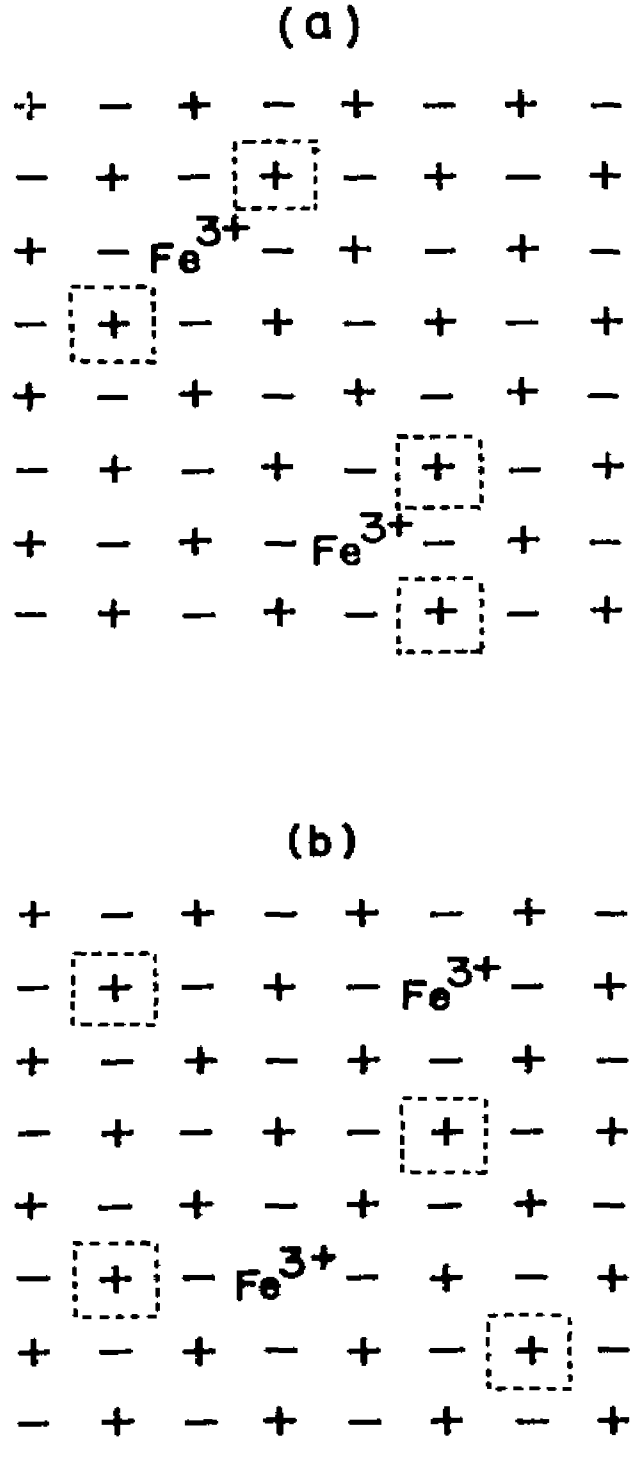

Fig. 17. Schematic diagram showing (a) associated charge compensating cation vacancies in next-nearest neighbor positions forming a "complex," and (b) charge compensating vacancies away from the Fe^{3+} ion. In this case the Fe^{3+} ions are left in a site with cubic symmetry and the vacancies are free to migrate at sufficiently high temperatures depending on the activation energy.

thermal vibration is proportional to $(\Delta x)^2$ and also to T. Therefore, W becomes proportional to the square root of T.

Secondly, the fine structure constant, a, decreases as T increases. This tendency is consistent with the existing speculation.[36] The decrease of a is practically linear in T. This linear relation leads to a linear dependence of a on the lattice constant d, for the case of the linear expansion of the lattice. Such a relationship between a and d is expected of the lattice. Such a relationship between a and d is expected from the discussions in the preceding. Quantitatively, however, the amount of change (approximately 60%) of a between 77°K and 180°K does not appear to be easily compatible with the existing theories on a. According to the theories on the S-state ions, the fine structure constant is given in a certain approximation by the following:[37]

$$a = \frac{K\lambda^4}{E_{PS}^4} \tag{16}$$

where K is the matrix element of the potential V of the cubic crystalline field, and E_{PS} and λ are the energy spacing between the ^4P and ^6S states of the free Fe^{3+} ion and the spin-orbit coupling constant respectively. Since E_{PS} refers to the free ion, the temperature dependence of a must come from K and/or λ, according to Eq. (16). Of the two, K and λ, the latter seems to be less significant in the T-dependence of a. The reason is the following. Experimentally, the spectroscopic splitting factor, g, is practically insensitive to temperature changes in the range between 77°K and 180°K. This means that the change of λ over the same temperature range, if any, is not significant. Thus, K becomes the major factor to produce the temperature dependence of a. The wave function used for the matrix element is more or less insensitive to the temperature change.

Consequently, possible T-dependence of K originates from the temperature dependence of the cubic field potential V. Simple calculations by means of Eq. (16) and a linear thermal expansion of the lattice produce about 2 to 3% change of a over this temperature range. This is just too small to account for the observed change (60%) of a. It appears that in order to account for the large change of a, a should be determined primarily by at least a third order perturbation in the crystalline field.[38]

Conclusion

EPR studies of x-irradiated single crystals of NaF containing iron as an impurity have been conducted near 4.2°K and at temperatures between 77°K and 180°K.

Three (EPR) spectra with isotropic g values have been distinguished: One is the well-known F center spectrum; the second is centered near $g = 2.002$, and exhibits a partially resolved structure which is anisotropic; the third is centered near $g = 4.334$, and corresponds to the Fe^+ spectrum that was previously determined by Bleaney and Hayes.[25] The first two spectra are readily observable near 77°K, while the Fe^+ spectrum is observed near 4.2°K.

The observed anisotropy of the second spectrum has been successfully described in terms of a spin Hamiltonian consisting of (i) a Zeeman term for an effective spin $S = 5/2$, (ii) a fine structure term for an S-state ion located at the center of a cubic crystalline field, and (iii) a hyperfine interaction term pertaining to six equivalent nuclei of spin 1/2 each. The spin Hamiltonian has lead to the identification of the ion responsible for the spectrum to be $Fe^{3+}(^6S_{5/2})$ located at a cation site, interacting with the cubic crystalline field

and with the nearest neighbor fluorine nuclei. The results indicate that the charge-compensating vacancies (two cation-ion vacancies per Fe^{3+}) are far from the site of Fe^{3+} and do not disturb the cubic crystalline field surrounding Fe^{3+}.

As the temperature is raised from 77°K to 180°K, the Fe^{3+} spectrum changes in both its structure and amplitude. Computer analyses of the observed temperature dependence have indicated that the changes are due primarily to the temperature dependence of the fine structure constant (a), and the width (W) of the individual lines composing the Fe^{3+} spectrum. The analyses also have yielded that a decreases almost linearly by approximately 60% over the temperature range and W increases as the square root of the temperature.

The results are consistent qualitatively with the existing theories of the S-state ion. Quantitatively, however, the change (60%) of a from 77°K to 180°K is just too big to be satisfactorily accounted for by the corresponding change (2% to 3%) expected from the theoretical expression for a. Similar studies on S-state ions are being conducted in order to examine further this point of concern.

CHAPTER V

IRON IMPURITY CONTROLLED F TO M CONVERSION IN X-IRRADIATED NaF*

The EPR investigations described in Chapter IV have shown that iron entering the NaF lattice as a divalent ion can be transformed into Fe^{3+} or Fe^{+} by x-irradiation. Among other things, the presence of these ions has indicated that these samples have an excess of cation vacancies, which are free to migrate in the lattice. Optical bleaching of these samples can now be compared to samples without the iron impurity. The results of these studies can be used to determine how the iron impurity affects the optical bleaching mechanism.

Introduction

The mechansim that governs the optical bleaching has been the subject of several recent papers.[39-45] An interesting review of the subject has been given by Compton and Rabin.[5] Two mechanisms appear to be in general use, one proposed by Lüty[39] and the other by Delbecq.[41] Lüty's mechanism consists of the following steps: (1) the F-light dissociates an F center into an α center (anion vacancy) and an electron (e^-), (2) the electron is trapped at another F center to form an F' center (a negatively charged F center), and (3) the α center migrates to the F' center to form an M center. The three steps are schematically represented as follows:

---

* The content of this chapter is based on a manuscript submitted to the Physical Review by this author and Y.W. Kim.

$$(1)\quad F + h\nu_F \rightarrow \alpha + e^- \quad , \tag{17}$$

$$(2)\quad F + e^- \rightarrow F' \quad , \tag{18}$$

$$(3)\quad \alpha + F' \rightarrow M \quad , \tag{19}$$

where h and ν_F are Planck's constant and the frequency of the F-light respectively. On the other hand, Delbecq's mechanism differs from LÜty's with respect to the second and third steps as follows:

$$(1)\quad F + h\nu_F \rightarrow \alpha + e^- \quad , \tag{20}$$

$$(2)\quad \alpha + F \rightarrow F_2^+ \quad , \tag{21}$$

$$(3)\quad F_2^+ + e^- \rightarrow M \quad . \tag{22}$$

In other words, the α center formed in step (1) migrates to an F center to form an F_2^+ center (step (2)), which subsequently traps an electron to become an M center (step (3)).

Neither of the above mentioned mechanisms considers possible implication of any kind of impurity in the bleaching process. On the other hand, for example, an involvement of anion-cation vacancy pairs in an early stage of optical bleaching of x-irradiated KCl has been suggested by Bron and Nowick.[45] However, the nature of the source for the cation vacancies has not been actually understood.

A source of cation vacancies in alkali halide crystals can be provided by a concentration of foreign metallic ions introduced in the crystals. For example, consider iron impurity in NaF. If the iron impurity is in the triply ionized state (Fe^{3+}), for instance, then two cation vacancies per Fe^{3+} have to be produced in the lattice so that the charge neutrality of the lattice is maintained. Whether or not the two cation vacancies are tightly bound to the Fe^{3+} to form

a complex can be determined by investigating the crystalline field of Fe^{3+} with the method of the electron paramagnetic resonance (EPR) absorption of Fe^{3+}. Furthermore, the EPR absorption of Fe^{3+} provides information concerning whether Fe^{3+} is affected by the optical bleaching of the F centers.

The present work presents the results of an effort to make use of iron impurity as the source of cation vacancies in NaF and to investigate possible involvement of the iron impurity in the optical bleaching of the F centers in NaF. The formation and site of Fe^{3+} and Fe^{+} in the lattice of NaF have been investigated in detail by means of the EPR absorption in the previous chapter. The results of the EPR work have indicated that the x-irradiation transforms the iron impurity from Fe^{2+} into Fe^{+} and Fe^{3+}. Each of these two ions has been found to be located at a cation site of the lattice with cubic symmetry. The cation vacancies associated with the conversion of Fe^{2+} to Fe^{3+} and Fe^{+} appear to be free to migrate in the lattice rather than being bound to the immediate neighborhood of the sites of the Fe^{3+} and Fe^{+} ions.

Experimental Procedure and Results

Crystals of NaF with and without iron impurity were obtained from the Harshaw Chemical Co., Cleveland, Ohio. Samples without iron impurity were also obtained from Optovac, North Brookfield, Massachusetts. Samples about 4mm x 4mm x 14mm in dimensions were cut with the [110] axis parallel to the longest dimension of each sample. The samples were exposed to x-rays from a Molybdenum target tube operated at 50 Kv and 20 ma for periods of up to 90 hours at room temperature. The irradiated samples were used for both EPR and optical measurements. The optical

measurements were made at room temperature, with a Bausch and Lomb Spectronic 505 recording spectrophotometer. As mentioned in chapter III, in order to facilitate the optical bleaching experiments, the sample compartment of the spectrophotometer has been modified as illustrated schematically in Fig. 7. The bleaching light is a beam of width 20 mμ, whose central wavelength is equal to 355 mμ. For the purpose of distinction, all samples which exhibit an EPR signal due to Fe^{3+} will be called Type I samples, and all others will be called Type II samples.

Colorability

The F center growth of both Type I and Type II samples under x-irradiation has been investigated by treating both types of samples exactly in the same manner. Two typical growth curves are given in Fig. 18, where the intensity of the F-band, which is a measure of the concentration of the F center, is plotted as a function of x-irradiation time. To obtain the growth curves, the samples were removed from the x-ray unit at several points in time to measure the F-band absorption, and then they were returned for further irradiation without exposure to room light. It has been observed that the Type II samples are always colored more readily than the Type I samples in the early stage of coloration. After extended periods (approximately 60 hours or longer) of x-irradiation, however, the F center concentrations of both types of samples were approximately equal. These results are rather interesting when compared with recent results of similar studies of the F center formation in NaCl crystals doped with Ca^{2+} or Cd^{2+}, which were x-irradiated near room temperature.[46] The Ca^{2+} impurity appeared to enhance the F center production, while the Cd^{2+} impurity apparently had no effect.

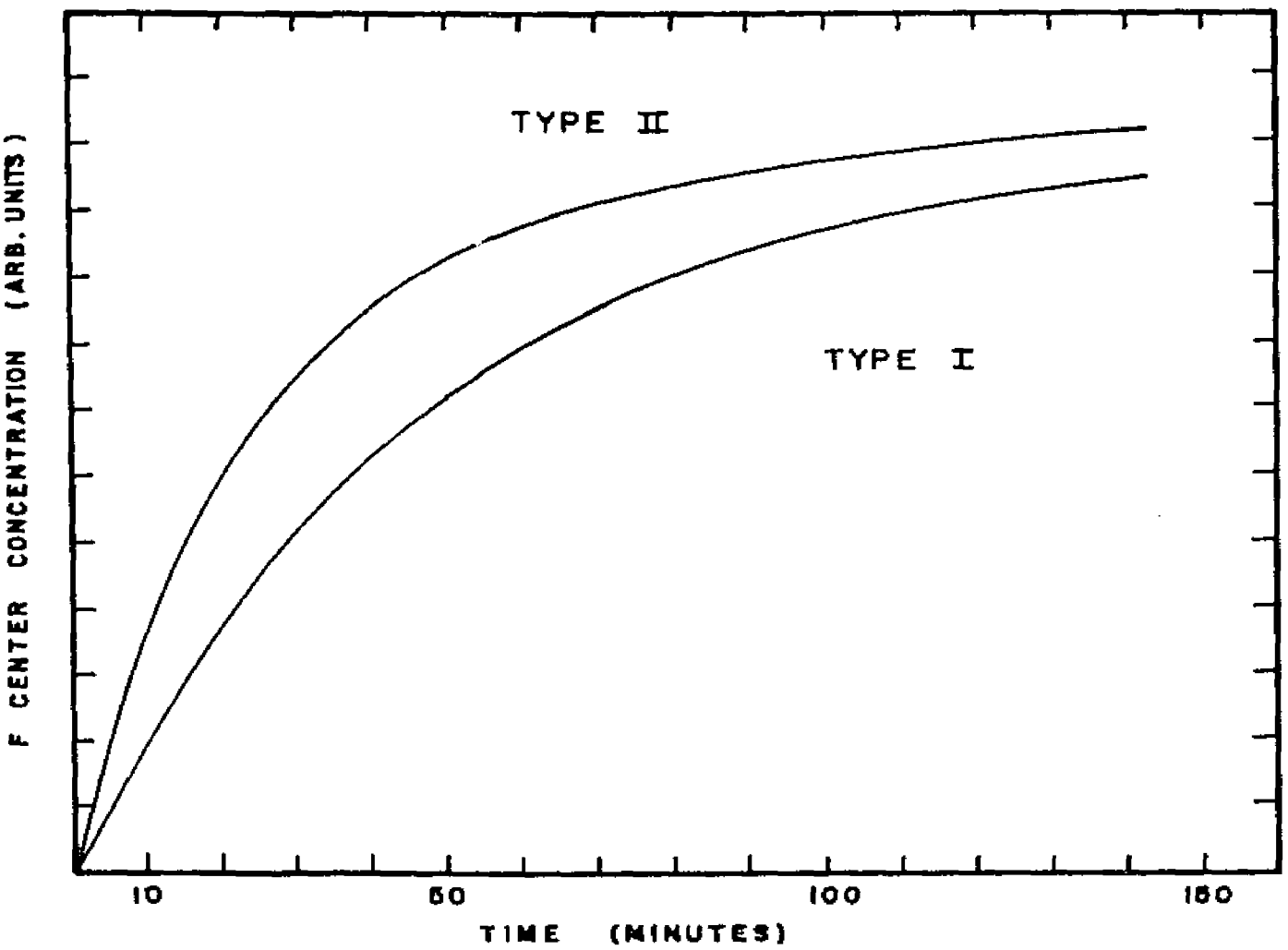

Fig. 18. Typical x-ray colorability curves for F centers in Type I and Type II samples at room temperature.

Optical Bleaching Efficiency

Samples of both types, x-irradiated for the same interval of time (90 hours), were subsequently optically bleached with F-light at room temperature. As mentioned in Section I, the optical bleaching affects both the F-band and the M-band. In Fig. 19, the observed variation of the F and M bands with the controlled bleaching time is illustrated by the two curves labelled F_I and M_I for a Type I sample, and by the other two curves labelled F_{II} and M_{II} for a Type II sample. The bleaching was interrupted at several points in time to measure the optical absorption spectrum of the samples. The major difference is that the changes in Type II samples occur only after much longer periods of time than the corresponding changes in Type I samples. In other words, the bleaching process is consistently more efficient in the Type I samples. The Type II sample used to obtain the bleaching curves in Fig. 19 showed the poorest bleaching efficiency of all the Type II samples measured. The difference in the bleaching efficiency between the two types of samples has been observed to become more noticeable as the period of x-irradiation is increased.

The EPR signals due to Fe^{3+} and Fe^{+} in Type I samples remain unchanged both in intensity and structure during and after optical bleaching.

Aging Effects

If the bleaching light is turned off at some time $t = t_A$, and the sample is allowed to remain in the dark near room temperature for a certain time period Δ, three major effects due to the interruption of bleaching are observed in a subsequent bleaching starting from

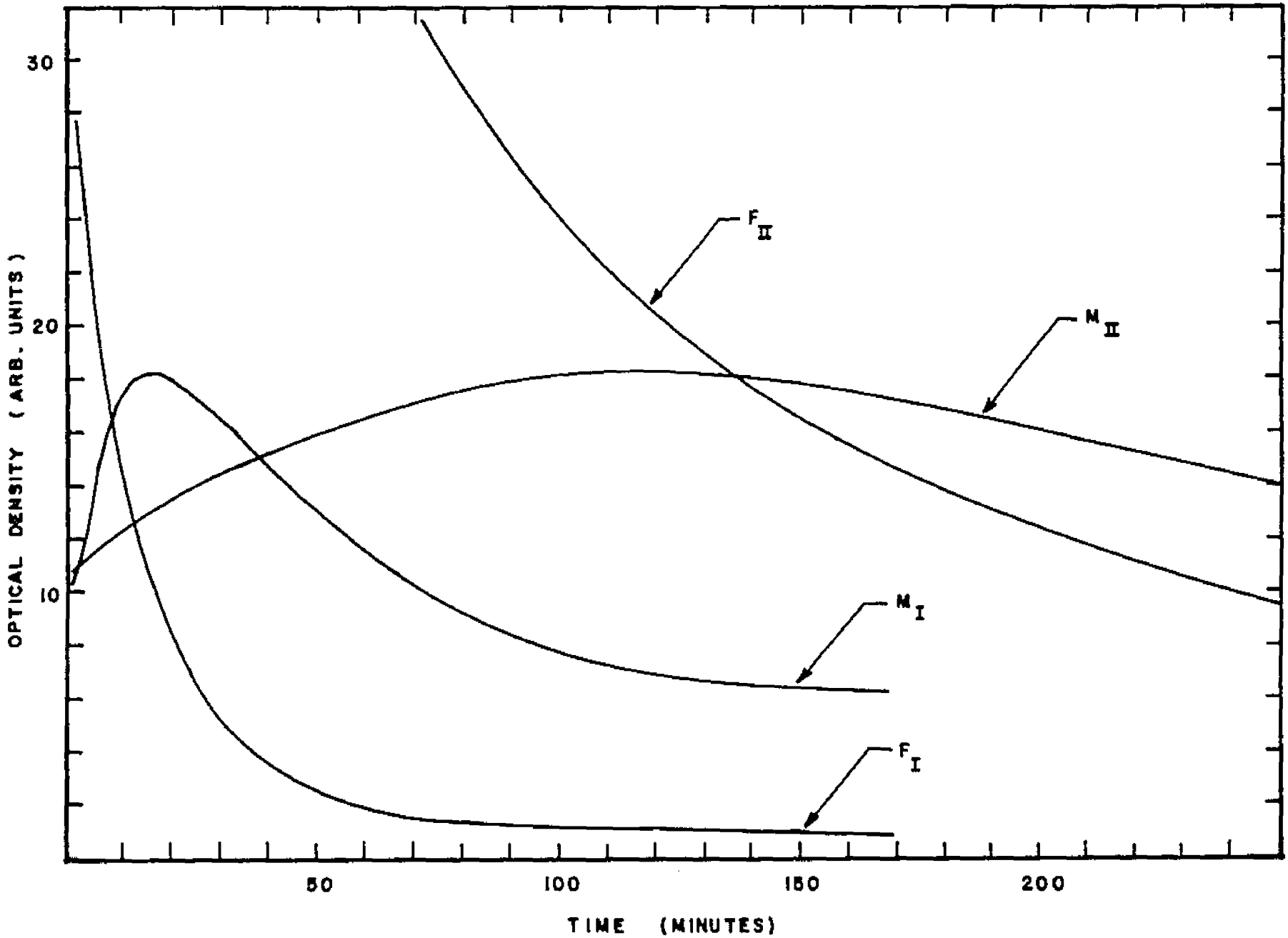

Fig. 19. Typical optical bleaching curves for the F and M centers in Type I (F_I and M_I) and Type II (F_{II} and M_{II}) samples.

$t = t_A + \Delta$. First, the concentration n of the color center at $t = t_A + \Delta$ is the same as that at $t = t_A$, but the rate of bleaching, $-dn/dt$, at time $t_A + \Delta$ is substantially larger than that at time t_A. Secondly, for t larger than $t_A + \Delta$, the rate of bleaching and also the concentration of the color center approach rapidly the values that they would have had, if the bleaching had not been interrupted. Third, these effects vary for different choices of t_A and Δ. These "aging" effects are observed for both the F center and the M center.

Figure 20 illustrates the aging effects by means of a typical M-band bleaching curve (optical density of the M-band vs. the net period of bleaching) of a Type I sample. At an arbitrarily picked point A for which $t = t_A$, the F-light is turned off and the sample is kept in the dark for $\Delta = 382$ minutes. In the figure, t_A and $t_A + 382$ minutes coincide with each other, because of the nature of the time axis mentioned above, and n at t_A is found to be the same as that at $t_A + 382$ minutes. When the bleaching is resumed at $t_A + 382$ minutes, n decreases as indicated by the solid curve from point A to point B, at which point the F-light is turned off again. The rate of bleaching at time $t_A + 382$ minutes is found to be approximately nine times larger than that at time t_A (see next section). The dashed curves starting from points A and C represent portions of the bleaching curve which would be expected without the interruption of the original bleaching from t_A to $t_A + 382$ minutes (see next section). In particular, the dashed curve extending from point C is asymptotic to the solid curve from A to B. This seems to indicate that as the resumed bleaching proceeds from $t_A + 382$ minutes, the values of n and $-dn/dt$ rapidly approach the values that they would have had, had there not been the interruption of bleaching at t_A.

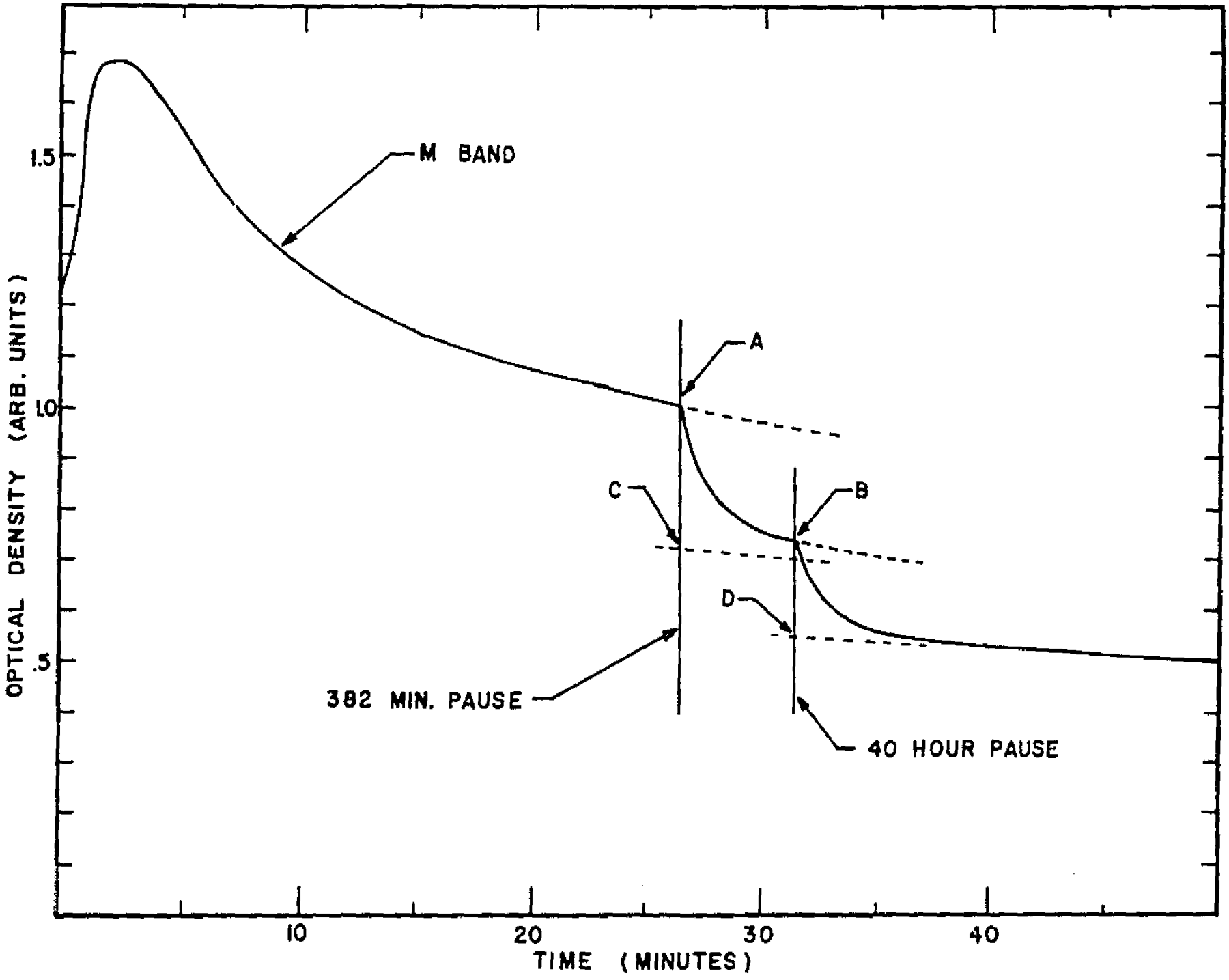

Fig. 20. A typical M center optical bleaching curve of a Type I sample illustrating aging effects after pauses in the F-light optical bleaching at points A and B. The optical density of the M band is plotted as a function

This effect can be observed any number of times. This is illustrated by the portion of the bleaching curve to the right of point B of Fig. 20. The bleaching is terminated at the point B for which $t = t_B$, and the sample is kept in the dark for $\Delta = 40$ hours, and subsequently the bleaching is resumed at $t = t_B + 40$ hours. The solid curve to the right of point B in the figure indicates the subsequent bleaching. The dashed curves extending from points B and D represent the continuation of the solid curve between points A and B, which would be obtained without the interruption of the bleaching from t_B to $t_B + 40$ hours. Again, n at t_B is the same as n at $t_B + 40$ hours, but the rate of bleaching is noticeably enhanced after the second pause in the bleaching. However, the enhanced rate of bleaching is less than that at $t_A + 382$ minutes, indicating the dependence of the aging effects on the time at which the bleaching is terminated, and also on the value of Δ. Furthermore, the dashed curve from point D is asymptotic to the solid curve from point B, illustrating the behavior of n and $-dn/dt$ (see next section).

Three more points of significance should be added here. First, the aging effects are far more noticeable with the Type I samples than with the Type II samples. Second, the aging effects are not observable, when the samples are kept at liquid nitrogen temperature during the period of bleaching interruption. This, the EPR signals of Fe^{3+} and Fe^{+} remain unchanged during the bleaching and aging processes.

The observed results pertaining to the aging effects appear to indicate the following: (i) the aging process does not affect the concentration of the color center, nor does it change the concentration of Fe^{3+} or its cubic crystalline field, (ii) rather, in the process of aging, those defects which are different from the color center and yet

which are actively involved in the bleaching process are redistributed perhaps through thermally activated migration, and (iii) the majority of these defects are caused by the Fe^{3+} ions in the lattice, and they are cation vacancies.

Empirical Analysis of the Aging Effects

The portion of the (solid) bleaching curve of the M-band to the right of the maximum in Fig. 20 can be described very satisfactorily by the following equation

$$n = K/(1 + \tau)^{\lambda} \quad , \tag{27}$$

where n is the concentration of the M centers, τ is the net period of optical bleaching, and K and λ are empirical constants. For the best fit, the values of λ have been found to be 0.26, 0.085, and 0.067 for the solid curves between the maximum and point A, between point A and point B, and to the right of point B in the figure, respectively.

The ratio of the bleaching rate $(-dn/dt)_+$ immediately after a pause to that $(-dn/dt)_-$ just before the pause can be obtained easily from Eq. (27) as follows:

$$(-dn/dt)_+ \; / \; (-dn/dt)_- = (\lambda_+/\lambda_-) \; (1 + t_p) \tag{28}$$

where λ_- and λ_+ are the values of λ before and after the pause respectively and t_p is the net time period of continuous bleaching up to the pause.

The numerical values of λ_+, λ_-, and t_p to be used for points A and B are listed in Table 2. When these values are introduced into Eq. (28), the ratio of bleaching rates is found to be approximately 9.0 at point A and 4.7 at point B.

TABLE 2

THE VALUES OF EMPIRICAL PARAMETERS OF EQ. (28)

	Point A	Point B
λ_+	0.085	0.067
λ_-	0.26	0.085
t_p	26.5 minutes	5 minutes

The observation that n and dn/dt rapidly approach the values they would have had if the bleaching had not been stopped can be stated as a condition on λ used in Eq. (27). To see this consider a general case where the bleaching is started at time t = 0, stopped at $t = t_1$ and resumed at $t = t_2$. Then the period of aging is given by $\Delta = t_2 - t_1$ and

$$n = \frac{(n)_o}{(1 + t)^{\lambda_1}} \quad , \quad (t < t_1) \quad , \tag{29}$$

$$n = \frac{K_2}{(1 + t')^{\lambda_2}} \quad , \quad (t > t_2) \quad , \tag{30}$$

where

$$K_2 = n\ (t_1) = \frac{(n)_o}{(1 + t_1)^{\lambda_1}} \quad ,$$

and $t' = t - t_2$. In order that n approaches but never becomes less than the value it would have had if the bleaching had been continuous,

$$\frac{K_2}{(1 + t')^{\lambda_2}} - \frac{(n)_o}{(1 + t)^{\lambda_1}} \geq o \quad , \quad (t > t_2) \quad . \tag{31}$$

This yields the following restriction on the value of λ_2:

$$\lambda_2 \gtrsim \lambda_1 \left\{ 1 - \frac{\ln(t_1)}{\ln(t_2)} \right\} \quad . \tag{32}$$

This condition is always found to be satisfied experimentally. In fact, the empirical values of λ_2 have been found to be very close to the largest value permitted by Eq. (32).

Proposed Mechanism of Optical Bleaching

The experimental results mentioned in the preceding have established reasonably well that the Fe^{3+} and Fe^{+} impurity ions are

responsible for the optical distinction of the Type I samples from the Type II samples. However, the impurity ions do not participate in the bleaching process directly, that is to say, through thermally activated migration in the lattice. Rather, the cation vacancies associated with the impurity ions seem to migrate and influence the bleaching processes.

Therefore, in order for a mechanism to be responsible for the bleaching processes, it must incorporate these cation vacancies in one way or another. In view of the experimental results, the following mechanism is proposed:

$$(1) \quad F + h\nu_F \rightarrow \alpha + e^- \quad , \tag{23}$$

$$(2) \quad \alpha + \tilde{\alpha} \rightarrow (\alpha,\tilde{\alpha}) \quad , \tag{24}$$

$$(3) \quad (\alpha,\tilde{\alpha}) + F \rightarrow M_s \rightarrow F_2^+ + \tilde{\alpha} \quad , \tag{25}$$

$$(4) \quad F_2^+ + e^- \rightarrow M \quad . \tag{26}$$

Step (1) is the same as the first step of the existing mechanisms mentioned in Section I. In step (2) the α center couples with one of the cation vacancies ($\tilde{\alpha}$) due to the iron impurity, thereby forming a cation-anion vacancy pair $(\alpha,\tilde{\alpha})$. In step (3) the migrating vacancy pair $(\alpha,\tilde{\alpha})$ encounters an F center and forms an M_s center, which corresponds to the model of the M center originally proposed by Seitz.[1] This particular step was previously suggested by Seitz for the formation of the M center. However, the M_s center has never been detected, and it is probably unstable. Therefore, the step (3) continues by the disintegration of the M_s center into an F_2^+ center and an $\tilde{\alpha}$ center. Finally (step (4)), the F_2^+ center captures an electron to form an M center. The α, $\tilde{\alpha}$, $(\alpha,\tilde{\alpha})$ and M_s centers are illustrated in Fig. 21. A possible mode of the M_s center decay is illustrated in Fig. 22. As illustrated, the ions

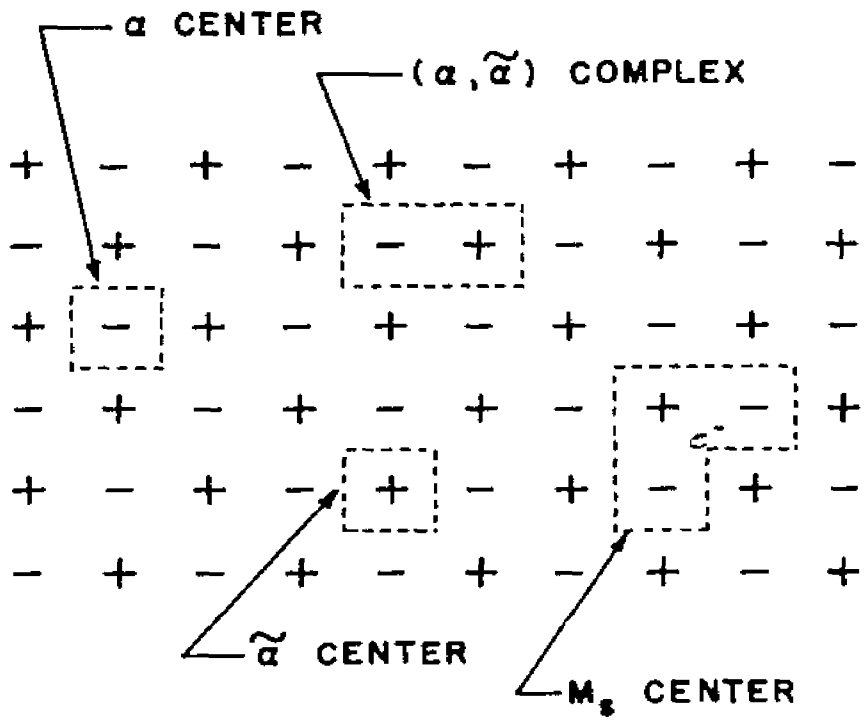

Fig. 21. Schematic diagram illustrating the models of an anion vacancy (α), a cation vacancy (α̃), a vacancy pair (α,α̃), and the Seitz model of an M center (M_S). e^- indicates a trapped electron.

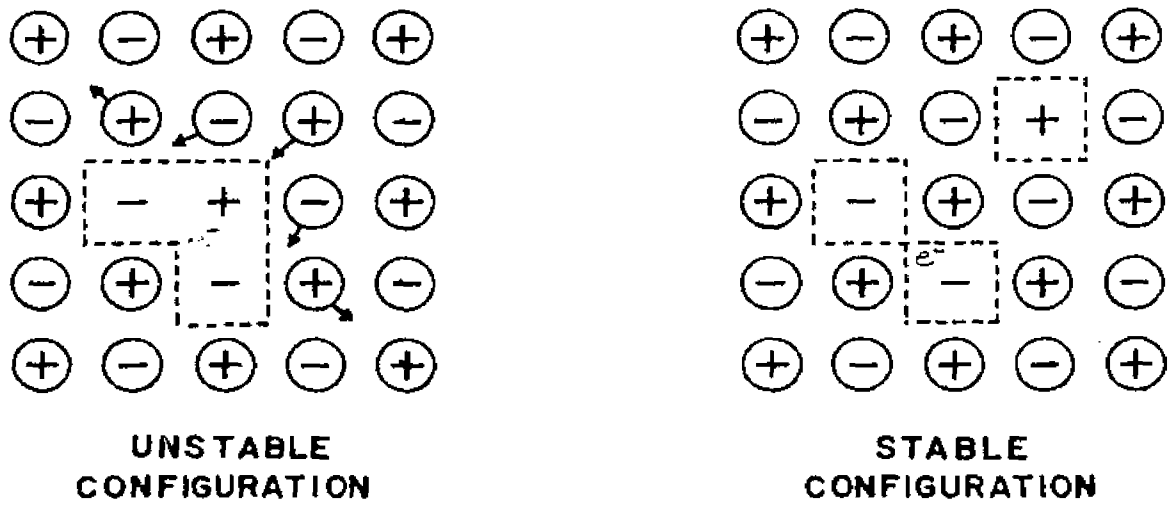

Fig. 22. A probable mode of decay of the M_S center into an M center and an $\tilde{\alpha}$ center. e^- represents a trapped electron. The arrows in the left hand diagram indicate the probable motion of lattice ions.

surrounding the M_s center might conceivably move as indicated by the arrows and allow the center to decay.

A few interesting features of the proposed mechanism seem to deserve comments. First, the cation vacancy involved in the steps (2) and (3) is one and the same cation vacancy, which thus acts like a catalyst. Second, the vacancy pair is expected to be more mobile than isolated vacancies.[1,47] This increased mobility of the vacancy pair should contribute to a corresponding increase in the "encounter" probability of the vacancy pair with an F center. Consequently, the sequence of steps (2) and (3) will definitely increase the efficiency of the optical processes as compared with other mechanisms which depend solely on isolated vacancies. Third, the rate of formation of the M_s centers, and hence the M centers, is proportional to the concentration of the vacancy pairs $(\alpha,\tilde{\alpha})$. But the rate of formation of $(\alpha,\tilde{\alpha})$ is proportional to the concentration of the $\tilde{\alpha}$ centers. Hence, if the concentration of the $\tilde{\alpha}$ centers is large enough, the proposed mechanism will be a dominant one for the formation of the M centers because of the larger mobility of the $(\alpha,\tilde{\alpha})$ centers over the isolated α, and $\tilde{\alpha}$ centers (see the second comment above). If the concentration of the $\tilde{\alpha}$ centers is neglibily small, the dominant mechanism would be one of the mechanisms discussed earlier (see Intro.), since these mechanisms are expected to be effective concurrently with the mechanism discussed above.

There is no doubt that the proposed mechanism is a very simple one in nature, particularly in view of the fact that there are always many other impurities present in commercial samples of NaF and other alkali halides. However, it is interesting, and significant as well, to see how consistently the observed results may be explained in terms of the proposed

mechanism of such a simple nature. This topic will be taken up in the next section.

Discussion of the Experimental Results

The proposed mechanism is based on the availability of excess cation vacancies due to the iron impurity and their participation in the formation of cation-anion vacancy pairs. The observed distinction between the two types of the samples seems to be consistently explained in terms of the excess cation vacancies due to the iron impurity and the proposed mechanism as summarized below.

Colorability

The observed lower efficiency in the colorability of the Type I samples relative to the Type II samples can be explained in terms of the α centers which are to be produced in the process of x-ray conversion of Fe^{2+} to Fe^{3+} and Fe^{+}. Because of the charge neutrality, each Fe^{2+} is accompanied with a charge compensating $\tilde{\alpha}$ center. The EPR absorption of Fe^{2+} is paramagnetic and also its concentration ($\sim$ 8 ppm) is more than enough to yield an observable EPR signal. This is probably due to the α center which is fairly tightly bound to the site of the Fe^{2+} ion. This α center, however, may be made to migrate,[29] when Fe^{2+} is transformed into Fe^{+}. This indicates a physical separation of the $\tilde{\alpha}$ center from the iron impurity site. Furthermore, the conversion of Fe^{2+} to Fe^{3+} contributes additionally two $\tilde{\alpha}$ centers per Fe^{3+} formed. Therefore, the Type I samples subjected to the x-irradiation may contain more $\tilde{\alpha}$ centers than the similarly treated Type II samples. During x-irradiation these excess α centers combine with some of the α centers produced by the x-irradiation. These vacancy pairs migrate and enhance the

recombination of vacancies and interstitials during x-irradiation. Therefore, the number of α centers available for the formation of the F centers is definitely less in the Type I samples than in the Type II samples. In other words, the Type I samples are less easily colored than the Type II samples.

Bleaching Efficiency

The existence of excess ã centers due to the x-ray conversion of the iron impurity mentioned in the preceding can activate the steps (2) and (3) of the proposed mechanism in the previous section, thus contributing to the observed enhancement of the bleaching efficiency of the Type I samples over the Type II samples, for which Delbecq's mechanism is probably dominant.

Since the ã centers are produced gradually under x-irradiation, the difference in optical bleaching efficiencies between Type I and Type II samples would be expected to become more noticeable for a longer x-irradiation time. This actually has been observed in the present experiment.

Aging Effects

Before bleaching commences, the excess ã centers and F centers are presumably distributed randomly through the lattice. Some F centers will have an ã center nearby and others will not. During bleaching, (α,ã) centers have a better chance of being formed, if an F center, which is the source of an α center during bleaching, and an ã center are close to one another. Once formed, the (α,ã) center, with its relatively high mobility, can migrate to form an M center according to the steps (2), (3), and (4). As the bleaching proceeds, the average distance between

an F center and an $\tilde{\alpha}$ center tends to increase and consequently the probability of formation of $(\alpha,\tilde{\alpha})$ centers tends to decrease. However, when the sample is allowed to remain in the dark at room temperature, the $\tilde{\alpha}$ centers, which are still able to migrate, may redistribute themselves. In doing so many F centers will acquire an $\tilde{\alpha}$ center in their immediate neighborhood. Thus, when bleaching starts again, the bleaching rate will be higher than when the bleaching was stopped. This accounts for the aging effects.

Conclusion

Effects of iron impurity on the x-ray colorability and the subsequent optical bleaching of NaF have been investigated near room temperature. EPR and optical absorption measurements have been made on NaF samples with (Type I) and without (Type II) iron impurity. The results have indicated that the colorability of Type I samples is poorer than that of Type II samples, but the efficiency of the optical bleaching of Type I samples is significantly larger than that of the Type II samples.

The optical bleaching has been found to exhibit "aging" effects. The aging effects are far more noticeable with Type I samples than with Type II samples.

In order to account for the observed distinction between the two types of samples, an impurity controlled mechanism of optical bleaching is proposed. The mechanism is based on the availability of excess cation vacancies associated with the iron impurity, and their participation in the formation of cation-anion vacancy pairs.

CHAPTER VI

OBSERVATION OF AN UNSTABLE N-BAND IN NaF

In several alkali halides, when optical bleaching is continued for extended periods, optical absorption bands due to N centers (see Chapter II and Fig. 3) appear on the long wavelength side of the F-band. In NaF no prominent N-bands have been observed. In this chapter experimental evidence of an unstable N-band in x-irradiated NaF is presented. A summary of this work has recently been published by this author and Y.W. Kim in the Physics Letters.[48]

In the case of LiF, KCl, KBr, NaCl, and KI, the N-bands have been observed,[2,49-51] and they seem to satisfy an Ivey type relation:[52]

$$\lambda_{max} = 1730\ d^{1.52} \quad \text{for the } N_1\text{-band} \quad , \tag{33}$$

$$\lambda_{max} = 1880\ d^{1.52} \quad \text{for the } N_2\text{-band} \quad , \tag{34}$$

where λ_{max} and d are the wavelength of the absorption maximum of the band and the lattice constant, respectively, both in Angstrom units. The two empirical Ivey relations for the N-bands are illustrated by the two straight lines labelled as N_1 and N_2 in Fig. 23. It should be noted here that the N_1- and N_2-lines in Fig. 23 are drawn without any attention to the experimental point for NaF to be described in this chapter.

The band investigated here (simply band N for convenience) has an absorption maximum at approximately 727 mμ (1.705 ev) and a half width of approximately 0.142 ev, and is unstable at 300°K. It can be produced in single crystals of NaF, with varying degrees of difficulty, depending upon the ingots of Harshaw and Optovac.

The Type I samples, which were referred to in Chapter V as having a

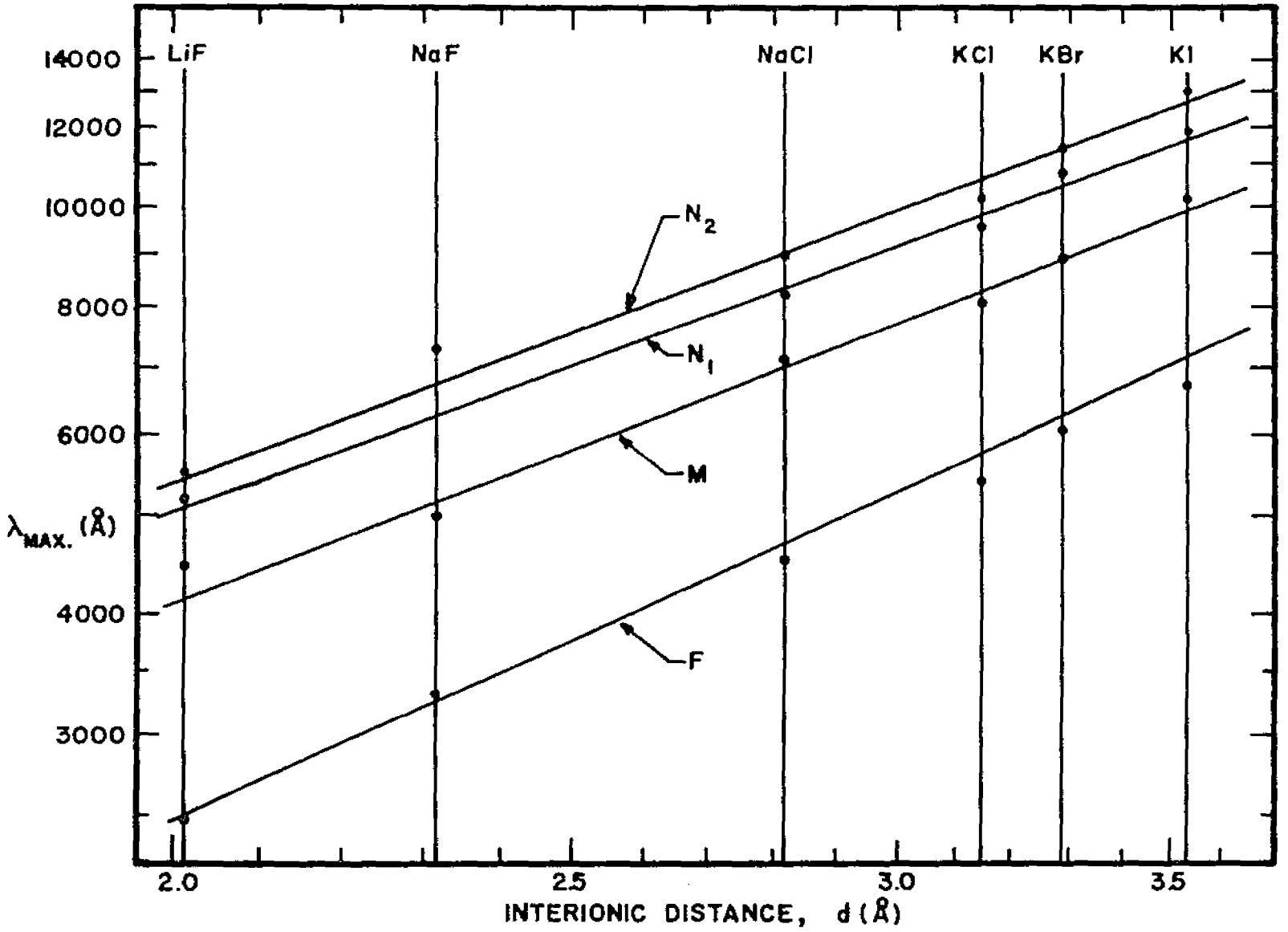

Fig. 23. λ_{max} (dots) of N bands, and also F and M bands, observed in several alkali halides, and Ivey's relations (straight lines) for the bands. The straight lines for the F and M bands are taken from ref. 2: $\lambda_m = 703\ d^{1.84}$ (F band) and $\lambda_{max} = 1400\ d^{1.56}$ (M band). They are included here for comparison.

high bleaching efficiency, also developed the most intense band N. This is not unexpected since band N is unstable and the larger the rate of formation, the larger the maximum intensity of the band N. This may indeed be the reason why this band has not been observed previously in NaF, since the observation depends on a sample with impurities which enhance the bleaching process.

Typically, a sample of NaF obtained from Harshaw is first irradiated for 34 hours by x-rays from a Molybdenum target tube operated at 50 kev and 20 ma. The irradiated sample contains a large concentration of F centers. Subsequently, the F-band centered at 341 mμ is bleached with the F-light filtered from a 150 watt high pressure Hg lamp. This F-bleach leads first to a very rapid growth of the M-band centered at 507 mμ to a maximum intensity, after which the M-band decreases. In the process, the band N continues to grow at a slower rate, and reaches a maximum intensity much later than the M-band. The observed behavior of the F- and M-bands, and the band N during the bleaching is illustrated in Fig. 24. Notice that the bleaching time is on a logarithmic scale since changes are relatively slow in the region where the band N reaches its maximum. If, at the point where the band N is at maximum, the bleaching light is turned off and the sample is allowed to set in the dark, the band N decays exponentially with a time constant τ = 7.8 hours, as illustrated in Fig. 25.

The band N of the present work seems to have the following three major similarities with the known N bands of KCl and other alkali halides: (1) The λ_{max} of the band N is fairly close to that predicted by the Ivey relation for the N_2-band of KCl and other alkali halides (see Fig. 23). Since λ_{max} of the band N is obtained at 300°K, while λ_{max} for the other alkali halides except for LiF in Fig. 23 refers to 77°K, a temperature

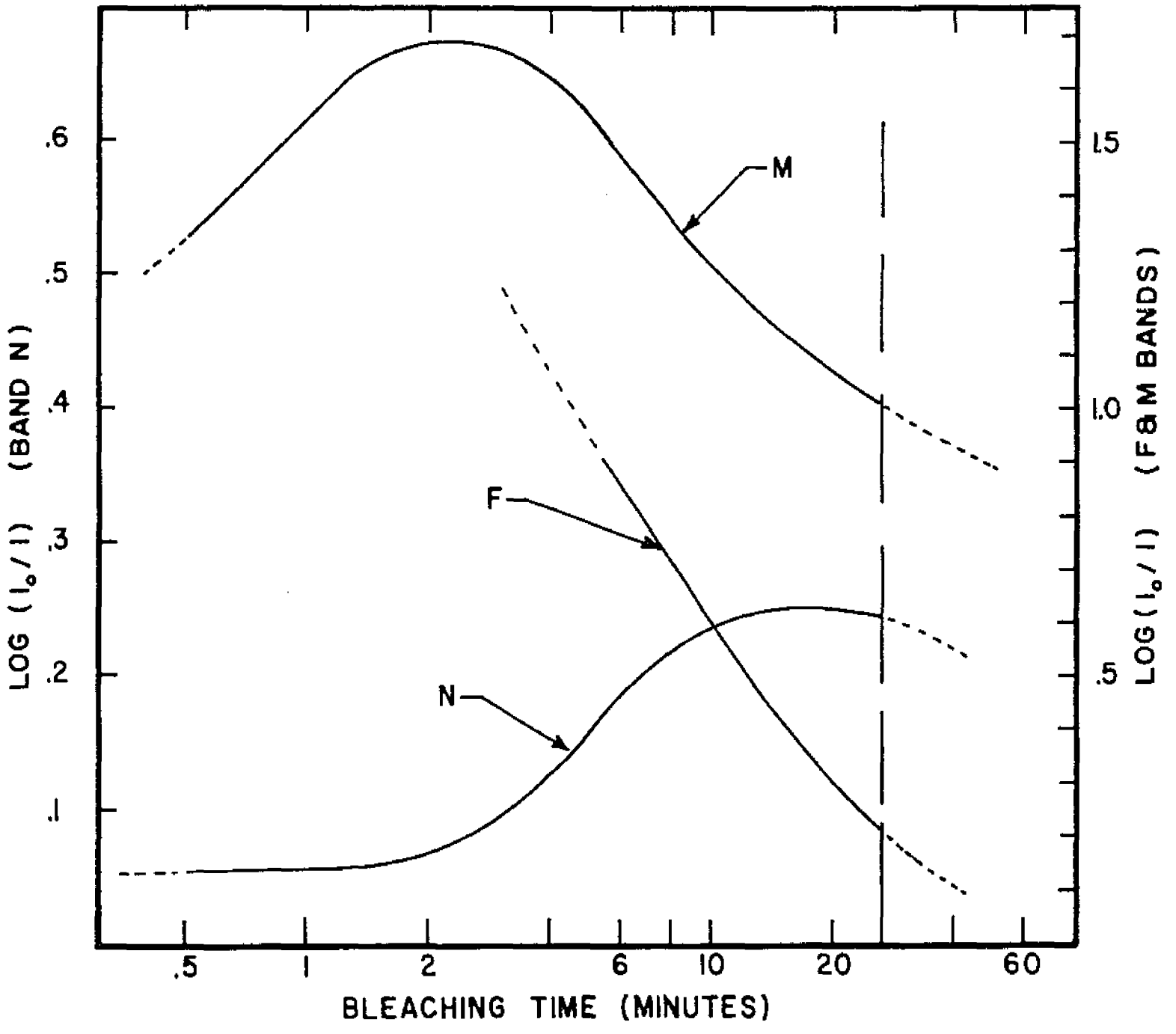

Fig. 24. Behavior of the band N, and the F and M bands during optical bleaching with F-light. Note the different ordinate scales for the F and M bands and the band N.

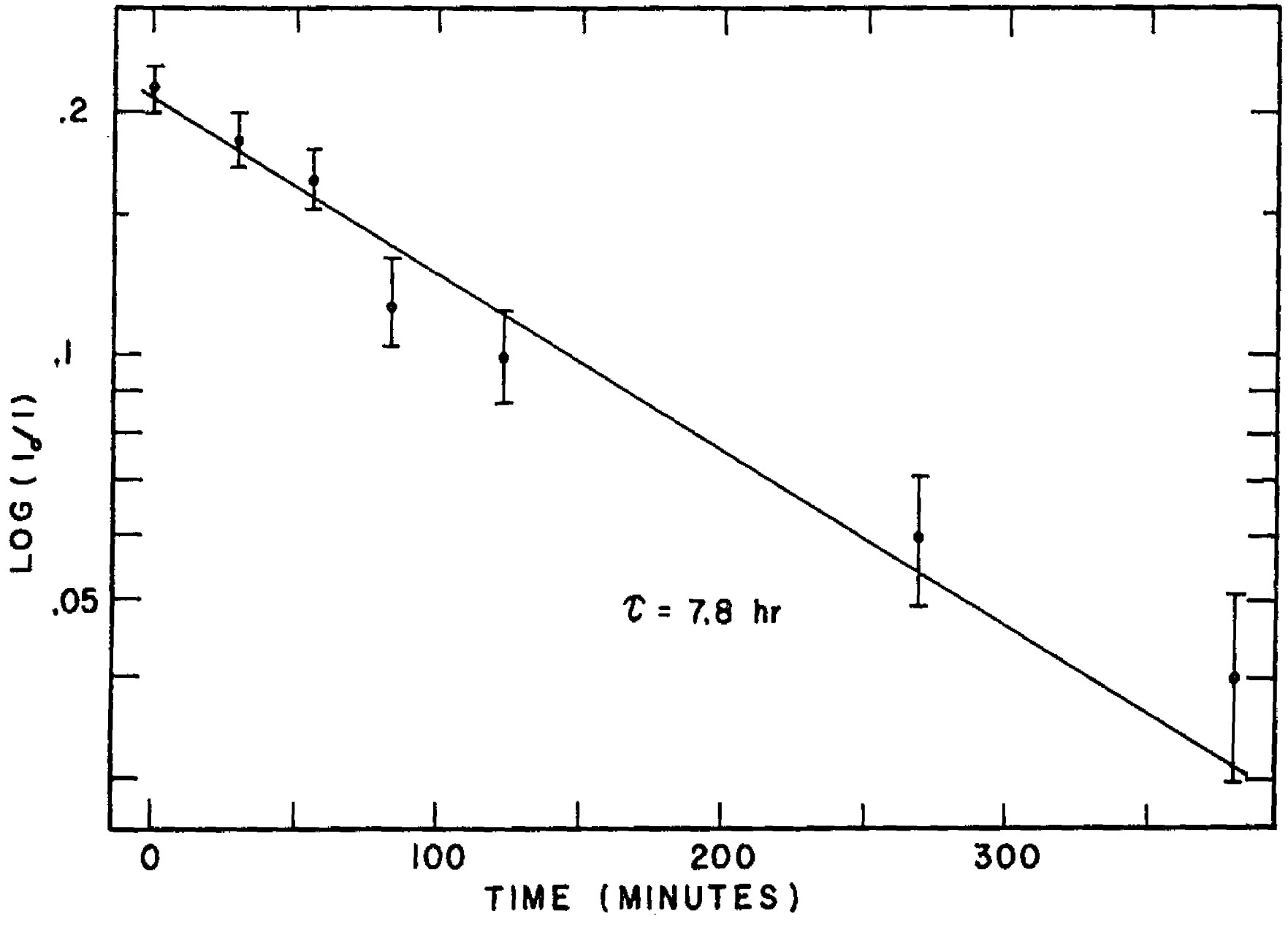

Fig. 25. Exponential decay with time constant 7.8 hours of the band N, when left in the dark.

correction should move λ_{max} of NaF closer to the N_2 line of the Ivey relation by approximately 10 mμ. (2) The formation process of the band N by the F-bleach is similar to that of the N bands in x-irradiated KCl.[53] (3) According to Pierce,[54] certain zero-phonon lines appear in the general region of the N bands of alkali halides. In the case of NaF, four zero-phonon lines have been detected. One of them located at 821.7 mμ corresponds to the long wavelength edge of the band N reported here.

These similarities suggest very strongly that the unstable band N observed in the present work is one of the N bands of NaF, probably the N_2 band.

APPENDIX I

HYPERFINE INTERACTION TERM IN A SPIN HAMILTONIAN

The hyperfine term in the spin Hamiltonian for a paramagnetic ion describes the interaction between the magnetic dipole moment of the paramagnetic ion and all the neighboring nuclear magnetic moments.[55] For simplicity, consider an interaction of the paramagnetic ion with only one nuclear magnetic moment. (For the more general case of many nuclear magnetic moments, it is only necessary to add the interactions due to each of them.) Let

$$\vec{\mu}_s = \text{spin magnetic moment of the paramagnetic ion,}$$
$$= -g\beta\vec{S} \qquad \text{(A-1)}$$
$$\vec{\mu}_n = \text{magnetic moment of the nucleus,}$$
$$= g_N\beta_N\vec{I} \ , \qquad \text{(A-2)}$$

where β , β_N = electronic and nuclear Bohr magnetons, respectively,

g , g_N = electronic and nuclear g-factors, respectively,

$\vec{S}$ = spin of the paramagnetic ion, and

$\vec{I}$ = spin of the interacting nucleus.

Also let $\vec{r}$ be a radius vector in a cartesian coordinate system whose origin coincides with the site of the interacting nucleus..

The Hamiltonian which describes the magnetic effects of this system of a paramagnetic ion and one interacting nuclear magnetic moment can be given by

$$\mathcal{H} = g\beta\vec{S}\cdot\vec{H} - g_N\beta_N\vec{I}\cdot\vec{H} + \mathcal{H}_{H.F.} \qquad \text{(A-3)}$$

The first term is the Zeeman energy of the paramagnetic ion and the second term is the nuclear Zeeman energy. The third term is the

hyperfine interaction term which can be expressed as follows:

$$\mathcal{H}_{H.F.} = \left\{ \frac{-3(\vec{\mu}_N \cdot \vec{r})(\vec{\mu}_S \cdot \vec{r})}{r^5} + \frac{\vec{\mu}_N \cdot \vec{\mu}_S}{r^3} \right\} - \frac{8\pi}{3} \vec{\mu}_N \cdot \vec{\mu}_S \, \delta(\vec{r}) \quad , \tag{A-4}$$

where the first term is the dipole-dipole interaction and the second term is the Fermi contact interaction.

Let ψ be the orbital wave function of the paramagnetic ion. It is now possible to calculate the spin Hamiltonian term for the hyperfine interaction which is given by

$$\mathcal{H}_{S,H.F.} = \int \psi^* \mathcal{H}_{H.F.} \psi \, d\tau \quad , \tag{A-5}$$

where the integration is over spatial coordinates only. Hence, using Eqs. (A-1), (A-2), (A-4), and (A-5),

$$\mathcal{H}_{H.F.} = g g_N \beta \beta_N \left\{ \frac{3(\vec{I} \cdot \vec{r})(\vec{S} \cdot \vec{r})}{r^5} - \frac{\vec{I} \cdot \vec{S}}{r^3} + \frac{8\pi}{3} \vec{I} \cdot \vec{S} \, \delta(\vec{r}) \right\} \quad , \tag{A-6}$$

and

$$\mathcal{H}_{S,H.F.} = g g_N \beta \beta_N \int \left\{ \frac{3(\vec{I} \cdot \vec{r})(\vec{S} \cdot \vec{r})}{r^5} - \frac{\vec{I} \cdot \vec{S}}{r^3} + \frac{8\pi}{3} \vec{I} \cdot \vec{S} \, \delta(\vec{r}) \right\} |\psi(\vec{r})|^2 d\tau \quad . \tag{A-7}$$

Equation (A-7) can be written as

$$\mathcal{H}_{S,H.F.} = \vec{I} \cdot \underline{A} \cdot \vec{S} \quad , \tag{A-8}$$

where $\underline{A}$ is the hyperfine interaction tensor. For convenience $\underline{A}$ is divided into what is called the anisotropic hyperfine tensor $\underline{B}$ and the isotropic hyperfine term δ, as follows:

$$\underline{A} = \underline{B} + \delta \quad , \tag{A-9}$$

The cartesian components of $\underline{B}$ are indicated by $B_{m,n}$ where m, n = 1, 2, or 3; and

$$B_{m,n} = gg_N\beta\beta_N \int \left\{\frac{3x_m x_n}{r^5} - \frac{\delta_{mn}}{r^3}\right\} |\psi(\vec{r})|^2 d\tau \quad , \qquad (A\text{-}10)$$

$$\delta = \frac{8\pi}{3} gg_N\beta\beta_N \int \delta(\vec{r}) \; |\psi(\vec{r})|^2 d\tau \quad .$$

In these expressions, x_i refers to a component of the vector $\vec{r}$. At this point it can be shown that the tensor $\underline{B}$ is traceless.

$$\text{Trace } \underline{B} = \sum_{i=1}^{3} B_{ii} = gg_N\beta\beta_N \int \left\{\frac{3(x_1^2+x_2^2+x_3^2)}{r^5} - \frac{3}{r^3}\right\} |\psi(\vec{r})|^2 d\tau = 0 \quad . \qquad (A\text{-}11)$$

In order to evaluate the components of $\underline{A}$, assume that the wave function of the paramagnetic ion $\psi(\vec{r})$ has axial symmetry about the z-axis.* The same results can be derived if the z-axis is an n-fold axis of symmetry where $n \geq 3$.[3] With this assumption,

$$B_{xy} = 3gg_N\beta\beta_N \left\{\int_0^\infty \int_0^\pi \frac{\sin^2\xi}{r^3} |\psi|^2 r^2 \sin\xi d\tau d\xi\right\} \left\{\int_0^{2\pi} \sin\eta\cos\eta d\eta\right\} = 0 \qquad (A\text{-}12)$$

where $x_1 = r\sin\xi\cos\eta$, $x_2 = r\sin\xi\sin\eta$, and $x_3 = r\cos\xi$; and ξ and η are the polar angles of $\vec{r}$ using the line joining the paramagnetic ion and the interacting nucleus as the polar axis (see Fig. 26). Likewise

$$B_{xz} = B_{yz} = B_{yx} = B_{zx} = B_{zy} = 0 \qquad (A\text{-}13)$$

In a similar manner,

---

* In what follows the line joining the paramagnetic ion and the nuclear site will be referred to as the z-axis.

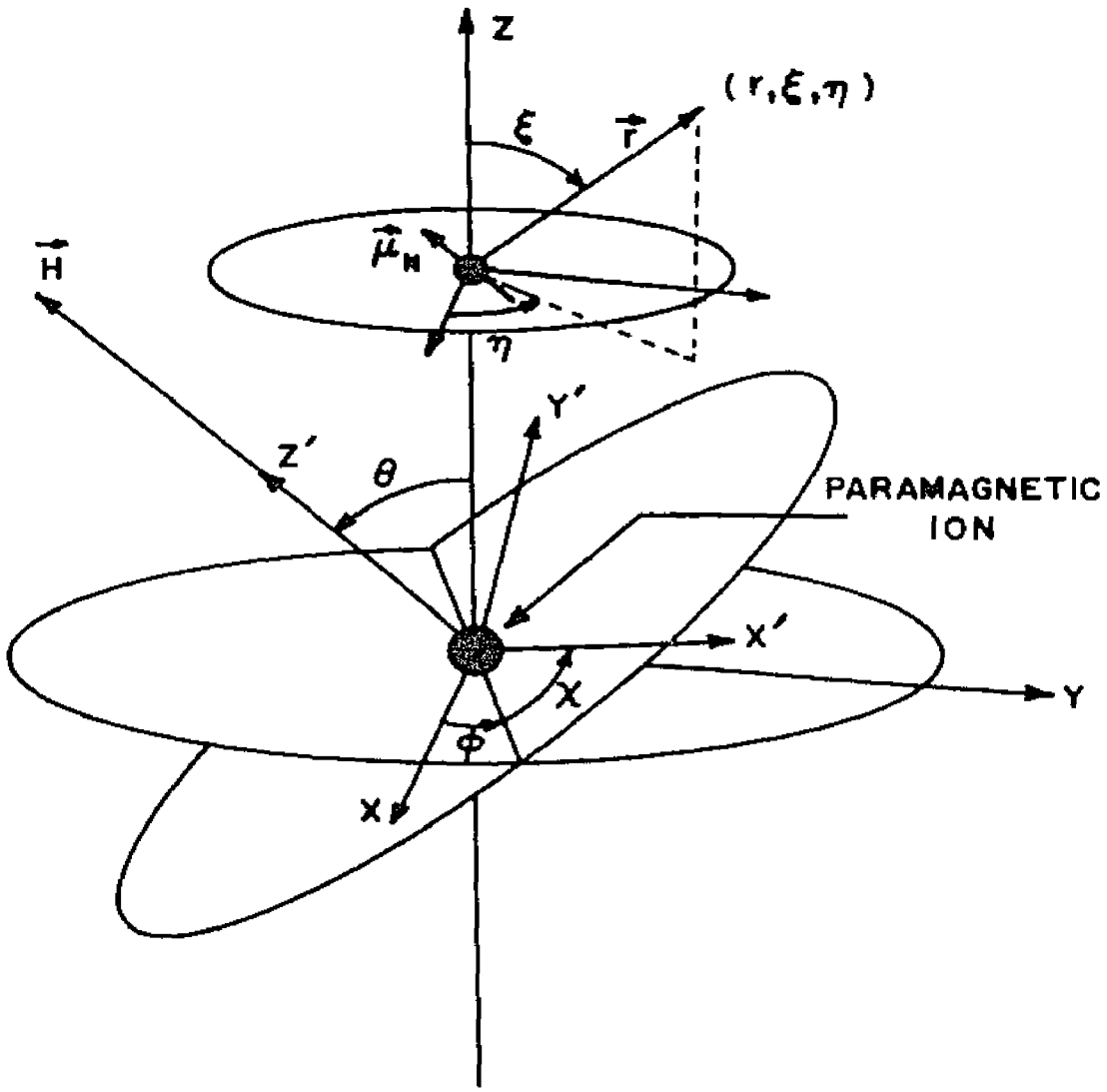

Fig. 26. Coordinate systems used to find the hyperfine interaction between a paramagnetic ion and a single nuclear magnetic moment. $\vec{H}$ is directed along the z' axis and the nuclear magnetic moment is located on the z axis.

$$B_{xx} = gg_N\beta\beta_N \int_0^\infty\int_0^\pi\int_0^{2\pi} \frac{3\sin^2\xi\cos^2\eta-1}{r^3} |\psi|^2 \, r^2\sin\xi dr d\xi d\eta$$

$$= gg_N\beta\beta_N \int_0^\infty\int_0^\pi \frac{3\pi\sin^2\xi-2\pi}{r^3} |\psi|^2 \, r^2\sin\xi dr d\xi$$

$$= gg_N\beta\beta_N \int_0^\infty\int_0^\pi \frac{3-3\cos^2\xi-2}{r^3}\pi |\psi|^2 \, r^2\sin\xi dr d\xi$$

$$= -gg_N\beta\beta_N \, \pi \int_0^\infty\int_0^\pi \frac{3\cos^2\xi-1}{r^3} |\psi|^2 \, r^2\sin\xi dr d\xi$$

$$= -\gamma \quad ; \tag{A-14}$$

also

$$B_{yy} = -\gamma \tag{A-15}$$

and

$$B_{zz} = gg_N\beta\beta_N \int_0^\infty\int_0^\pi\int_0^{2\pi} \frac{3\cos^2\xi-1}{r^3} |\psi|^2 \, r^2\sin\xi dr d\xi d\eta = 2\gamma \quad . \tag{A-16}$$

Thus

$$\underline{A} = \underline{B} + \delta = \begin{pmatrix} \delta-\gamma & 0 & 0 \\ 0 & \delta-\gamma & 0 \\ 0 & 0 & \delta+2\gamma \end{pmatrix} \tag{A-17}$$

referred to the (x,y,z) system (see Fig. 26) and

$$\mathcal{H}_{S,H.F.} = I_z S_z(\delta+2\gamma) + (\delta-\gamma)(I_x S_x + I_y S_y) \tag{A-18}$$

Consider the paramagnetic ion and the interacting nucleus to be in a large external magnetic field $\vec{H}$. The electronic Zeeman term is then much larger than the hyperfine interaction term. In this case $\vec{S}$ is quantized along the magnetic field direction. However, the interacting nucleus sees not only the external magnetic field, but the dipole field due to the magnetic moment of the paramagnetic ion. The nuclear magnetic moment will be quantized along the direction of the external magnetic field in two cases: (1) If the nuclear Zeeman term $(-g_N\beta_N\vec{H}\cdot\vec{I})$ is much

larger than the hyperfine interaction and (2) If the isotropic part of the hyperfine interaction (measured by δ) is much larger than both the nuclear Zeeman term and the anisotropic hyperfine interaction (measured by $\underline{B}$). In the second case the dominant term as far as the nucleus is concerned, is the isotropic hyperfine term which has the form $\delta\vec{S}\cdot\vec{I}$. Since in this case $\vec{S}$ is quantized along the direction of $\vec{H}$, $\vec{I}$ will be quantized along the same direction. The two cases mentioned above describe most of the situations which normally occur. Hence, in what follows, it will be assumed that $\vec{I}$ is quantized along the direction of $\vec{H}$ just as is $\vec{S}$.

Define an (x,y,z) coordinate system with its origin at the site of the paramagnetic ion and the interacting nucleus lying on the z axis as shown in Fig. 26. Also define an (x',y',z') system which has Eulerian angles (θ,ϕ,χ) relative to the (x,y,z) system. Let the magnetic field $\vec{H}$ be directed along the z' axis. Then $\vec{S}$ and $\vec{I}$ are quantized along the z' axis and the matrix elements of $\vec{I}$ and $\vec{S}$ are known in the (x',y',z') system (i.e. $\langle I_{x'}\rangle = \langle I_{y'}\rangle = \langle S_{x'}\rangle = \langle S_{y'}\rangle = 0$). However, measurements are made with respect to the (x,y,z) system. Therefore, Eq. (A-18) must be transformed to the (x,y,z) system. Referring to Fig. 26:

$$\begin{aligned} I_z &= I_{z'}\cos\theta + (\text{terms in } I_{x'}, I_{y'}) \\ I_x &= I_{z'}\sin\theta\cos\psi + (\text{terms in } I_{x'}, I_{y'}) \\ I_y &= I_{z'}\sin\theta\sin\psi + (\text{terms in } I_{x'}, I_{y'}) \end{aligned} \tag{A-19}$$

and

$$\begin{aligned} S_z &= S_{z'}\cos\theta + (\text{terms in } S_{x'}, S_{y'}) \\ S_x &= S_{z'}\sin\theta\cos\psi + (\text{terms in } S_{x'}, S_{y'}) \\ S_y &= S_{z'}\sin\theta\sin\psi + (\text{terms in } S_{x'}, S_{y'}) \end{aligned} \tag{A-20}$$

Using Eqs. (A-18), (A-19), and (A-20),

$$\begin{aligned}\mathcal{H}_{S,H.F.} &= I_z, S_z, (\delta+2\gamma)\cos^2\theta \\ &+ (\delta-\gamma)(\sin^2\theta\cos^2\phi + \sin^2\theta\sin^2\phi)\, S_z, I_z, \\ &= I_z, S_z, \{\delta+\gamma(3\cos^2\theta-1)\} \qquad \text{(A-21)}\end{aligned}$$

Equation (A-21) gives the spin Hamiltonian term for the hyperfine interaction for the case of $\vec{S}$ and $\vec{I}$ both being quantized along $\vec{H}$. δ and γ are known as the isotropic and anisotropic hyperfine coupling constants, respectively.

APPENDIX II

SPIN HAMILTONIAN FOR $S_{5/2}$ - STATE IONS IN A CUBIC CRYSTALLINE FIELD

Electron paramagnetism occurs whenever an atomic system has a resultant angular momentum of electronic origin. One way this can happen is for an ion to have a partially filled inner shell. This happens in the case of the transition elements. For example, the iron group elements ($_{21}Sc \rightarrow {}_{29}Cu$) have an electronic configuration consisting of a complete core, which is the same as the argon configuration, a partially filled 3d shell, and two 4s electrons (except copper which has only one 4s electron). According to Hund's rule,[56] whenever an electronic shell of an ion is half filled, the ground state of the ion is an S-state. There are three commonly occuring ions in the iron group for which this happens: Cr^{+}, Mn^{2+}, and Fe^{3+}. Each of these ions has a $^6S_{5/2}$ ground state due to a $(Ar)(3d)^5$ electronic configuration. If one of these paramagnetic ions is placed in a solid, it will see a crystalline field due to its neighboring ions in the solid. In general, the crystalline field destroys some of the orbital degeneracy of the ground state. Also, further splitting is caused by spin-orbit coupling ($\lambda \vec{L} \cdot \vec{S}$), and there are magnetic interactions between the magnetic moment of the paramagnetic ion and neighboring magnetic moments in the lattice (electronic and nuclear).

In what follows consider only the specific example of an $^6S_{5/2}$ ion located substitutionally at a cation site in a cubic crystal. To first order, there is no splitting of the ground state since it is an orbital singlet. Higher order perturbation theory does give a splitting of the six magnetic sub-levels as is observed experimentally. The theory

of the S-state ion splitting is discussed in detail in references 11, 14, and 15.

The Spin Hamiltonian used to describe the $^6S_{5/2}$ ion will have the following terms: (1) the Zeeman interaction terms, (2) the hyperfine interaction, and (3) the fine structure term. The electronic Zeeman term is given by

$$g\beta\ \vec{S}\cdot\vec{H} \qquad \text{(A-22)}$$

where g = electronic g factor,

β = Bohr magneton, and

$\vec{H}$ = external magnetic field.

The hyperfine interaction is described in detail in Appendix I. The fine structure term incorporates the combined effects of the crystalline field, spin-orbit coupling, and the spin-spin interaction between the electrons of the paramagnetic ion. Hence, among other things the fine structure term will depend on the crystalline field and $\vec{S}$. This term will be dealt with in detail in the remainder of this appendix.

The general form of the fine structure term and how it depends on $\vec{S}$ can be found by symmetry considerations. When a paramagnetic ion is placed in a solid its wavefunction will be determined by the crystalline field. Therefore, in the absence of an external magnetic field the spin Hamiltonian which describes the paramagnetic ion will have the symmetry of the crystalline field. Consider the $^6S_{5/2}$ ion to be situated at a cubic site, which is taken as the origin of an (x,y,z) coordinate system as shown in Fig. 27. The x,y, and z axes lie along the [100], [010], and [001] crystalline directions, respectively; and they are three mutually orthogonal and equivalent axes. This implies that the <u>fine structure term</u> in the spin Hamiltonian must remain unchanged by any permutation of (x,y,z).

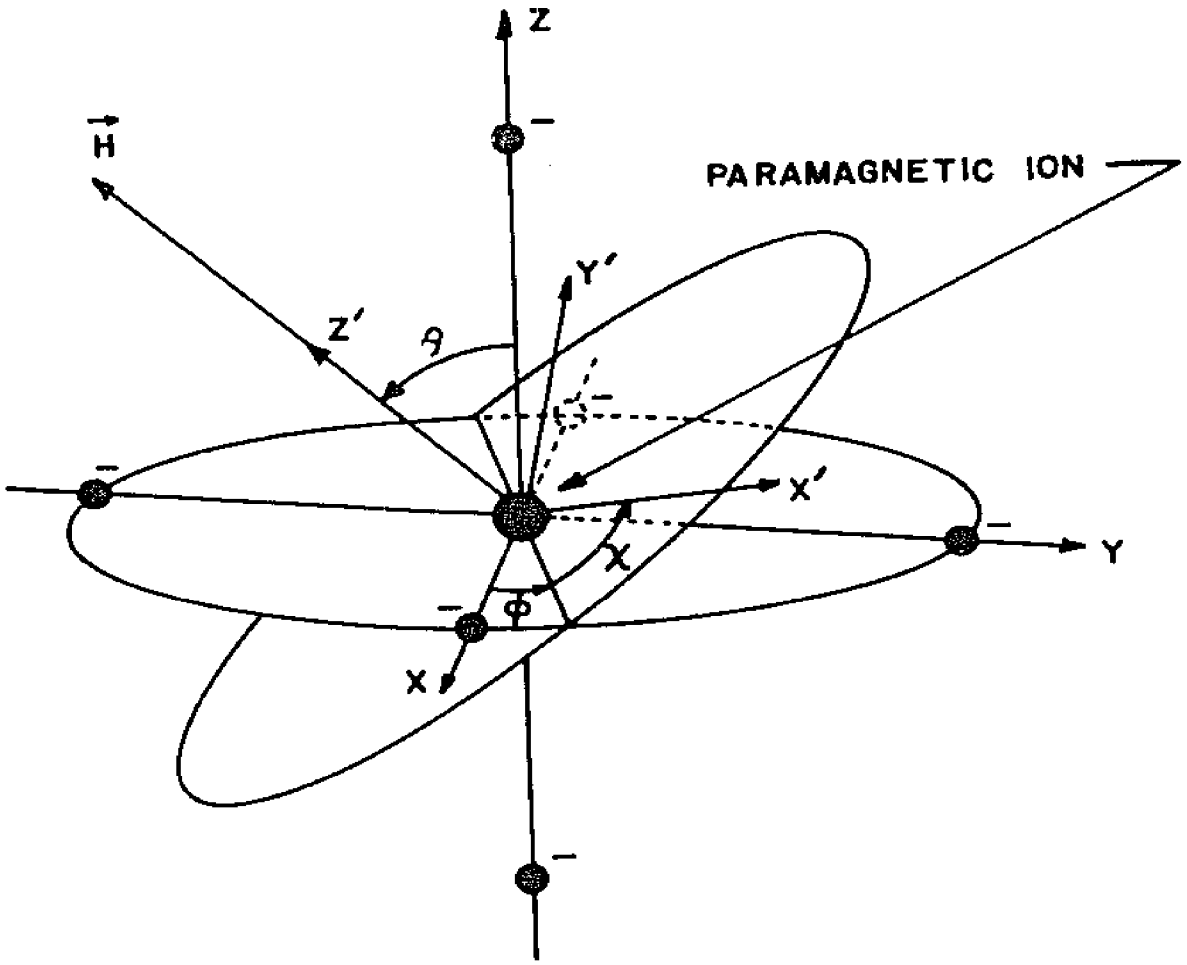

Fig. 27. Coordinate system of the cubic lattice (x, y, z) and a primed coordinate system in which $\vec{H}$ is along the z' axis.

Also, if for example S_x^2 appears in the spin Hamiltonian, then S_y^2 and S_z^2 must appear with the same coefficient, i.e. $c(S_x^2 + S_y^2 + S_z^2)$. However, since $S_x^2 + S_y^2 + S_z^2 = S(S+1)$ is a constant, it can be neglected in the determination of the magnetic energy level structure. To find the most general spin dependence of the fine structure term all possible combinations of the spin components must be considered. Terms such as S_xS_y can be expressed as functions of S_x^2, S_y^2, and S_z^2 and therefore they can also be neglected. Other possibilities are terms like $S_x^2S_y^2$ and S_x^4. Note that

$$[S(S+1)]^2 = (S_x^2 + S_y^2 + S_z^2)^2 = S_x^4 + S_y^4 + S_z^4 + (S_x^2S_y^2 + S_y^2S_z^2 + S_z^2S_x^2 + S_y^2S_x^2 + S_z^2S_y^2 + S_x^2S_z^2) \quad . \tag{A-23}$$

Hence terms such as $S_x^2S_y^2$ can be replaced by some multiple of $(S_x^4 + S_y^4 + S_z^4)$ plus a constant. For $S = 5/2$, it can be shown that even power terms of sixth and higher orders reduce to expressions in S_x^4, S_y^4, and S_z^4 and constants.[57] Odd power terms of the spin components do not appear because of symmetry considerations. For example a rotation of 90° about the z axis leaves the crystalline field unchanged. This means that a term with odd powers of the spin operators such as $c(S_x^3 + S_y^3 + S_z^3)$ must remain unchanged under this operation. But for this rotation $S_x \rightarrow S_y$, $S_y \rightarrow -S_x$, and $S_z \rightarrow S_z$. Therefore

$$c(S_x^3 + S_y^3 + S_z^3) \rightarrow c(S_y^3 - S_x^3 + S_z^3) \quad .$$

This implies that the constant $c = 0$ in order for the spin Hamiltonian to remain unchanged. Hence the $\vec{S}$ dependence of the fine structure term takes the form:

$$\mathcal{H}_{S,F.S.} = \frac{1}{6} a[S_x^4 + S_y^4 + S_z^4 - \frac{1}{5} S(S+1)(3S^2 + 3S-1)] \qquad (A-24)$$

where a is the fine structure constant and the term in S is a constant added for convenience in latter calculations. The fine structure constant depends on the crystalline field and all the parameters which characterize the particular $^6S_{5/2}$ ion being described.

For convenience in latter calculations the expression for $\mathcal{H}_{S,F.S.}$ given by Eq. (A-24) can be restated in a form which depends only on S_z and $(S_x \pm iS_y)$. Let $S_{\pm} = S_x \pm iS_y$ then

$$S_{\pm}^2 = S_x^2 + S_y^2 \pm i(S_xS_y + S_yS_x) \qquad (A-25)$$

and

$$\begin{aligned} S_{\pm}^4 = {} & S_x^4 + S_y^4 - S_x^2S_y^2 - S_y^2S_x^2 \pm iS_x^2(S_xS_y + S_yS_x) \\ & \pm i\,(S_xS_y + S_yS_x)S_x^2 \mp i\,S_y^2(S_xS_y + S_yS_x) \\ & \mp i\,(S_xS_y + S_yS_x)S_y^2 - S_xS_yS_xS_y - S_yS_xS_yS_x \\ & - S_xS_y^2S_x - S_yS_x^2S_y \,. \end{aligned} \qquad (A-26)$$

However,

$$S_x^2S_y^2 + S_y^2S_x^2 = (S_x^2 + S_y^2)^2 - S_x^4 - S_y^4 \,. \qquad (A-27)$$

The commutator of S_ℓ and S_m is given by

$$[S_\ell, S_m] = i\,\epsilon_{\ell mn}\,S_n \qquad (A-28)$$

where S_k is a cartesian component of $\vec{S}$ with k = 1, 2, or 3; and $\epsilon_{\ell mn}$ is the usual permutation operator. Using Eqs. (A-26), (A-27), and (A-28) it is found that

$$S_x^4 + S_y^4 = \frac{1}{8}(S_+^4 + S_-^4) + \frac{3}{4}[S(S+1) - S_z^2]^2$$

$$+ \frac{3}{4} S_z^2 - \frac{1}{2}[S(S+1) - S_z^2] \qquad \text{(A-29)}$$

Finally, using Eq. (A-29) the expression for $\mathcal{H}_{S,F,S.}$ given by Eq. (A-24) can be written as

$$\mathcal{H}_{S,F,S.} = \frac{a}{120}[35\, S_z^4 - 30\, S(S+1)S_z^2 + 25\, S_z^2 - 6\, S(S+1)$$

$$+ 3\, S^2\,(S+1)^2] + \frac{a}{48}[S_+^4 + S_-^4] \quad . \qquad \text{(A-30)}$$

The expectation values of S_x^4, S_y^4, and S_z^4 depend on the direction of $\vec{H}$ relative to the crystalline axes. Hence, $\mathcal{H}_{S,F,S.}$ also depends on the direction of $\vec{H}$. This dependence can be calculated using Eq. (A-30). As shown in Fig. 27 let the external magnetic field $\vec{H}$ be along the z' axis of a coordinate system whose Euler angles are (θ,ϕ,χ) with respect to the (x,y,z) system. The choice of x' and y' is arbitrary and it will be seen that χ does not appear in the final result of the calculation. The components of $\vec{S}$ in the (x',y',z') system are indicated by S_x', S_y', and S_z'.

As mentioned previously the fine structure is a higher than first order effect for S state ions. For typical S state ions it is found that the magnitude of the fine structure term in the spin Hamiltonian is much less than the magnitude of the Zeeman term for $H \sim 3000$ gauss.[15] Hence, assume that the Zeeman term is the largest term in the spin Hamiltonian for $H \sim 3000$ gauss. Therefore, if g is a scalar,[15] $\vec{S}$ is quantized along the direction of $\vec{H}$. In this case, the spin Hamiltonian should be transformed from the (x,y,z) system to the coordinate system in which the Zeeman term is simply $g\beta S_z H$, i.e., the x', y', z' system. Therefore,

$$S_z = \sin\theta\sin\chi S'_x + \sin\theta\cos\chi S'_y + \cos\theta S'_z$$

$$= \frac{\sin\theta}{2i}\,(e^{i\chi}-e^{-i\chi})S'_x + \frac{\sin\theta}{2}\,(e^{i\chi}+e^{-i\chi})S'_y + \cos\theta S'_z$$

$$= -i\cos\frac{\theta}{2}\sin\frac{\theta}{2}\,e^{i\chi}\,(S'_x + iS'_y) + (\cos^2\frac{\theta}{2} - \sin^2\frac{\theta}{2})S'_z$$

$$+ i\cos\frac{\theta}{2}\sin\frac{\theta}{2}\,e^{-i\chi}\,(S'_x - iS'_y)$$

$$= -\sigma\tau^* S_+ + (\sigma\sigma^* - \tau\tau^*)S_z \qquad \text{(A-31)}$$

where

$$\sigma = \cos\frac{\theta}{2}\,e^{1/2i(\phi+\chi)} \qquad \text{(A-32)}$$

$$\tau = i\sin\frac{\theta}{2}\,e^{1/2i(-\phi+\chi)} \qquad \text{(A-33)}$$

$$S_\pm = S_x \pm iS_y \qquad \text{(A-34)}$$

Similarly,

$$S_+ = \sigma^2 S_+ + 2\sigma\tau^* S_z - \tau^{*2} S_- \qquad \text{(A-35)}$$

and

$$S_- = \sigma^{*2} S_- + 2\sigma^*\tau S_z - \tau^2 S_+ \qquad \text{(A-36)}$$

Since it has been assumed that the fine structure term is much smaller than the Zeeman term, first order perturbation theory is sufficient to determine the changes in the energy level structure due to the fine structure term. Hence,

$$E(m_s) = g\beta Hm_s + \langle S, m_s | \mathcal{H}_{S,F} | S, m_s \rangle \qquad \text{(A-37)}$$

To evaluate the matrix element in Eq. (A-37), it is first necessary to find expressions for S_z^2, S_z^4, S_+^4, and S_-^4 in terms of the components of $\vec{S}$. This can be done by using Eqs. (A-31), (A-35), and (A-36). Only the diagonal elements are necessary for this first order calculation. Bearing this in mind and using the fact that

$$S'_{\pm} \, |S', m'_s\rangle = \sqrt{(S' \mp m'_s)(S' \pm m'_s + 1)} \; |S', m'_s \pm 1\rangle \quad , \tag{A-38}$$

$$\sigma^4 \zeta^{*4} + \zeta^4 \sigma^{*4} = \frac{\sin\theta}{8} \cos 4\phi \quad , \tag{A-39}$$

$$\sigma\sigma^* - \zeta\zeta^* = \cos\theta \quad , \tag{A-40}$$

$$\sigma\sigma^*\zeta\zeta^* = \frac{\sin^2\theta}{4} \quad , \tag{A-41}$$

it can be shown that to 1st order in a, the fine structure constant,

$$E_{\pm 1/2} = \pm \frac{g\beta H}{2} + pa \quad , \tag{A-42}$$

$$E_{\pm 3/2} = \pm \frac{3g\beta H}{2} - \frac{3}{2} pa \quad , \tag{A-43}$$

$$E_{\pm 5/2} = \pm \frac{5g\beta H}{2} + \frac{1}{2} pa \quad . \tag{A-44}$$

For transitions given by $\Delta m_s = \pm 1$,

$$\Delta E(\pm 1/2 \rightarrow \mp 1/2) = g\beta H \quad , \tag{A-45}$$

$$\Delta E(\pm 3/2 \rightarrow \pm 1/2) = g\beta H \mp 5/2 \; pa \quad , \tag{A-46}$$

$$\Delta E(\pm 5/2 \rightarrow \pm 3/2) = g\beta H \pm 2 \; pa \quad , \tag{A-47}$$

where

$$p = \frac{1}{8} (35 \cos^4\theta - 30 \cos^2\theta + 3 + 5 \sin^2\theta\cos 4\phi) \quad . \tag{A-48}$$

For a rotation about a [110] axis, $\phi = 45^o$. The angular dependence of the fine structure lines for this case is shown in Fig. 28. In this figure (-2.5 pa) is plotted as a function of the angle θ. This curve gives the angular variation of the resonance line due to the transition $m_s = 3/2 \rightarrow 1/2$ (see Eq. (A-46)). The angular variations of the resonance lines due to transitions $m_s = \pm 5/2 \rightarrow \pm 3/2$ and $m_s = -3/2 \rightarrow -1/2$ are

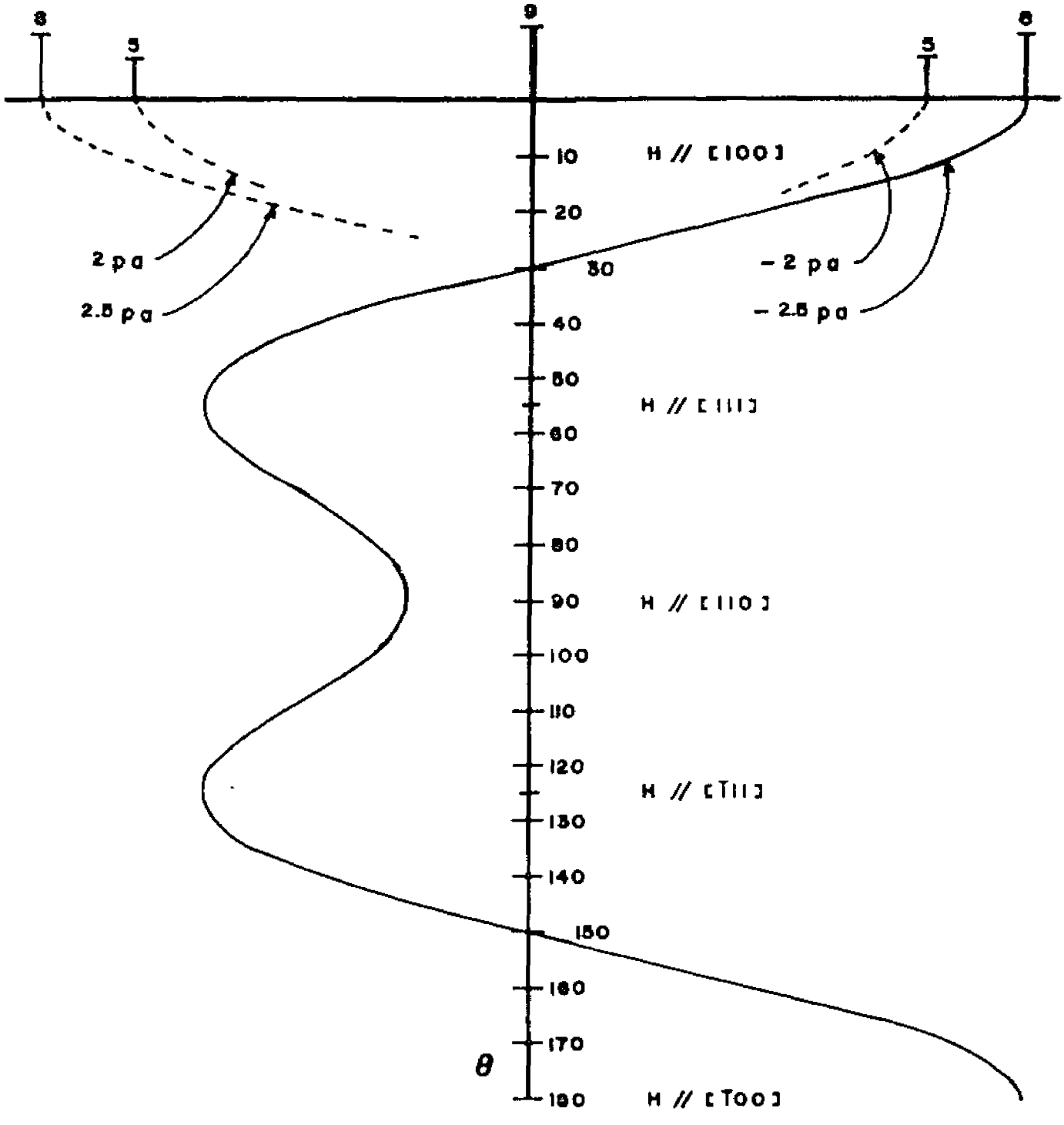

Fig. 28. Angular variation of the fine structure components of a resonance line for rotation about the [110] axis ($\phi = 45^{o}$).

similar to this variation and indicated by dashed lines in Fig. 28. The transitions due to $m_s = \pm 1/2 \rightarrow \mp 1/2$ have no angular dependence as indicated by Eq. (A-45). The lines at the top of the figure indicate the intensity ratios of the individual lines. These ratios will be discussed below. Note that the fine structure disappears when $p = 0$ and this happens when $\theta \sim 30^\circ$. Also, the maximum separation of the fine structure lines is when $\theta = 0^\circ$ ($\vec{H}$ // [100]). When $\vec{H}$ // [110], $\theta = 90^\circ$ and there is a secondary minimum in the separation of the fine structure lines.

According to the "Golden Rule" of time dependent perturbation theory,[58] the intensity of the lines given by Eqs. (A-45), (A-46), and (A-47) is proportional to the square of the matrix element perturbation operator, $\mathcal{H}'$, taken between the two states differing by $\Delta m_s = \pm 1$. However, $\mathcal{H}' = -\vec{\mu} \cdot \vec{H}'(t)$ where $\vec{\mu}$ is the magnetic dipole operator of the paramagnetic ion and $\vec{H}'(t)$ is the microwave magnetic field which is perpendicular to $\vec{H}$. Therefore, $\mathcal{H}' = -\mu_x H'_x(t)$. Also,

$$|\langle S, m_s | \mu_x | S, m_s - 1 \rangle|^2 \propto (S+m_s)(S-m_s+1) \quad , \tag{A-49}$$

where m_s is the magnetic quantum number of the upper level involved in the transition. This gives for an intensity ratio

$$I_{5/2} : I_{3/2} : I_{1/2} : I_{-1/2} : I_{-3/2} = 5 : 8 : 9 : 8 : 5 \tag{A-50}$$

where I_{m_s} is the intensity of the transition $\pm m_s \rightarrow \pm (m_s - 1)$.

For cases where the fine structure term is not too much smaller than the Zeeman term, terms of higher order in a must be considered. Details of these higher order corrections are given by Low.[32]

LIST OF REFERENCES

1. F. Seitz, Rev. Mod. Phys. 26, 7 (1954).

2. W.D. Compton and H. Rabin in Solid State Physics, eds. F. Seitz and D. Turnbull, Vol. 16 (Academic Press, New York, 1964).

3. H. Seidel and H.C. Wolf, Phys. Stat. Sol. 11, 3 (1965).

4. H. Pick, Erg. Exakt. Naturwiss. 38, 1 (1965).

5. J.H. Schulman and W.D. Compton, Color Centers in Solids (MacMillan Co., New York, 1962).

6. E.U. Condon and H. Odishaw, Eds. Handbook of Physics (McGraw-Hill, New York, 1958), p. 7-102.

7. H. Seidel, Phys. Letters 7, 27 (1963).

8. W.D. Compton and H. Rabin, loc. cit., pp. 141-4, 148-51.

9. W.D. Compton and H. Rabin, loc. cit., pp. 146-7.

10. J. Schulman and W.D. Compton, loc. cit., pp. 160-187.

11. G.E. Pake, Paramagnetic Resonance (W.A. Benjamin, Inc., New York, 1962).

12. C.P. Slichter, Principles of Magnetic Resonance (Harper & Row, New York, 1963).

13. A. Abragam, The Principles of Nuclear Magnetism (Clarendon Press, Oxford, 1961).

14. S.A. Al'tshuler and B.M. Kozyrev, Electron Paramagnetic Resonance (Academic Press, New York, 1964).

15. W. Low, Paramagnetic Resonance in Solids (Academic Press, New York, 1960).

16. D.C. Krupka and R.H. Silsbee, Phys. Rev. Letters 12, 193 (1964).

17. H. Seidel, et. al., Z. Phys. 182, 398 (1965).

18. W. Low, loc. cit., p. 39.

19. Bausch and Lomb Reference Manual #33-28-02 (Bausch and Lomb, Inc., Rochester, New York).

20. Varian Associates Publication #87-100-074 (Varian Associates, Palo Alto, California).

21. Varian Associates Staff, NMR and EPR Spectroscopy, (Pergamon Press, New York, 1960), pp. 66-68.

22. R.A. Andrews and Y.W. Kim, Rev. Sci. Instr. 37, 411 (1966).

23. R. Ager, T. Cole, and J. Lambe, Rev. Sci. Instr. 34, 308 (1963).

24. E.L. Ginzton, Microwave Measurements (McGraw-Hill Book Co., Inc., New York, 1957), Appendix A, p. 480.

25. B. Bleaney and W. Hayes, Proc. Phys. Soc. 70B, 626 (1957).

26. W. Hayes and D.A. Jones, Proc. Phys. Sco. 71, 503 (1958).

27. M. Satoh and C.P. Slichter, Phys. Rev. 144, 259 (1966): These authors summarize studies of Fe^{3+} in AgCl. All Fe^{3+} studies before 1958 are reported in Ref. 14, pp. 319 and 140.

28. S.A. Al'tshuler and B.M. Kozyrev, loc. cit., pp. 139-140.

29. W. Hayes, J. Appl. Phys., Supp. to Vol. 33, p. 329 (1962).

30. D.H. McMahon, Phys. Rev. 134, A128 (1964).

31. W.C. Holton and H. Blum, Phys. Rev. 125, 89 (1962): The F center resonance in NaF is an isotropic line at g = 2.001 with a partially resolved structure. 19 lines with 37.7 g separation.

32. W. Low, loc. cit., pp. 114-117.

33. L.H. Ahrens, Geochim. et. Cosmochim. Acta 2, 155 (1952).

34. N.S. Gill and R.S. Hyholm, J. Chem. Soc. 3997 (1959).

35. W. Low, loc. cit., p. 159.

36. W. Low, loc. cit., p. 118.

37. S.A. Al'tshuler and B.M. Kozyrev, loc. cit., p. 72.

38. H. Watanabe, Progr. Theoret. Phys. (Kyoto) 18, 405 (1957). Terms which are third order in K are considered by Watanabe, but according to his theory the coefficients of these terms make their contribution almost negligible. This is not what is observed in the present work.

39. F. Luty, Z. Phys. 165, 17 (1961).

40. E. Link and F. Lüty, Abstract #120, Int. Symp. Color Centers in Alkali Halides, Univ. of Ill., Urbana, Ill. (1965).

41. C.J. Delbecq, Z. Phys. 171, 560 (1963).

42. Y. Farge, M. Lambert, and R. Smoluchowski, Solid State Comm. 4, 333 (1966).

43. N.P. Kalabukhov and P.K. Gorbenko, Optika i Spektrosk. 16, 475 (1964); [English translation in: Optics and Spectrosc. 16, 258 (1964)].

44. M.J. Kirai, Phys. Soc. Japan 14, 1400 (1959).

45. W.E. Bron and A.S. Nowick, Phys. Rev. 119, 114 (1960).

46. H.W. Etzel, Phys. Rev. 87, 906 (1952).

47. G.J. Dienes, J. Chem. Phys. 16, 620 (1948).

48. R.A. Andrews and Y.W. Kim, Phys. Letters 21, 616 (1966).

49. S. Hattori, J. Phys. Soc. Japan 17, 1454 (1962).

50. K. Kubo, J. Phys. Soc. Japan 16, 2294 (1961).

51. S. Hattori, J. Phys. Soc. Japan 15, 2117 (1960).

52. H.F. Ivey, Phys. Rev. 72, 341 (1947).

53. R. Herman, M.C. Wallis, and R.F. Wallis, Phys. Rev. 103, 87 (1956).

54. C.B. Pierce, Phys. Rev. 135, A83 (1964).

55. W. Low, loc. cit., p. 58.

56. G.E. Pake, loc. cit., p. 11.

57. B. Bleaney and K.W.H. Stevens, Repts. Progr. in Phys. 16, 108 (1953).

58. E. Merzbacher, Quantum Mechanics (J. Wiley & Sons, Inc., New York, 1961), p. 470.

AUTOBIOGRAPHICAL STATEMENT

NAME.	Ronald Allen Andrews
BIRTH:	March 1, 1940; Pontiac, Michigan
EDUCATION:	High School Diploma, St. Michael High School, Pontiac, Michigan, 1958; Bachelor of Science in Physics, Wayne State University, 1962.
RECOGNITIONS	Phi Beta Kappa, 1962 Bachelor of Science in Physics with High Distinction, 1962 The Society of the Sigma Xi, 1965 National Science Foundation Cooperative Graduate Fellowship (1962-1966)
PROFESSIONAL MEMBERSHIPS.	American Physical Society American Association of Physics Teachers American Association for the Advancement of Science Phi Beta Kappa The Society of the Sigma Xi
PUBLICATIONS	"Cryostat for Combined EPR and Optical Studies," R.A Andrews and Y.W. Kim, Rev. Sci. Instr. 37, 411 (1966). "Observation of an Unstable N Band in NaF," R.A. Andrews and Y.W. Kim, Phys Letters 21, 616 (1966). "Electron Paramagnetic Resonance of Fe^{3+} in NaF," R.A Andrews and Y.W Kim submitted to the Physical Review (1966). "Iron Impurity Controlled Conversion in x irradiated NaF," R.A Andrews and Y.W. Kim, submitted to the Physical Review (1966).